Robert Köberl, BSc

Alternative Description of the Magnetic Field Topology for a 3D-MHD Equilibrium Code

MASTER'S THESIS

to achieve the university degree of

Diplom-Ingenieur

Master's degree programme: Technical Physics

submitted to

Graz University of Technology

Supervisor

Ass.Prof. Dipl.-Ing. Dr.techn. Winfried Kernbichler

Institute of Theoretical Physics - Computational Physics

Co-Supervisor

Dipl.-Ing. Dr.rer.nat. BSc Christopher Albert

Institute of Theoretical Physics - Computational Physics

Graz, May 18, 2021

AFFIDAVIT

I declare that I have authored this thesis independently, that I have not used other than the declared sources/resources, and that I have explicitly indicated all material which has been quoted either literally or by content from the sources used. The text document uploaded to TUGRAZonline is identical to the present master's thesis.

Date, Signature

ACKNOWLEDGEMENT

I would like to thank my advisor Dr. Ing. Florian Hindenlang for his extensive, persistent and immensely helpful support throughout this thesis. Additionally, I would like to thank the entire plasma-physics research group at the Graz University of Technology for their constructive discussions and useful inputs.

Contents

Abstract

The computation of ideal magnetohydrodynamic (MHD) equilibria plays an important role in fusion research, since it allows to approximately describe the steady state of magnetically confined plasmas. Ideal MHD describes a macroscopic single-fluid magnetically confined plasma under the assumption of high collisionality, small ion gyro-radius and small resistivity. The MHD equilibrium is then obtained in the static case by solving the corresponding force balance equation $\nabla P = \mathbf{J} \times \mathbf{B}$. Where P is the pressure, $\mathbf{J}$ the current density and $\mathbf{B}$ the magnetic field. The Galerkin Variational Equilibrium Code (GVEC) calculates three-dimensional MHD equilibrium configurations. In this work, alternative representations of the magnetic field topology are introduced and examined. GVEC uses a gradient descent algorithm to minimize the total energy functional for nested magnetic flux surfaces. This yields the desired force balance. Under the assumption of closed nested flux surfaces, the magnetic field can be written in flux coordinates that consist of the poloidal and toroidal angles θ and ζ as well as the flux surface label s. The magnetic flux surfaces are then expressed via a mapping from the flux coordinates onto the real space coordinates (X^1, X^2, ζ). For this mapping two alternative formulations are implemented and analysed. The first is based on the NSTAB code [2] which introduces a blending of the outermost flux surface to the magnetic axis via the introduction of a generalised radius. As shown in the numerical results, this NSTAB mapping exhibited convergence problems even for simple geometries in the near axis region and, therefore, motivated the introduction of a new hybrid mapping, a hybridisation between the original GVEC mapping and the NSTAB mapping. As a result the near axis problematic of the NSTAB mapping was resolved. It was shown, that for the hybrid mapping the boundary conditions have to be chosen carefully when solving equilibria with a complex boundary shape. Additionally, the influence of the radial and spectral resolution was investigated for the original GVEC mapping and the hybrid mapping using a test case with a simple elliptic boundary shape. Through this, the convergence of the total energy with increasing resolution was demonstrated. In comparison to the original GVEC mapping, the hybrid mapping proved more sensible with regards to the resolution especially regarding the placement of the magnetic axis.

1. Introduction

In hope of finding a reliable alternative source of energy, thermonuclear fusion devices have been of great interest since the last century. Due to the extreme physical conditions needed for the fusion reaction of deuterium and tritium, special devices were developed to contain the necessary high temperature plasmas within a controlled environment. One approach is magnetic confinement. From the various geometries tested two toroidal confinement concepts seem to provide the most promising results: The stellarator and the tokamak. Such fusion devices are of extremely high complexity and designing and building devices like the ITER tokamak or the W7-X stellarator needs not only technical and mechanical ingenuity but also computational and theoretical analysis.

Many computer codes dealing with various aspects of fusion plasmas and fusion devices exist nowadays. One field of those codes deals with the solution of the so-called magneto-hydrodynamic equations (MHD). Although, this theory works with several assumptions and simplifications, MHD equilibrium and stability are necessary requirements for designing fusion reactors. [1]

This work, which was done in close cooperation with the Max-Planck Institute for Plasma Physics via the support of Dr. Ing. Florian Hindenlang, evolves around the Galerkin Variational Equilibrium Code (GVEC). GVEC is a new 3D MHD equilibrium code developed by F.Hindenlang and O.Maj which is based on the ideas of the established VMEC [10]. By minimizing the total energy functional, arising from the ideal MHD theory, under the assumption of nested flux surfaces, equilibrium configurations of the magnetic field for magnetic confinement fusion devices can be calculated. The minimisation itself is performed via gradient descent. The underlying theory is heavily dependent on the description of the magnetic field in a flux coordinate system, which form the natural coordinate system for toroidal fusion devices. These coordinates are the poloidal and toroidal angles θ and ζ as well as a radial coordinate labelling the magnetic flux surfaces s. In GVEC, magnetic flux surfaces are then expressed via a mapping from the flux coordinates onto real space coordinates generally denoted via (X^1, X^2, ζ). Usually, these real space coordinates equal the cylindrical coordinates (R, Z, ϕ).

This mapping from flux- to real space coordinates is the main topic of this work. In the paper by M.Taylor [2] about the NSTAB 3D MHD equilibrium code, an alternative mapping to the one of GVEC is proposed. This NSTAB mapping utilizes a blending of the outermost flux surface to the magnetic axis, where M.Taylor [2] introduces a special approximate treatment of the near axis region via an axis residue condition. Promising results due to this mapping concerning perturbation calculations via NSTAB motivated this work. The goal is to implement and analyse the alternative mapping within GVEC.

In the first part of the thesis, an introduction and derivation of the physical and

[1] see Freidberg 2014, 1 [7]

mathematical theory concerning ideal MHD is given. Starting from a two fluid model, the ideal MHD equations are derived and their validity regime is discussed. Additionally, core concepts like the corresponding energy functional and flux surfaces are introduced. Furthermore, a detailed explanation of flux coordinate systems and important concepts of the differential geometry algebra are presented.

The second part focuses on the description of the computer code itself. Further, the newly implemented alternative mapping to describe the magnetic field topology used in NSTAB [2] as well as a newly introduced hybrid mapping, a hybridisation between the original GVEC mapping and the NSTAB mapping, are described. Moreover, the resulting changes in GVEC are explained and discussed.

The third part then presents the numerical results obtained with the different mappings. Via three test geometries of increasing complexity, comparisons between results obtained with the original GVEC mapping and the two alternatives are performed. In addition, the influence of different boundary conditions for the newly introduced quantities are examined. Finally, dependencies on the radial and spectral resolutions are investigated by examination of the total energy and the position of the magnetic axis.

2. Theory

This chapter introduces the fundamental concepts and theories necessary for the formulation and understanding of the physical and mathematical framework.

The first section presents a derivation of the ideal magneto hydrodynamic (MHD) equations, following closely the structure shown in the books by Bellan [5] and Freidberg [7] but including detailed mathematical steps to allow for a consistent formulation of these fundamental results within the thesis. Additionally, important consequences of the formalism of ideal MHD are shown and a short summary of the discussion on the validity of this theory, as written by Freidberg [7], is given.

The second section provides the necessary foundation for understanding the flux coordinates needed in MHD equilibrium codes such as VMEC and GVEC, following the detailed and extensive book by W.D.D'haeseleer et al. [4].

2.1. Ideal Magneto-Hydrodynamic Equations

The ideal magneto-hydrodynamic (MHD) equations and their relevance and validity for fusion plasmas form the very basis of this thesis and minimisation codes like GVEC. Therefore, a derivation and a discussion of the validity of those fundamental relations shall be presented.

2.1.1. The Vlasov-Equation

To obtain a closed set of equations, describing a fusion plasma in the framework of fluid mechanics one can derive the so-called ideal magneto hydrodynamic equations. A common starting point for this derivation is by assuming a distribution function for a plasma consisting of charged particles and the corresponding differential equation as given by the so-called Vlasov equation

$$\frac{\partial f_\sigma}{\partial t} + \nabla_x \cdot (\mathbf{v} f_\sigma) + \nabla_v \cdot \left(\frac{q_\sigma}{m_\sigma} (\mathbf{E} + \mathbf{v} \times \mathbf{B}) f_\sigma \right) = \sum_\alpha C_{\sigma\alpha} (f_\sigma) , \tag{2.1.1}$$

where σ is the index denoting the particle species, f represents the distribution function, ∇_x the Nabla operator for the spacial variable $\mathbf{x}$, ∇_v the Nabla operator for the velocity variable $\mathbf{v}$, $\mathbf{E}$ and $\mathbf{B}$ the electric and magnetic field and $C_{\sigma,\alpha}$ is the rate of change of f_σ due to collisions of particle species σ with particle species α. Hereby, the collision operator $C_{\sigma\alpha} (f_\sigma)$ must obey the following constraints [2]:

- The total number of particles must be conserved:

$$\int C_{\sigma\alpha} (f_\sigma) \, d\mathbf{v} = 0. \tag{2.1.2}$$

- The total momentum must be conserved for collisions between like particles and for all particle collisions together [3]:

[2] see Bellan 2008, 35 [5]

[3] Here, m_σ denotes the mass of the corresponding species and the indices e and i stand for electrons and ions.

$$\int m_\sigma \mathbf{v} C_{\sigma\sigma}(f_\sigma)\, d\mathbf{v} = 0. \tag{2.1.3}$$

$$\int m_e \mathbf{v} C_{ei}(f_e)\, d\mathbf{v} + \int m_i \mathbf{v} C_{ie}(f_i)\, d\mathbf{v} = 0. \tag{2.1.4}$$

- The total energy must be conserved for collisions between like particles and for all particle collisions together:

$$\int m_\sigma v^2 C_{\sigma\sigma}(f_\sigma)\, d\mathbf{v} = 0. \tag{2.1.5}$$

$$\int m_e v^2 C_{ei}(f_e)\, d\mathbf{v} + \int m_i v^2 C_{ie}(f_i)\, d\mathbf{v} = 0. \tag{2.1.6}$$

With this setup it is now possible to take moments of the whole equation, i.e. perform integrals over the whole velocity phase space with different weights of $\mathbf{v}(\int d\mathbf{v}\cdots, \int d\mathbf{v}\mathbf{v}\cdots, \int d\mathbf{v} v^2\cdots)$. For this purpose it is advisable to recall the general definition for the number density $n_\sigma(\mathbf{x})$ and the mean velocity $\mathbf{u}_\sigma(\mathbf{x})$ of a distribution function $f_\sigma(\mathbf{x}, \mathbf{v})$:

$$n_\sigma(\mathbf{x}) = \int f_\sigma(\mathbf{x}, \mathbf{v}) d\mathbf{v}. \tag{2.1.7}$$

$$\mathbf{u}_\sigma(\mathbf{x}) = \frac{\int \mathbf{v} f_\sigma(\mathbf{x}, \mathbf{v}) d\mathbf{v}}{n_\sigma(\mathbf{x})}. \tag{2.1.8}$$

2.1.2. The Species Continuity Equation

If one now takes the first moment of (2.1.1) we have to deal with three different terms on the left-hand side and the collsion term on the right:

$$\int \left[\underbrace{\frac{\partial f_\sigma}{\partial t}}_{\text{I}} + \underbrace{\nabla_x \cdot (\mathbf{v} f_\sigma)}_{\text{II}} + \underbrace{\nabla_v \cdot \left(\frac{q_\sigma}{m_\sigma} (\mathbf{E} + \mathbf{v} \times \mathbf{B}) f_\sigma \right)}_{\text{III}} \right] d\mathbf{v} = \underbrace{\int \sum_\alpha C_{\sigma\alpha}(f_\sigma)\, d\mathbf{v}}_{C}. \tag{2.1.9}$$

The time derivative for I can be pulled out of the integral and thus using (2.1.7) one can write

$$\text{I}: \int \frac{\partial}{\partial t} f_\sigma d\mathbf{v} = \frac{\partial}{\partial t} \int f_\sigma d\mathbf{v} = \frac{\partial n_\sigma}{\partial t}. \tag{2.1.10}$$

In a similar fashion, the spatial derivative in II does not affect the integration so that by recalling (2.1.8) one can write

$$\text{II}: \int \nabla_x \cdot (\mathbf{v} f_\sigma)\, d\mathbf{v} = \nabla_x \cdot \int \mathbf{v} f_\sigma d\mathbf{v} = \nabla_x \cdot (n_\sigma \mathbf{u}_\sigma). \tag{2.1.11}$$

For the third term, the Nabla operator can not be extracted from the integral. However, by collecting the terms for the Lorentz-force into one variable $\mathbf{F}_L := \frac{q_\sigma}{m_\sigma}(\mathbf{E} + \mathbf{v} \times \mathbf{B})$ and applying the divergence theorem ($\int_V \nabla \cdot \mathbf{F} dV = \oint_S \mathbf{F} \cdot \mathbf{n} dS$) one can easily see, that this part of the equation must vanish, since the probability of finding particles at infinite velocities is zero. This is because the evaluation is done over the whole phase space of $\mathbf{v}$ and thus, the surface has to be evaluated at $v = \infty$:

$$\text{III}: \int \nabla_v \cdot (\mathbf{F}_L f_\sigma)\, d\mathbf{v} = \oint \mathbf{F}_L f_\sigma \cdot d\mathbf{S}_v = 0. \tag{2.1.12}$$

For the collision term C, the summation is swapped with the integral and therefore (2.1.2) can be used to see that

$$C: \int \sum_{\alpha} C_{\sigma\alpha} f_\sigma d\mathbf{v} = \sum_{\alpha} \int C_{\sigma\alpha} f_\sigma d\mathbf{v} \overset{(2.1.2)}{=} 0. \tag{2.1.13}$$

Hence, combining I, II, III and C one arrives at the species continuity equation:

$$\frac{\partial n_\sigma}{\partial t} + \nabla_x \cdot (n_\sigma \mathbf{u}_\sigma) = 0. \tag{2.1.14}$$

2.1.3. The First Moment Equation

In a similar approach to Sec.2.1.2 one can perform calculations by taking the first moment of the Vlasov-equation, i.e. multiplying by $\mathbf{v}$ an integrating over the whole velocity phase space. Again, the three different terms plus the collision on the right-hand side have to be treated:

$$\begin{aligned} \int \mathbf{v} \Bigg[\underbrace{\frac{\partial f_\sigma}{\partial t}}_{\mathrm{I}} + \underbrace{\nabla_x \cdot (\mathbf{v} f_\sigma)}_{\mathrm{II}} + \underbrace{\nabla_v \cdot \left(\frac{q_\sigma}{m_\sigma} (\mathbf{E} + \mathbf{v} \times \mathbf{B}) f_\sigma \right)}_{\mathrm{III}} \Bigg] d\mathbf{v} \\ = \int \underbrace{\mathbf{v} \sum_{\alpha} C_{\sigma\alpha}(f_\sigma)}_{C} d\mathbf{v}. \end{aligned} \tag{2.1.15}$$

For the first term I, one can extract the time derivative since $\mathbf{v}$ and t are independent variables. Taking (2.1.8) into account one is left with

$$\mathrm{I}: \int \mathbf{v} \frac{\partial}{\partial t} f_\sigma d\mathbf{v} = \frac{\partial}{\partial t} \int \mathbf{v} f_\sigma d\mathbf{v} \overset{(2.1.7)}{=} \frac{\partial (n_\sigma \mathbf{u}_\sigma)}{\partial t}. \tag{2.1.16}$$

Before considering the second term II it is useful to deal with one essential change of variables:

$$\mathbf{w} = \mathbf{v} - \mathbf{u}_\sigma. \tag{2.1.17}$$

This variable $\mathbf{w}$ is advantageous for,

$$d\mathbf{w} = d\mathbf{v} \tag{2.1.18}$$

and

$$\int \mathbf{w} f_\sigma d\mathbf{w} = \int \mathbf{v} f_\sigma d\mathbf{v} - \int \mathbf{u}_\sigma f_\sigma d\mathbf{v} \overset{(2.1.7),(2.1.8)}{=} n_\sigma \mathbf{u}_\sigma - n_\sigma \mathbf{u}_\sigma = 0. \tag{2.1.19}$$

If one now extracts the spatial Nabla operator, which does not affect the variable $\mathbf{v}$, for the second term and performs the change of variables shown above, II can be rewritten in the following way:

$$\begin{aligned} \mathrm{II}: \int \mathbf{v} \nabla_x \cdot (\mathbf{v} f_\sigma) \, d\mathbf{v} &= \nabla_x \cdot \int (\mathbf{w} + \mathbf{u}_\sigma)(\mathbf{w} + \mathbf{u}_\sigma) f_\sigma d\mathbf{w} \\ &= \nabla_x \cdot \int (\mathbf{w}\mathbf{w} + \mathbf{w}\mathbf{u}_\sigma + \mathbf{w}\mathbf{u}_\sigma + \mathbf{u}_\sigma \mathbf{u}_\sigma) f_\sigma d\mathbf{w} \\ &= \nabla_x \cdot \int \mathbf{w}\mathbf{w} f_\sigma d\mathbf{w} + \nabla_x \cdot (n_\sigma \mathbf{u}_\sigma \mathbf{u}_\sigma). \end{aligned} \tag{2.1.20}$$

In the last step, the two mixed terms were dropped because $\mathbf{u}_\sigma$ is independent of $\mathbf{w}$ and thus the integral vanishes due to (2.1.19).

For the third term, one can accomplish some simplification by making use of the vector identity

$$\nabla \cdot (\mathbf{ab}) = \mathbf{a} \cdot \nabla \mathbf{b} + \nabla \mathbf{a} \cdot \mathbf{b}. \tag{2.1.21}$$

Additionally, the divergence theorem may be applied once again leading to

$$\begin{aligned} \mathrm{III}: \int \mathbf{v} \nabla_v \cdot (\mathbf{F}_L f_\sigma)\, d\mathbf{v} \\ &= \int \left[\nabla_v \cdot (\mathbf{v}\mathbf{F}_L f_\sigma) - \underbrace{(\nabla_v \mathbf{v})}_{=1} \cdot (\mathbf{F}_L f_\sigma) \right] d\mathbf{v} \\ &= \underbrace{\oint \mathbf{v}\mathbf{F}_\mathbf{L} f_\sigma d\mathbf{S}_v}_{=0} - \frac{q_\sigma}{m_\sigma} \left[\int \mathbf{E} f_\sigma d\mathbf{v} + \int (\mathbf{v} \times \mathbf{B})\, f_\sigma d\mathbf{v} \right] \\ &= -\frac{q_\sigma}{m_\sigma} n_\sigma \left[\mathbf{E} + \mathbf{u}_\sigma \times \mathbf{B} \right]. \end{aligned} \tag{2.1.22}$$

In the last step, the integration was performed using the fact, that neither $\mathbf{E}$ nor $\mathbf{B}$ are velocity dependent. For the collision term, the integral does not vanish this time. The contributions are gathered in the expression $\mathbf{R}_{\sigma\alpha}$, denoting the frictional drag force between the two species σ and α due to collisions:

$$C: \int_C \mathbf{v} \sum_\alpha C_{\sigma\alpha}(f_\sigma) d\mathbf{v} =: \frac{1}{m_\sigma} \mathbf{R}_{\sigma\alpha}. \tag{2.1.23}$$

Thus, combining the four contributions and slightly rearranging the terms one obtains an equation of the form

$$m_\sigma \left[\frac{\partial (n_\sigma \mathbf{u}_\sigma)}{\partial t} + \nabla_x \cdot (n_\sigma \mathbf{u}_\sigma \mathbf{u}_\sigma) \right] = n_\sigma q_\sigma (\mathbf{E} + \mathbf{u}_\sigma \times \mathbf{B}) - \nabla_x \cdot \overleftrightarrow{\mathbf{P}}_\sigma - \mathbf{R}_{\sigma\alpha}. \tag{2.1.24}$$

Here, the definition for the *pressure tensor* $\overleftrightarrow{\mathbf{P}}_\sigma$ was used:

$$\overleftrightarrow{\mathbf{P}}_\sigma := m_\sigma \int \mathbf{w}\mathbf{w} f_\sigma d\mathbf{w} = m_\sigma \int (\mathbf{v} - \mathbf{u}_\sigma)(\mathbf{v} - \mathbf{u}_\sigma) f_\sigma d\mathbf{v}. \tag{2.1.25}$$

Where the isotropic contribution is given by

$$\begin{aligned} P_\sigma &:= \int w_x w_x f_\sigma d\mathbf{w} = \int w_y w_y f_\sigma d\mathbf{w} = \int w_z w_z f_\sigma d\mathbf{w} \\ &= \frac{m_\sigma}{3} \int \mathbf{w} \cdot \mathbf{w} f_\sigma d\mathbf{w} \end{aligned} \tag{2.1.26}$$

and the anisotropic contribution can be expressed via

$$\mathbf{\Pi}_\sigma = \overleftrightarrow{\mathbf{P}}_\sigma - P_\sigma \overleftrightarrow{\mathbf{I}}. \tag{2.1.27}$$

However, for now an isotropic form of the pressure tensor will be assumed. Further simplification can be achieved by expanding the derivatives on the left-hand side and recalling the species continuity equation (2.1.14):

$$\begin{aligned}\frac{\partial\left(n_\sigma \mathbf{u}_\sigma\right)}{\partial t}+\nabla_x\cdot\left(n_\sigma \mathbf{u}_\sigma \mathbf{u}_\sigma\right) &= n_\sigma\frac{\partial \mathbf{u}_\sigma}{\partial t}+\mathbf{u}_\sigma\frac{\partial n_\sigma}{\partial t}+\mathbf{u}_\sigma\left[\nabla_x\cdot\left(n_\sigma \mathbf{u}_\sigma\right)\right]+\left(n_\sigma \mathbf{u}_\sigma\right)\left(\nabla_x\cdot\mathbf{u}_\sigma\right)\\ &= n_\sigma\frac{\partial \mathbf{u}_\sigma}{\partial t}+\mathbf{u}_\sigma\underbrace{\left[\frac{\partial n_\sigma}{\partial t}+\nabla_x\cdot\left(n_\sigma \mathbf{u}_\sigma\right)\right]}_{\overset{(2.1.14)}{=}0}+\left(n_\sigma \mathbf{u}_\sigma\right)\left(\nabla_x\cdot\mathbf{u}_\sigma\right)\\ &= n_\sigma\frac{d\mathbf{u}_\sigma}{dt}.\end{aligned} \tag{2.1.28}$$

In the last step the definition of the *convective derivative* is introduced:

$$\frac{d}{dt}=\frac{\partial}{\partial t}+\mathbf{u}_\sigma\cdot\nabla_x. \tag{2.1.29}$$

Thence, the moment equation can be cast into a compact form reading

$$m_\sigma n_\sigma\frac{d\mathbf{u}_\sigma}{dt}=n_\sigma q_\sigma\left(\mathbf{E}+\mathbf{u}_\sigma\times\mathbf{B}\right)-\nabla_x\cdot\overleftrightarrow{\mathbf{P}}_\sigma-\mathbf{R}_{\sigma\alpha}. \tag{2.1.30}$$

2.1.4. The Second Moment Equation

Although it already becomes obvious that proceeding with taking higher moments will not yield a closed set of equations due to the $\mathbf{v}\cdot\nabla_x f$ term in the Vlasov equation, it is still advisable to perform some further calculations by taking the second moment. If the weight is chosen as $\frac{m_\sigma v^2}{2}$ one ends up with an expression for the energy:

$$\begin{aligned}\int\frac{m_\sigma v^2}{2}\Bigg[\underbrace{\frac{\partial f_\sigma}{\partial t}}_{\mathrm{I}}+\underbrace{\nabla_x\cdot\left(\mathbf{v}f_\sigma\right)}_{\mathrm{II}}+\underbrace{\nabla_v\cdot\left(\frac{q_\sigma}{m_\sigma}\left(\mathbf{E}+\mathbf{v}\times\mathbf{B}\right)f_\sigma\right)}_{\mathrm{III}}\Bigg]d\mathbf{v}\\ =\underbrace{\int\frac{m_\sigma v^2}{2}\sum_\alpha C_{\sigma\alpha}\left(f_\sigma\right)d\mathbf{v}}_{C}.\end{aligned} \tag{2.1.31}$$

Executing the same term separated procedure as before one can evaluate the first one I via the change of variables given by (2.1.17)-(2.1.19):

$$\begin{aligned}\mathrm{I}:\frac{\partial}{\partial t}\int\frac{m_\sigma v^2}{2}f_\sigma d\mathbf{v} &= \frac{\partial}{\partial t}\int\frac{m_\sigma\left(\mathbf{w}+\mathbf{u}_\sigma\right)^2}{2}f_\sigma d\mathbf{v}\\ &= \frac{\partial}{\partial t}\int\frac{1}{2}m_\sigma\left(\mathbf{w}\cdot\mathbf{w}+\underbrace{2\mathbf{w}\cdot\mathbf{u}_\sigma}_{\overset{(2.1.19)}{=}0}+\mathbf{u}_\sigma\cdot\mathbf{u}_\sigma\right)f_\sigma d\mathbf{v}\\ &= \frac{\partial}{\partial t}\left(\frac{3P_\sigma}{2}+\frac{m_\sigma n_\sigma u_\sigma^2}{2}\right).\end{aligned} \tag{2.1.32}$$

For the second term II using the same substitution, new physical quantities can be defined:

$$\begin{aligned}
\text{II} :& \nabla_x \cdot \int \frac{m_\sigma v^2}{2} \mathbf{v} f_\sigma d\mathbf{v} \\
&= \nabla_x \cdot \int \frac{m_\sigma}{2} \left(w^2 \mathbf{w} + 2 \left(\mathbf{u}_\sigma \cdot \mathbf{w} \right) \mathbf{w} + \underbrace{u_\sigma^2 \mathbf{w}}_{=0} + w^2 \mathbf{u}_\sigma + \underbrace{2 \left(\mathbf{u}_\sigma \cdot \mathbf{w} \right) \mathbf{u}_\sigma}_{=0} + u_\sigma^2 \mathbf{u}_\sigma \right) f_\sigma d\mathbf{w} \\
&= \nabla_x \cdot \left(\mathbf{Q}_\sigma + \frac{5}{2} P_\sigma \mathbf{u}_\sigma + \frac{m_\sigma n_\sigma u_\sigma^2}{2} \mathbf{u}_\sigma \right).
\end{aligned} \tag{2.1.33}$$

The terms with just a single $\mathbf{w}$ in the integration vanish as per definition, and the new introduced quantity $\mathbf{Q}_\sigma$ is called the *heat flux* with the definition

$$\mathbf{Q}_\sigma := \int \frac{m_\sigma w^2}{2} \mathbf{w} f_\sigma d\mathbf{w}. \tag{2.1.34}$$

For the acceleration term III an application of Stoke's theorem for the $\mathbf{E}$-field and the $(\mathbf{v} \times \mathbf{B})$ term is necessary. To get III into a form where the theorem can be applied one needs to consider the following:

$$\left\{ \nabla_v \cdot (\mathbf{v} \times \mathbf{B}) \right\}_i = \epsilon_{ijk} \partial_i v_j B_k = \epsilon_{ijk} \delta_{ij} B_k = 0.$$

$$\nabla_v \cdot \left[\frac{v^2}{2} (\mathbf{v} \times \mathbf{B}) f_\sigma \right] = \underbrace{\mathbf{v} \cdot (\mathbf{v} \times \mathbf{B}) f_\sigma}_{=0} + \underbrace{\frac{v^2}{2} f_\sigma \nabla_v \cdot (\mathbf{v} \times \mathbf{B})}_{=0} + \frac{v^2}{2} (\mathbf{v} \times \mathbf{B}) \nabla_v f_\sigma.$$

$$\nabla_v \cdot \frac{v^2}{2} \mathbf{E} = \frac{v^2}{2} \nabla_v \cdot \mathbf{E} + \mathbf{v} \cdot \mathbf{E}.$$

Using these relations one can therefore evaluate III as

$$\begin{aligned}
\text{III} :\ & q_\sigma \int \frac{v^2}{2} \nabla_v \cdot \left[(\mathbf{E} + \mathbf{v} \times \mathbf{B}) f_\sigma \right] d\mathbf{v} \\
&= q_\sigma \int \frac{v^2}{2} \nabla_v \cdot \mathbf{E} f_\sigma d\mathbf{v} + q_\sigma \int \nabla_v \cdot \left[\frac{v^2}{2} (\mathbf{v} \times \mathbf{B}) f_\sigma \right] d\mathbf{v} \\
&= q_\sigma \int \nabla_v \cdot \frac{v^2}{2} \mathbf{E} f_\sigma d\mathbf{v} - q_\sigma \int \mathbf{v} \cdot \mathbf{E} f_\sigma d\mathbf{v} + \underbrace{\oint \frac{v^2}{2} (\mathbf{v} \times \mathbf{B}) f_\sigma \cdot d\mathbf{S}_v}_{=0} \\
&= q_\sigma \underbrace{\oint \frac{v^2}{2} \mathbf{E} f_\sigma \cdot d\mathbf{S}_v}_{=0} - q_\sigma \int \mathbf{v} \cdot \mathbf{E} f_\sigma d\mathbf{v} \\
&= -q_\sigma n_\sigma \mathbf{u}_\sigma \cdot \mathbf{E}.
\end{aligned} \tag{2.1.35}$$

It is worth noting, that the surface integrations again vanish due to the evaluation of the distribution function at infinite velocities.

Recalling (2.1.5) allows one to recast and identify the collision contribution

$$\sum_\alpha \int m_\sigma \frac{v^2}{2} C_{\sigma\alpha} f_\sigma d\mathbf{v} = \int_{\alpha \neq \sigma} m_\sigma \frac{v^2}{2} C_{\sigma\alpha} f_\sigma d\mathbf{v} = - \left(\frac{\partial W}{\partial t} \right)_{E\alpha\sigma} \tag{2.1.36}$$

as the energy transfer rate between the two different species α and σ. Recombining everything from above with small rearrangements gives one

$$\begin{aligned}\left(\frac{\partial}{\partial t}\frac{m_\sigma n_\sigma u_\sigma^2}{2} + \nabla_x \cdot \frac{m_\sigma n_\sigma u_\sigma^2}{2}\mathbf{u}_\sigma\right) + \frac{\partial}{\partial t}\frac{3P_\sigma}{2} + \nabla_x \cdot \left(\mathbf{Q}_\sigma + \frac{5}{2}P_\sigma \mathbf{u}_\sigma\right) \\ = q_\sigma n_\sigma \mathbf{E}\cdot\mathbf{u}_\sigma - \left(\frac{\partial W}{\partial t}\right)_{E\alpha\sigma}.\end{aligned} \tag{2.1.37}$$

To achieve further simplification it is necessary to make use of some identities. The first one is obtained by simply expanding derivatives,

$$\begin{aligned}&\frac{\partial}{\partial t}\frac{m_\sigma n_\sigma u_\sigma^2}{2} + \nabla_x \cdot \frac{m_\sigma n_\sigma u_\sigma^2}{2}\mathbf{u}_\sigma \\ &= \frac{m_\sigma}{2}\left[n_\sigma \frac{\partial u_\sigma^2}{\partial t} + \underbrace{u_\sigma^2 \frac{\partial n_\sigma}{\partial t} + u_\sigma^2 \nabla_x \cdot (n_\sigma \mathbf{u}_\sigma)}_{\overset{(2.1.14)}{=}0} + (n_\sigma \mathbf{u}_\sigma)\nabla_x u_\sigma^2\right] \\ &= \frac{m_\sigma n_\sigma}{2}\left[\frac{\partial u_\sigma^2}{\partial t} + \mathbf{u}_\sigma \cdot \nabla_x u_\sigma^2\right] \overset{(2.1.29)}{=} n_\sigma \frac{d}{dt}\left(\frac{m_\sigma u_\sigma^2}{2}\right).\end{aligned} \tag{2.1.38}$$

For the second identity it is necessary to form the dot-product (2.1.30) with $\mathbf{u}_\sigma$. For the left-hand side this yields

$$m_\sigma n_\sigma \mathbf{u}_\sigma \cdot \frac{d\mathbf{u}_\sigma}{dt} = m_\sigma n_\sigma \frac{d}{dt}\frac{u_\sigma^2}{2},$$

since pulling the dot product into the derivative will just create a factor of two, due to the partial differentiation. Adding now the right hand-side, still under the assumption of an isotropic pressure tensor, gives the expression

$$m_\sigma n_\sigma \frac{d}{dt}\frac{u_\sigma^2}{2} = n_\sigma q_\sigma \mathbf{u}_\sigma \cdot \mathbf{E} - \mathbf{u}_\sigma \cdot \nabla_x P_\sigma - \mathbf{u}_\sigma \cdot \mathbf{R}_{\sigma\alpha}. \tag{2.1.39}$$

Using both identities, (2.1.38) and (2.1.39), for the second moment equation (2.1.37) yields following simplification:

$$\begin{aligned}&n_\sigma q_\sigma \mathbf{u}_\sigma \cdot \mathbf{E} - \mathbf{u}_\sigma \cdot \nabla_x P_\sigma - \mathbf{u}_\sigma \cdot \mathbf{R}_{\sigma\alpha} + \frac{\partial}{\partial t}\frac{3}{2}P_\sigma + \nabla_x \cdot \left(\mathbf{Q}_\sigma + \frac{5}{2}P_\sigma \mathbf{u}_\sigma\right) \\ &= n_\sigma q_\sigma \mathbf{u}_\sigma \cdot \mathbf{E} - \left(\frac{\partial W}{\partial t}\right)_{E\alpha\sigma} \\ &\frac{\partial}{\partial t}\frac{3}{2}P_\sigma + \left(\frac{5}{2}P_\sigma \nabla_x \cdot \mathbf{u}_\sigma + \frac{5}{2}\mathbf{u}_\sigma \cdot \nabla_x P_\sigma - \mathbf{u}_\sigma \cdot \nabla_x P_\sigma\right) = \frac{3}{2}\underbrace{\left(\frac{\partial}{\partial t}P_\sigma + \mathbf{u}_\sigma \nabla_x P_\sigma\right)}_{=\frac{dP_\sigma}{dt}} + \frac{5}{2}P_\sigma \nabla_x \cdot \mathbf{u}_\sigma \\ &= -\nabla_x \cdot \mathbf{Q}_\sigma + \mathbf{u}_\sigma \cdot \mathbf{R}_{\sigma\alpha} - \left(\frac{\partial W}{\partial t}\right)_{E\alpha\sigma}.\end{aligned}$$

Hence, leaving behind just

$$\frac{3}{2}\frac{dP_\sigma}{dt} + \frac{5}{2}P_\sigma \nabla_x \cdot \mathbf{u}_\sigma = -\nabla_x \cdot \mathbf{Q}_\sigma + \mathbf{u}_\sigma \cdot \mathbf{R}_{\sigma\alpha} - \left(\frac{\partial W}{\partial t}\right)_{E\sigma\alpha}. \tag{2.1.40}$$

2.1.5. From the Two Fluid Equations to the Ideal MHD Equations

So far, two different fluids, one for ions and one for electrons, were treated within the equations given by

$$\begin{aligned}
&\frac{\partial n_\sigma}{\partial t} + \nabla \cdot (n_\sigma \mathbf{u}_\sigma) = 0 \\
&m_\sigma n_\sigma \frac{d\mathbf{u}_\sigma}{dt} = n_\sigma q_\sigma (\mathbf{E} + \mathbf{u}_\sigma \times \mathbf{B}) - \nabla \cdot P_\sigma - \mathbf{R}_{\sigma\alpha} \\
&\frac{3}{2}\frac{dP_\sigma}{dt} + \frac{5}{2} P_\sigma \nabla \cdot \mathbf{u}_\sigma = -\nabla \cdot \mathbf{Q}_\sigma + \mathbf{u}_\sigma \cdot \mathbf{R}_{\sigma\alpha} - \left(\frac{\partial W}{\partial t}\right)_{E\sigma\alpha} \\
&\nabla \times \mathbf{E} = \frac{\partial \mathbf{B}}{\partial t} \\
&\nabla \times \mathbf{B} = \mu_0 (q_i n_i \mathbf{u}_i - e n_e \mathbf{u}_e) + \frac{\partial \mathbf{E}}{\partial t} \\
&\nabla \cdot \mathbf{E} = \frac{1}{\epsilon_0} (q_i n_i - e n_e) \\
&\nabla \cdot \mathbf{B} = 0.
\end{aligned} \tag{2.1.41}$$

Here the corresponding Maxwell equations for the system have been included. Since no velocity derivatives are left, the subscript of the ∇ operator has been dropped. Therefore it will from now on refer just to the spatial derivative. The system of equations in (2.1.41), however, does not yet provide the environment for a closed system. Therefore, further simplifications are necessary. First of all, the high-frequency and short-wavelength information will be removed from the model. Second, a reduction to a single fluid picture is necessary. Third, a collision dominated regime will be prescribed. Fourth, limitations with regards to the characteristic dimensions and the macroscopic size will be applied.

As a starting point, the transformation to the the pre-Maxwell low-frequency equations is perfomed by letting $\epsilon_0 \to 0$. Which implies, that both the net charge $\epsilon_0 \mathbf{E}$ and the displacement current $\epsilon_0 \frac{\partial \mathbf{E}}{\partial t}$ vanish. Hence, the alternate form of Gauss's law requires $q_i n_i = e n_e$. Therefore, both electrons and ions are chosen to carry just the elemental charge e and thus, $n_i = n_e = n$. Further simplification is achieved by ignoring the electron inertia by setting $m_e = 0$. Thus, electrons now have an infinitely fast response time in the system, because of their small mass. Both these assumptions valid for typical fusion plasmas.[4]

As a next step, the introduction of single fluid variables is at hand. Since the influence of the electron mass m_e is being ignored, the mass density can be written as

$$\rho = m_i n. \tag{2.1.42}$$

For the same reason, one can now define the fluid velocity via

$$\mathbf{v} = \mathbf{u}_i, \tag{2.1.43}$$

[4] see Freidberg 2014, 18-19 [7]

since the whole fluid momentum is embedded with the ions. Additionally, a current density may be expressed through the difference between the flow velocities of the ions and electrons so that

$$\mathbf{J} = ne\left(\mathbf{u}_i - \mathbf{u}_e\right). \tag{2.1.44}$$

In the same fashion, an expression for the total pressure is given by the ion and electron contributions:

$$P = P_i + P_e. \tag{2.1.45}$$

With these single fluid variables, $\rho, \mathbf{v}, \mathbf{J}$ and P, it is now possible to derive a single-fluid set of equations from the two-fluid equations (2.1.41). By multiplying the ion mass onto the continuity equation for the ions, the ideal MHD continuity equation is obtained:

$$\begin{aligned} m_i\frac{\partial n}{\partial t} + \nabla\cdot\left(n\mathbf{u}_i\right) &= 0 \\ = \frac{\partial \rho}{\partial t} + \nabla\cdot\left(\rho\mathbf{v}\right) &= 0. \end{aligned} \tag{2.1.46}$$

Furthermore, multiplying both the electron and ion continuity equations with the elementary charge e and then subtracting those equations yields

$$\begin{gathered} \frac{\partial en_i}{\partial t} + \nabla\cdot\left(en_i\mathbf{u}_i\right) - \frac{\partial en_e}{\partial t} - \nabla\cdot\left(en_e\mathbf{u}_e\right) = \nabla\cdot\underbrace{en(\mathbf{u}_i - \mathbf{u}_e)}_{=\mathbf{J}} = 0 \\ \nabla\cdot\mathbf{J} = 0. \end{gathered} \tag{2.1.47}$$

As a next step, the two momentum equations are added together:

$$\begin{aligned} \underbrace{m_i n}_{=\rho}\frac{d\mathbf{v}}{dt} &= ne\left(\mathbf{E} + \mathbf{v}\times\mathbf{B}\right) - \nabla P_i - \underbrace{\mathbf{R}_{ie}}_{\overset{(2.1.4)}{=}-\mathbf{R}_{ei}} - ne\left(\mathbf{E} + \mathbf{u}_e\times\mathbf{B}\right) - \nabla\cdot P_e - \mathbf{R}_{ei} \\ &= \left[\underbrace{ne\left(\mathbf{v} - \mathbf{u}_e\right)}_{=\mathbf{J}}\times\mathbf{B}\right] - \nabla\underbrace{\left(P_i + P_e\right)}_{=P}. \end{aligned}$$

This provides the momentum equation of ideal MHD:

$$\rho\frac{d\mathbf{v}}{dt} - \mathbf{J}\times\mathbf{B} + \nabla P = 0. \tag{2.1.48}$$

Rewriting the electron momentum equation in terms of the single fluid variables will provide the foundation for Ohm's law of the ideal MHD equations:

$$\begin{aligned} \underbrace{m_e}_{=0} n_e\frac{d\mathbf{u}_e}{dt} &= -n_e e\left(\mathbf{E} + \mathbf{u}_e\times\mathbf{B}\right) - \nabla P_e - \mathbf{R}_{ei} \\ ne\mathbf{E} &= \left(\mathbf{J} - \mathbf{u}_i ne\right)\times\mathbf{B} - \nabla P_e - \mathbf{R}_{ei} \\ \mathbf{E} + \mathbf{v}\times\mathbf{B} &= \frac{1}{ne}\left[\mathbf{J}\times\mathbf{B} - \nabla P_e - \mathbf{R}_{ei}\right]. \end{aligned} \tag{2.1.49}$$

For further progression it is necessary to consider the ideal MHD limits, that will provide the closure of the system of equations. As mentioned before, the ideal MHD

equations aim to describe a macroscopic collision dominated plasma. If a system is dominated by collisions or is rather collisionless is largely dependent on the the evolution of the pressure tensor. In other words, one expects the pressure tensor $\mathbf{P}$ to reduce to a scalar isotropic pressure P. This kind of behaviour occurs when the distribution function rapidly reduces into a Maxwellian form. This assumption has already been made, leading to (2.1.48).[5]

Focusing on the right hand side of (2.1.49) it is possible to relate the $\mathbf{J} \times \mathbf{B}$ term to the Hall effect and the ∇P_e term with the electron diamagnetic drift. If those terms are compared to the $\mathbf{v} \times \mathbf{B}$ term on the left-hand side, it can be shown that, if the ion gyro-radius r_g^i is small in comparison to the macroscopic dimension of the plasma a, they are negligible. In other words,

$$\frac{r_g^i}{a} \ll 1.$$

This also implies, that MHD frequencies are essentially lower than the ion gyro-frequencies. [6]

The remaining term $\mathbf{R_{ei}}$, which represents the momentum transfer due to friction between electrons and ions, is dominated by electrical resistivity. It vanishes under the assumption, that the macroscopic dimension is large enough so that the time scale of the resistive diffusion is large enough compared to the typical MHD time scale. The final assumptions concern the energy equation. To be able to neglect the terms on the right-hand side of the energy equation one has to restrict the system in such a way, that the energy equilibration time is short compared to the characteristic time. However, the energy equilibration time has to be still much longer than the momentum exchange time, which implies further restrictions in terms of collisionality. These conditions may be satisfied by setting [7]

$$P_i \approx P_e = \frac{P}{2}. \tag{2.1.50}$$

Therefore, greatly simplifying (2.1.40). Rewriting the continuity equation and using it with the simplified energy equation for ions one obtains the adiabatic relation:

$$\begin{aligned} &\frac{\partial n}{\partial t} + \nabla \cdot (n\mathbf{u}_i) = \frac{\partial n}{\partial t} + n\nabla \cdot \mathbf{u}_i + \mathbf{u}_i \cdot \nabla n = 0 \\ &\frac{1}{n}\frac{dn}{dt} = -\nabla \cdot \mathbf{u}_i. \end{aligned}$$

Here, again the definition for the convective derivative was used.

$$\begin{aligned} &\frac{3}{2}\frac{dP}{dt} + \frac{5}{2}P\nabla \cdot \mathbf{u}_i = 0 \\ &\frac{1}{P}\frac{dP}{dt} = -\frac{5}{3}\nabla \cdot \mathbf{u}_i = \underbrace{\frac{5}{3}}_{=\gamma}\frac{1}{n}\frac{dn}{dt}. \end{aligned}$$

[5] see Freidberg 2014, 22f [7]
[6] see Freidberg 2014, 24 [7]
[7] see Freidberg 2014, 27 [7]

Integrating the equation above provides

$$\frac{P}{n^\gamma} = const. \tag{2.1.51}$$

Therefore, the set of ideal MHD equations is finally completed by the simplified forms of the momentum equations for a single fluid and the low-frequency Maxwell equations:

$$\boxed{\begin{aligned} Continuity\ Equation: &\ \frac{\partial \rho}{\partial t} + \nabla \cdot (\rho \mathbf{v}) = 0 \\ Momentum\ Equation: &\ \rho \frac{d\mathbf{v}}{dt} - \mathbf{J} \times \mathbf{B} + \nabla P = 0 \\ Adiabatic\ Energy\ Relation: &\ \frac{P}{n^\gamma} = const. \\ Ideal\ Ohm's\ Law: &\ \mathbf{E} + \mathbf{v} \times \mathbf{B} = 0 \\ Ampere's\ Law: &\ \nabla \times \mathbf{B} = \mu_0 \mathbf{J} \\ Faraday's\ Law: &\ \nabla \times \mathbf{E} = -\frac{\partial \mathbf{B}}{\partial t} \\ Divergence\ Constraint: &\ \nabla \cdot \mathbf{B} = 0. \end{aligned}} \tag{2.1.52}$$

2.1.6. The Total Energy Functional

The next important physical quantity that is of interest is the total energy contained in, e.g., a confined fusion plasma. To obtain an expression for this energy one may start by building the dot product of $\mathbf{v}$ with the momentum equation:

$$\underbrace{\mathbf{v} \cdot \rho \frac{d\mathbf{v}}{dt}}_{\text{I}} = \underbrace{\mathbf{v} \cdot (\mathbf{J} \times \mathbf{B})}_{\text{II}} - \underbrace{\mathbf{v} \cdot \nabla P}_{\text{III}}.$$

To now obtain the desired form, the three different terms will be treated separately. For the first term I it will be necessary to make use of the mass continuity equation. The goal is to cast it into a similar form $\frac{\partial(\cdots)}{\partial t} + \nabla(\cdots)$. Therefore, one may take a closer look at

$$\begin{aligned} &\frac{\partial(\rho v^2)}{\partial t} + \nabla \cdot \left(\rho \mathbf{v} v^2\right) = v^2 \frac{\partial \rho}{\partial t} + \rho \frac{\partial v^2}{\partial t} + \rho \nabla \cdot \left(\mathbf{v} v^2\right) + \mathbf{v} v^2 \cdot \nabla \rho \\ &= v^2 \left[\frac{\partial \rho}{\partial t} + \mathbf{v} \cdot \nabla \rho\right] + \rho \frac{\partial v^2}{\partial t} + \rho \nabla \cdot \left(\mathbf{v} v^2\right) \\ &= v^2 \left[\underbrace{\frac{\partial \rho}{\partial t} + \nabla \cdot (\mathbf{v} \rho)}_{=0} - \rho \nabla \cdot \mathbf{v}\right] + \rho \frac{\partial v^2}{\partial t} + \rho v^2 \nabla \cdot \mathbf{v} + \mathbf{v} \rho \cdot \nabla v^2 \\ &= \rho \frac{\partial v^2}{\partial t} + \mathbf{v} \rho \cdot \nabla v^2 = 2 \rho \mathbf{v} \cdot \left[\frac{\partial \mathbf{v}}{\partial t} + \mathbf{v} \cdot (\nabla \mathbf{v})\right] = 2 \rho \mathbf{v} \cdot \frac{d\mathbf{v}}{dt}. \end{aligned}$$

This allows one to recast I into the form of

$$\text{I}: \ \rho \mathbf{v} \cdot \frac{d\mathbf{v}}{dt} = \frac{1}{2} \frac{\partial(\rho v^2)}{\partial t} + \nabla \cdot \frac{1}{2} \left(\rho \mathbf{v} v^2\right). \tag{2.1.53}$$

The second term can be transformed by using Ampere's law, Faraday's law and the ideal version of Ohm's law:

$$\begin{aligned}\mathbf{v}\cdot(\mathbf{J}\times\mathbf{B}) &= \mathbf{J}\cdot(\mathbf{B}\times\mathbf{v})\\ &\overset{\substack{Ampere\\Ohm}}{=} \frac{1}{\mu_0}\mathbf{E}\cdot(\nabla\times\mathbf{B})\\ &= \frac{1}{\mu_0}\left[\mathbf{B}\cdot(\nabla\times\mathbf{E}) - \nabla\cdot(\mathbf{E}\times\mathbf{B})\right]\\ &\overset{Faraday}{=} \frac{1}{\mu_0}\left[-\mathbf{B}\cdot\frac{\partial\mathbf{B}}{\partial t} - \nabla\cdot(\mathbf{E}\times\mathbf{B})\right].\end{aligned}$$

Hence, arriving at the form of

$$\text{II}: \ \mathbf{v}\cdot(\mathbf{J}\times\mathbf{B}) = \left[\frac{\partial}{\partial t}\frac{B^2}{2\mu_0} - \nabla\cdot\left(\frac{1}{\mu_0}\mathbf{E}\times\mathbf{B}\right)\right]. \tag{2.1.54}$$

The last term can be rewritten by using the adiabatic relation before the integration:

$$\begin{aligned}\frac{dP}{dt} + \gamma P\nabla\cdot\mathbf{v} &= 0\\ \frac{\partial P}{\partial t} + \mathbf{v}\cdot\nabla P + \gamma\nabla\cdot(P\mathbf{v}) - \gamma\mathbf{v}\cdot\nabla P &= 0\\ \frac{\partial P}{\partial t} + \gamma\nabla\cdot(P\mathbf{v}) &= -\mathbf{v}\cdot\nabla P(1-\gamma).\end{aligned}$$

So, an expression for the third term is found:

$$\text{III}: \ \mathbf{v}\cdot\nabla P = \frac{1}{\gamma-1}\frac{\partial P}{\partial t} + \frac{\gamma}{\gamma-1}\nabla\cdot(P\mathbf{v}). \tag{2.1.55}$$

Combining the contributions from I to III and gathering the partial time derivatives and the spacial variations yields the following expression:

$$\frac{\partial}{\partial t}\underbrace{\left[\frac{1}{2}\rho v^2 + \frac{P}{\gamma-1} + \frac{B^2}{2\mu_0}\right]}_{=w} + \nabla\cdot\underbrace{\left[\frac{1}{2}\rho v^2\mathbf{v} + \frac{1}{\mu_0}\left(\mathbf{E}\times\mathbf{B} + \frac{P}{\gamma-1} + P\mathbf{v}\right)\right]}_{=\mathbf{s}} = 0 \tag{2.1.56}$$

$$\frac{\partial w}{\partial t} + \nabla\cdot\mathbf{s} = 0. \tag{2.1.57}$$

It is now possible to identify w as the total energy of the system which consists of the kinetic, internal and magnetic energy contributions. The quantity s contains the net flux of kinetic and internal energy as well as the mechanical work due to compression of the plasma and the flux of electromagnetic energy. The equation above therefore takes the form of a local conservation relation. To obtain the expression for the global energy, consisting of kinetic, internal and magnetic energies, integration over the whole volume of interest is necessary. Hence, the sum of those energies is given by [8]

$$\mathcal{W} = \int_V \left(\frac{1}{2}\rho v^2 + \frac{P}{\gamma-1} + \frac{B^2}{2\mu_0}\right) d\mathbf{r}. \tag{2.1.58}$$

[8] see Freidberg 2014, 45-47 [7]

2.1.7. Validity of Ideal MHD

During the derivation of the ideal MHD framework several mayor simplifications and assumptions had to be made, to obtain a closed system of mathematically quite convenient equations. Those assumptions can be summarized via three main constrains for the plasma [9]:

- high collisionality
- small ion gyro-radius
- small resistivity

For typical fusion plasmas both the small ion gyro-radius and the small resistivity are well satisfied assumptions. Nevertheless, the requirement for high collisionality is never satisfied to the degree necessary for ideal MHD to be valid. However, comparisons with experimental results show that plasma stability is often predicted by ideal MHD, though the specific physics may strongly differ. The question of why this is the case has several subtle reasons, some of which will be discussed in this chapter.[10] Hence, a further investigation of the errors occurring within the assumptions of ideal MHD is at hand.

First, it is worth noting that for the derivation of the continuity equation none of the above mentioned assumptions have to be made and only effects like recombination, charge exchange, fuel depletion, ionization etc. would prevent a legitimate description of the plasma through this equation. [11]

Second, it is possible to show that the perpendicular motion to the magnetic field in a collisionless plasma is fluid like. This implies that this motion is well described by the ideal MHD momentum equation. The parallel motion, however, is treated wrong most of the time. Anyhow, many plasma motions of interest are incompressible since both expansion and compression are quite stable motions that would prevent certain instabilities. As a consequence a isotropic pressure tensor occurs for fast collisionless plasmas. This, again, means that the part treated wrong by ideal MHD has no influence in those regimes. [12]

Third, the adiabatic energy equation is wrong for typical fusion plasmas but under the consideration of incompressible MHD instabilities provides the same result as the more appropriate limit of a plasma with infinite parallel thermal conductivity. Again, one may work with an equation that is wrong, but in many realistic situations it provides the same result as better approximations.[13]

[9] see Freidberg 2014, 28 [7] and Bellan 2008, 53 [5]
[10] see Freidberg 2014, 28-30 [7]
[11] see Freidberg 2014, 30 [7]
[12] see Freidberg 2014, 30f [7]
[13] see Freidberg 2014, 32 [7]

Last, it can be shown, that ideal MHD treats the inductive part of the electric field correctly but the electrostatic part incorrectly. Since the electric field is only used within Faraday's law, the error from the incorrect part does not matter. This is, because an electrostatic field would be described by a potential Φ via $\nabla\Phi$ and therefore evaluating $\nabla\times\mathbf{E}$ would mathematically annihilate the error. This validates again the neglect of the Hall effect and the electron diamagnetic drift, for both arise from such an electrostatic potential. Nevertheless, resistivity which too is neglected in the ideal Ohm's law appears independently from a electrostatic vector potential. Hence, it will give rise to a kind of motion that is described by the tearing and reconnecting of magnetic field lines. The time scale of such motions is typically on the order of 1 ms and therefore much larger than the MHD time scale. Nevertheless, it provides a suitable upper limit for time periods on which ideal MHD is valid. [14]

2.1.8. Frozen Flux Theorem

An important result of the ideal MHD equations, in particular the ideal version of Ohm's law, is, that the magnetic flux within any open surface area moving along with the described plasma stays constant. In other words, the plasma contains flux surfaces that are "frozen" into it. To show this, one might consider a surface $\mathbf{S}$ with the surface contour C which is penetrated by a magnetic field such that the magnetic flux trough the surface is given by

$$\Psi = \int_S \mathbf{B}\cdot d\mathbf{S}. \tag{2.1.59}$$

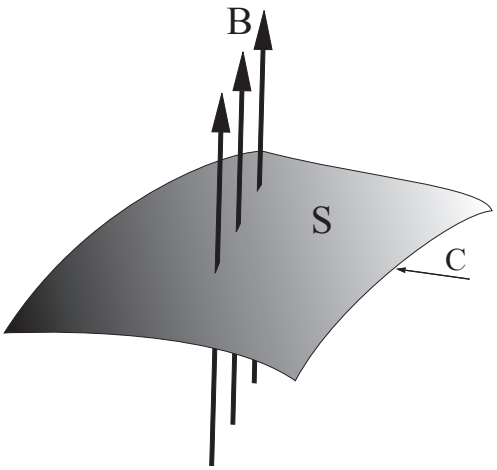

Figure 1: Magnetic flux through the open surface $\mathbf{S}$ with the contour C.

Considering now the change in the flux due to the movement of the surface $\mathbf{S}$, one can write

$$\frac{d\Psi}{dt} = \int_S \frac{\partial\mathbf{B}}{\partial t}\cdot d\mathbf{S} + \int_S \mathbf{B}\cdot\frac{\partial d\mathbf{S}}{\partial t}. \tag{2.1.60}$$

[14] see Freidberg 2014, 26,33 [7]

The first term on the right hand side of the above equation can be recast into a more convenient form by using Faraday's and Ohm's law ((2.1.52)). For the second term a geometric consideration is helpful (see Fig.2). The infinitesimal change of the surface along the contour element $d\mathbf{l}$ due to the movement of the plasma with the velocity $\mathbf{u}$ for the time interval Δt can be expressed via the surface-vector of the surface $\Delta\mathbf{S}$ [15]:

$$\Delta\mathbf{S} = \Delta t\,(\mathbf{u} \times d\mathbf{l})\,.$$

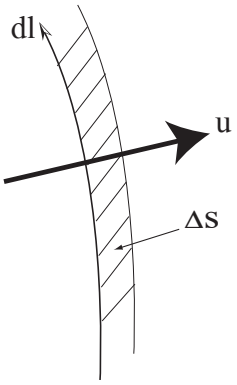

Figure 2: Infinitesimal change of the surface $\mathbf{S}$ due to movement of the plasma with the velocity $\mathbf{u}$ is given by the surface-vector $\Delta\mathbf{S} = \Delta t\,(\mathbf{u} \times d\mathbf{l})$.

Therefore, one might rewrite (2.1.60):

$$\frac{d\Psi}{dt} = \int_S \nabla \times (\mathbf{u} \times \mathbf{B}) \cdot d\mathbf{S} + \int_C \mathbf{B} \cdot (\mathbf{u} \times d\mathbf{l})\,.$$

Applying Stoke's theorem and rearranging the triple product yields

$$\frac{d\Psi}{dt} = \int_C (\mathbf{u} \times \mathbf{B}) \cdot d\mathbf{l} - \int_C (\mathbf{u} \times \mathbf{B}) \cdot d\mathbf{l} = 0.$$

Thus, showing that the magnetic flux is conserved for such a plasma since the surface can be chosen arbitrarily, i.e. it may also be the cross section of the whole plasma:

$$\frac{d\Psi}{dt} = 0. \tag{2.1.61}$$

An other interesting consideration is to form small flux tubes around a magnetic field line, so that this field line is enclosed by a continuation of infinitesimal small surfaces which move with the plasma for a period of Δt at the velocity $\mathbf{u}$. The cross sections may deform but still contain the original plasma. Nevertheless, due to (2.1.61) the magnetic flux does not change. Therefore, the magnetic field line has to move with the fluid which yields that it too is "frozen" into the plasma (see Fig.4).[16]

[15] see D'haeseleer et al. 1991, 53f [4]
[16] see Freidberg 2014, 51-54 [7]

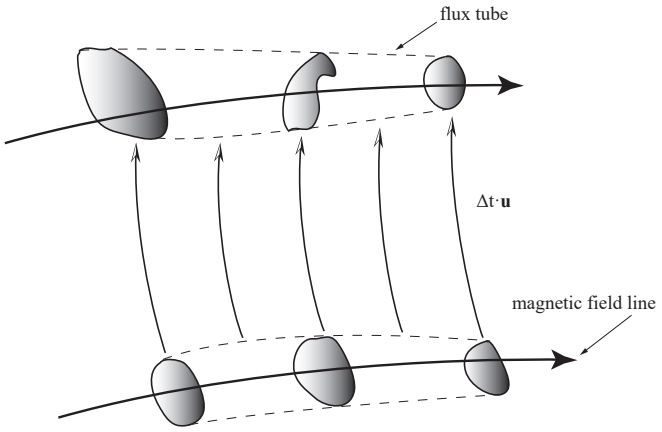

Figure 3: A thin flux tube containing a magnetic field line moves with the plasma for a time Δt at the velocity $\mathbf{u}$. The field line is "frozen" into the fluid.

The requirement of frozen magnetic field lines forms a strong restriction for the plasma under consideration. This is because the magnetic field topology must be conserved for any allowed physical motion within the framework of ideal MHD. Transitions where the magnetic field lines break and reconnect are not allowed due to this behaviour. During the derivation perfectly conducting plasma was assumed. Introducing even a small resistivity could now have drastic effects for the plasma stability for it would break the preserved magnetic topology constraint allowing the inclusion of further kinds of motions. Thus, even lower energy states would be available. Which leads to the conclusion, that the constrain of frozen magnetic field lines provides a solid definition for the assumption of an *ideal* MHD plasma. [17]

2.1.9. Flux Surfaces

If a surface is traced out by a series of magnetic field lines it is referred to as a magnetic surface. If the surface is closed as well the name "flux surface" is typically used within the field of fusion physics. For typical toroidal fusion devices, such surfaces usually exist as nested toroidal surfaces of constant pressure. This can be seen by evaluating the dot product of the magnetic field $\mathbf{B}$ with the static ($\mathbf{v} = 0$) time independent ($\frac{\partial}{\partial t} = 0$) MHD momentum equation [18]:

$$\mathbf{B} \cdot (\mathbf{J} \times \mathbf{B}) = \mathbf{B} \cdot \nabla P.$$

Due to the exchange rules for the triple product one can easily see that the left hand side vanishes and thus obtains

$$\mathbf{B} \cdot \nabla P = 0. \tag{2.1.62}$$

[17] see Freidberg 2014, 51-54 [7]
[18] see D'haeseleer et al. 1991, 54f [4]

Hence, it is seen, that the magnetic field lines lie on the constant pressure contour. From Ampere's law, a current continuity equation may be obtained by taking the gradient:

$$\begin{aligned} \nabla \cdot (\nabla \times \mathbf{B} - \mu_0 \mathbf{J}) &= 0 \\ \nabla \cdot \mathbf{J} &= 0. \end{aligned} \tag{2.1.63}$$

This current continuity in combination with the force balance $(\mathbf{J} \times \mathbf{B}) = \nabla P$ have as a result the so called *current closure condition* which requires the closed loop integral $\oint \frac{dl}{B}$ to be constant on rational surfaces [19], independently on which field line one might start. Violation of this requirement, which is a result due to the approximations made for ideal MHD, may result in the formation of magnetic islands. For axisymmetric devices this requirement is fulfilled, for non-axisymmetric devices this is not true. However, for good confinement of the plasma, it is necessary, that a suitable set of nested toroidal magnetic surfaces exists, whose cross-section in a poloidal pane forms a set of smooth closed curves. [20]

Since those flux surfaces are nested, a special name is given to the degenerate surface of volume zero. It is called the magnetic axis. It forms the center around which the flux surfaces are nested. However, it need not be circular but can take, e.g., even a helical from like in some stellarators. Furthermore, it usually does differ from the geometric center of toroidal devices. [21]

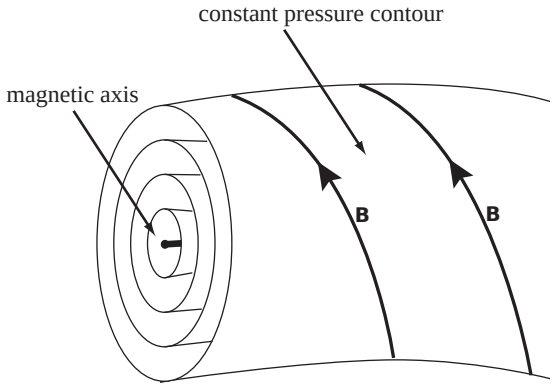

Figure 4: Schematic illustration of different toroidal surfaces of constant pressure including the degenerate surface which is the magnetic axis.

[19] Rational surfaces are surfaces which contain field lines that close upon themselves after one or several transits in the fusion device. The name *rational* arises from the fact, that the ratio of poloidal to toroidal transits of a field line on such surfaces is a rational number.

[20] see D'haeseleer et al. 1991, 65f [4]

[21] see Freidberg 2014, 62-66 [7]

2.1.10. Surface Labels

So far, the flux surfaces have been naturally labelled by the pressure. However, this is not the only label that can be used to distinguish between the surfaces. Actually, any function that is one-dimensional and just pressure dependent would be fit to serve as a label for the flux surfaces. [22]

Calculating for example the polodial flux trough a given pressure contour following (2.1.59) one can see, that it is just pressure dependent (see Fig.5). From a physical point of view this makes sense, since the magnetic lines lie in the constant pressure contours. [23]

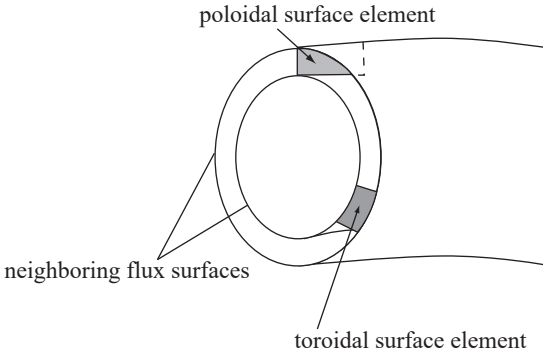

Figure 5: Poloidal and toroidal surface elements $d\mathbf{S}_p$ and $d\mathbf{S}_t$ between two neighboring flux surfaces.

$$\chi = \chi(p) = \int \mathbf{B} \cdot d\mathbf{S}_p. \tag{2.1.64}$$

Analogous to the poloidal flux given in equation (2.1.64) one might also evaluate the toroidal flux:

$$\Phi = \Phi(p) = \int \mathbf{B} \cdot d\mathbf{S}_t. \tag{2.1.65}$$

Both of these fluxes are commonly used to label the flux surfaces when performing MHD calculations. [24]

[22] see Freidberg 2014, 67 [7] and D'haeseleer et al. 1991, 79 [4]
[23] see Freidberg 2014, 66f [7]
[24] see Freidberg 2014, 67 [7]

2.2. Flux Coordinates

An important concept for equilibrium calculations within the framework of the ideal MHD equations is the one of flux coordinates. A common approach for treating physical or mathematical problems is to transform into a coordinate system which naturally describes the geometry of the problem itself, yielding drastic simplifications for calculations. Well known simple examples are, e.g., cylindrical or spherical coordinates. For the treatment of complex magnetic configurations, as the ones appearing in toroidal devices, it is common to perform calculations in a curvilinear coordinate system in which the magnetic field $\mathbf{B}$ and/or $\mathbf{J}$ appear straight. Many such systems exist and one can find an extensive treatment of the most important ones in the book by D'haeseleer et al. [4]. Here, just a short summary of some essential concepts is given and the coordinate system, which will be used within the following chapters, is introduced.

2.2.1. General Curvilinear Coordinates

Considering a position vector $\mathbf{R}(x, y, z)$ in a 3D-space, it is possible to describe this position uniquely by introducing three independent parameters u^1, u^2, u^3 so that a transformation from a Cartesian system to these three parameters $\mathbf{R}(u^1, u^2, u^3)$ can be written as

$$\mathbf{R}(u^1, u^2, u^3): \begin{array}{l} x = x(u^1, u^2, u^3) \\ y = y(u^1, u^2, u^3) \\ z = z(u^1, u^2, u^3). \end{array} \tag{2.2.1}$$

If the Cartesian coordinates also have continuous partial derivatives with respect to the new parameters u^1, u^2, u^3 and the corresponding Jacobian is non-zero, then it is possible to invert the transformation so that

$$\begin{array}{l} u^1 = u^1(x, y, z) \\ u^2 = u^2(x, y, z) \\ u^3 = u^3(x, y, z). \end{array} \tag{2.2.2}$$

If these considerations hold true, one has obtained a set of new coordinates. Within this new coordinate system one might define coordinate surfaces and curves by setting either one (surface) or two (curve) coordinates to a fixed value. However, to describe a point P within the new system in a useful sense, it is necessary to create a *basis* at the given point which so far is described by the position vector $\mathbf{R}$. Such a basis is obtained by forming tangent vectors to the coordinate curves at the point P via the evaluation of

$$\mathbf{e}_1 = \frac{\partial \mathbf{R}}{\partial u^1}, \quad \mathbf{e}_2 = \frac{\partial \mathbf{R}}{\partial u^2}, \quad \mathbf{e}_3 = \frac{\partial \mathbf{R}}{\partial u^3}. \tag{2.2.3}$$

These basis vectors, which are not of unit length, are referred to as the covariant basis vectors. [25]

[25] see D'haeseleer et al. 1991, 10-13 [4]

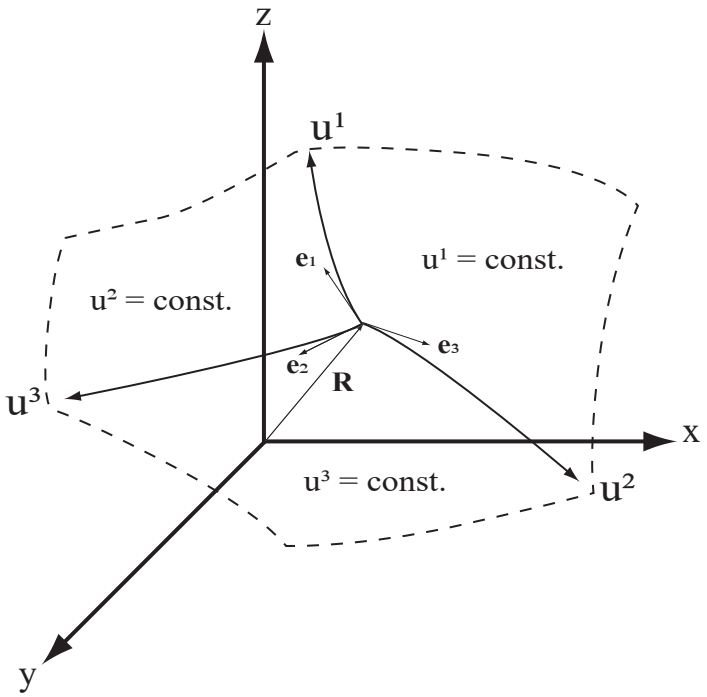

Figure 6: General curvilinear coordinate system with coordinates u^1, u^2 and u^3 with respect to the Cartesian system. The basis vectors $\mathbf{e}^1$, $\mathbf{e}^2$ and $\mathbf{e}^3$ tangent to the coordinate curves and the coordinate surfaces are shown.

Additionally to the co-variant basis vectors, one can find a reciprocal set of basis vectors called the contra-variant basis vectors. In contrast to the co-variant basis vectors, they are not tangent vectors to coordinate curves but rather point in a perpendicular direction with respect to the coordinate *surfaces*. A contra-variant set of basis vectors is given by

$$\nabla u^i = \mathbf{e}^i, \tag{2.2.4}$$

where i can be *1,2* or *3*. They are usually denoted via a superscript and fulfil the relation

$$\mathbf{e}^i \cdot \mathbf{e}_j = \delta^i_j, \tag{2.2.5}$$

where δ^i_j is the Kronecker delta which is zero if $i \neq j$ and one for $i = j$. As mentioned above, the contra-variant basis vectors are reciprocal to the co-variant ones, allowing for a straight forward change between the two bases, if the one set is already known:

$$\begin{aligned} \nabla u^i &= \frac{\mathbf{e}_j \times \mathbf{e}_k}{\mathbf{e}_i \cdot (\mathbf{e}_j \times \mathbf{e}_k)} = \mathbf{e}^i. \\ \frac{\partial \mathbf{R}}{\partial u^i} &= \frac{\mathbf{e}^j \times \mathbf{e}^k}{\mathbf{e}^i \cdot (\mathbf{e}^j \times \mathbf{e}^k)} = \mathbf{e}_i. \end{aligned} \tag{2.2.6}$$

The indices i,j and k must be chosen as circular permutations of *1,2* and *3*.
An arbitrary vector $\mathbf{D}$ can now be expressed in either basis via its co- or contra-

variant components which are given by

$$\begin{aligned} D_i &\equiv \mathbf{D} \cdot \mathbf{e}_i \\ D^i &\equiv \mathbf{D} \cdot \mathbf{e}^i. \end{aligned} \tag{2.2.7}$$

Hence, the full vector may be written as

$$\begin{aligned} \mathbf{D} &\equiv D^1 \mathbf{e}_1 + D^2 \mathbf{e}_2 + D^3 \mathbf{e}_3 \\ \mathbf{D} &\equiv D_1 \mathbf{e}^1 + D_2 \mathbf{e}^2 + D_3 \mathbf{e}^3. \end{aligned} \tag{2.2.8}$$

The Jacobian $\mathcal{J}$ of the transformation from Cartesian to the covariant curvilinear coordinates can be written via

$$\mathcal{J} = \frac{\partial \mathbf{R}}{\partial u^1} \cdot \frac{\partial \mathbf{R}}{\partial u^2} \times \frac{\partial \mathbf{R}}{\partial u^3} = \mathbf{e}_1 \cdot \mathbf{e}_2 \times \mathbf{e}_3 \tag{2.2.9}$$

and it can be shown with the help of (2.2.6), that the Jacobian of the transformation to the co-variant system is nothing else but the inverse of the contra-variant Jacobian [26]:

$$\mathfrak{J} = \nabla u^1 \cdot \nabla u^2 \times \nabla u^3 = \mathbf{e}^1 \cdot \mathbf{e}^2 \times \mathbf{e}^3 \overset{(2.2.6)}{=} \mathcal{J}^{-1}. \tag{2.2.10}$$

An other useful concept, especially when dealing with co- and contra-variant components, are the metric coefficients g_{ij} and g^{ij}. They are defined via

$$g_{ij} = \mathbf{e}_i \cdot \mathbf{e}_j = \frac{\partial \mathbf{R}}{\partial u^i} \cdot \frac{\partial \mathbf{R}}{\partial u^j} \tag{2.2.11}$$

and

$$g^{ij} = \mathbf{e}^i \cdot \mathbf{e}^j = \nabla u^i \cdot \nabla u^j. \tag{2.2.12}$$

and are symmetric, i.e. $g^{ij} = g^{ji}$ and $g_{ij} = g_{ji}$. They allow to easily switch between co- and contra-variant components of a vector:

$$\begin{aligned} D_i &= \sum_j g_{ij} D^j. \\ D^i &= \sum_j g^{ij} D_j. \end{aligned} \tag{2.2.13}$$

Furthermore, the metric coefficients allow the evaluation of a dot-product between two vectors $\mathbf{X}$ and $\mathbf{Y}$ via

$$\mathbf{X} \cdot \mathbf{Y} = \sum_{ij} g_{ij} X^i Y^j = \sum_{ij} g^{ij} X_i Y_j. \tag{2.2.14}$$

The matrix consisting of the metric coefficients is called the metric tensor $\mathcal{G} = [g_{ij}]$. The relation between the metric tensor and its determinant g with the Jacobian too is quite useful and simple:

$$det\,(\mathcal{G}) = g = (\mathcal{J})^2. \tag{2.2.15}$$

Also, the metric tensor for the co-variant system is nothing but the inverse of the tensor for the contra-variant one:

$$\mathcal{G} = [g_{ij}] = \left[g^{ij}\right]^{-1}. \tag{2.2.16}$$

This yields, that the determinants are the same [27]:

$$g = det\,(\mathcal{G}) = det\left[g^{ij}\right]^{-1}. \tag{2.2.17}$$

[26] see D'haeseleer et al. 1991, 23f [4]

[27] see D'haeseleer et al. 1991, 20-22 and 25 [4]

2.2.2. Straight Field Line Coordinates

With the foundation provided by a general curvilinear coordinate system it is now quite straight-forward to create a system which is tailored to the problems and questions arising with the theoretical treatment of fusion plasmas and in more specific terms ideal MHD. The first coordinate which will be introduced is one, that is able to act as a surface label. For the general considerations the coordinate will be labelled with $\mathfrak{r} \equiv u^1$. Since toroidal and/or cylindrical systems are the main focus, it is just natural to keep a poloidal and toroidal angle coordinate. Since the goal is to simplify equations with respect to $\mathbf{B}$ and/or $\mathbf{J}$, those angles will be generalized as well. Therefore, one ends up with a polodial angle θ whose coordinate surfaces are centred around the magnetic axis and take partial-cone like shapes. Analogously, the flux coordinate version of a toroidal angle ζ has coordinate surfaces that touch the major axis and cut the flux surfaces.

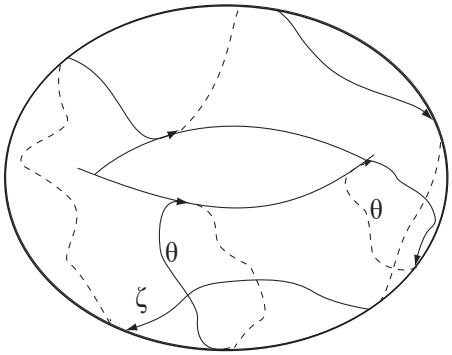

Figure 7: Coordinate curves for the general angle like coordinates θ and ζ in a toroidal system.

Considering the magnetic field $\mathbf{B}$, one may write it in terms of its contra-variant components:

$$\mathbf{B} = B^{\mathfrak{r}}\mathbf{e}_{\mathfrak{r}} + B^{\theta}\mathbf{e}_{\theta} + B^{\zeta}\mathbf{e}_{\zeta}. \tag{2.2.18}$$

Since the flux surface label has to fulfil the relation defining flux surfaces, one can easily see that the contra-variant magnetic field component in the direction of the flux label vanishes:

$$\mathbf{B} \cdot \nabla\mathfrak{r} = 0 \rightarrow B^{\mathfrak{r}} = 0. \tag{2.2.19}$$

Furthermore, it is possible to replace the co-variant basis vectors with the contra-variant ones using (2.2.6) and replacing the denominator by the Jacobian $\mathcal{J}$ ((2.2.9)) or equivalently with $\sqrt{g}$ ((2.2.15)). With this, the expression for the magnetic field can be expanded:

$$\mathbf{B} = B^{\theta}\sqrt{g}\left(\nabla\zeta \times \nabla\mathfrak{r}\right) + B^{\zeta}\sqrt{g}\left(\nabla\mathfrak{r} \times \nabla\theta\right). \tag{2.2.20}$$

Applying now the divergence constrain $\nabla \cdot \mathbf{B} = 0$ one arrives at an equation that suggest a dependence of B^{θ} and B^{ζ} from a single function that will be referred to

as $\nu \equiv \nu(\mathfrak{r}, \theta, \zeta)$. A useful vector relation for this is

$$\begin{aligned}\left[\nabla \times a\nabla b\right]_i &= \epsilon_{ijk}\partial_j(a\partial_k b) = \epsilon_{ijk}\left[(\partial_j a)(\partial_k b) + a\partial_j(\partial_k b)\right] \\ &= \left[\nabla a \times \nabla b\right]_i + a\underbrace{\left(\nabla \times \nabla b\right)}_{=0}.\end{aligned} \tag{2.2.21}$$

Thus yielding,

$$\begin{aligned}\nabla \cdot \mathbf{B} &= (\nabla B^\theta \sqrt{g})\frac{\mathbf{e}_\theta}{\sqrt{g}} + B^\theta\sqrt{g}\underbrace{\left[\nabla \cdot (\nabla \times \zeta\nabla\mathfrak{r})\right]}_{=0} + (\nabla B^\zeta\sqrt{g})\frac{\mathbf{e}_\zeta}{\sqrt{g}} + B^\zeta\sqrt{g}\underbrace{\left[\nabla \cdot (\nabla \times \mathfrak{r}\nabla\theta)\right]}_{=0} \\ &= \frac{\partial}{\partial\theta}\sqrt{g}B^\theta + \frac{\partial}{\partial\zeta}\sqrt{g}B^\zeta = 0.\end{aligned} \tag{2.2.22}$$

The above equation can be satisfied if the dependencies of B^θ and B^ζ are for example expressed via

$$\begin{aligned}B^\theta &= -\frac{1}{\sqrt{g}}\frac{\partial\nu}{\partial\zeta} \\ B^\zeta &= \frac{1}{\sqrt{g}}\frac{\partial\nu}{\partial\theta}.\end{aligned} \tag{2.2.23}$$

Therefore, (2.2.20) can be rewritten using the exchange identities for the cross-product as

$$\mathbf{B} = \nabla\mathfrak{r} \times \left(\underbrace{\frac{\partial\nu}{\partial\mathfrak{r}}\nabla\mathfrak{r}}_{=0} + \frac{\partial\nu}{\partial\zeta}\nabla\zeta + \frac{\partial\nu}{\partial\theta}\nabla\theta\right) = \nabla\mathfrak{r} \times \nabla\nu. \tag{2.2.24}$$

The first term in the bracket can be added for it vanishes anyway due to the cross product rules for the ∇-operator. Eq. (2.2.24) corresponds to a Clebsch form of the coordinate system[28]. From the consideration, that the magnetic field as a physical quantity needs to be single valued, one can deduce that the function ν must be periodic in θ and ζ but has an arbitrary dependence on $\mathfrak{r}$. A general form for this function ν can thus be expressed via a polynomial of the form [29]

$$\nu(\mathfrak{r}, \theta, \zeta) = C_1(\mathfrak{r})\theta + C_2(\mathfrak{r})\zeta + \tilde{\nu}(\mathfrak{r}, \theta, \zeta). \tag{2.2.25}$$

The parameters C_1 and C_2 are just as of now arbitrarily dependent on $\mathfrak{r}$ and the function $\tilde{\nu}$ represents a periodic function in θ and ζ. Applying the identity (2.2.21) onto the Clebsch form enables one to write the magnetic field derived from a vector potential $\mathbf{A}$ as

$$\mathbf{B} \overset{(2.2.21)}{=} \nabla \times \mathfrak{r}\nabla\nu = \nabla \times \mathbf{A}. \tag{2.2.26}$$

[28] Clebsch coordinates are a set of coordinates which originate from fluid mechanics and describe the system via functions that are constant along a stream line (stream functions). The stream functions occurring in (2.2.24) would be $\mathfrak{r}$ and ν.

[29] see D'haeseleer et al. 1991, 118 [4]

The goal now is to identify the two $\mathfrak{r}$-dependent functions and find a suitable way to deal with $\tilde{\nu}$. To tackle this problem, one uses a form-invariant expression for the toroidal and poloidal flux ((2.1.65) and (2.1.64)). Starting from the integral over a flux surface volume V with the elementary volume element d^3R,

$$\iiint_V d^3R\ \mathbf{B}\cdot\nabla\zeta = \iiint_V d^3R\nabla\cdot(\mathbf{B}\zeta), \tag{2.2.27}$$

it is possible to apply Gauss' theorem and split up the surface integral yielding

$$\iiint_V d^3R\ \nabla\cdot(\mathbf{B}\zeta) \overset{Gauss}{=} \oiint_S \zeta\mathbf{B}\cdot d\mathbf{S} = \iint_{S_{torus}} \zeta\mathbf{B}\cdot d\mathbf{S} + \iint_{S_{\zeta=2\pi}} \zeta\mathbf{B}\cdot d\mathbf{S} + \iint_{S_{\zeta=0}} \zeta\mathbf{B}\cdot d\mathbf{S}. \tag{2.2.28}$$

For the last step, the volume of the torus like flux surface was cut open at the $\zeta = 0$ and equivalently the $\zeta = 2\pi$ surfaces. Therefore, the volume is described by these three limiting surfaces.

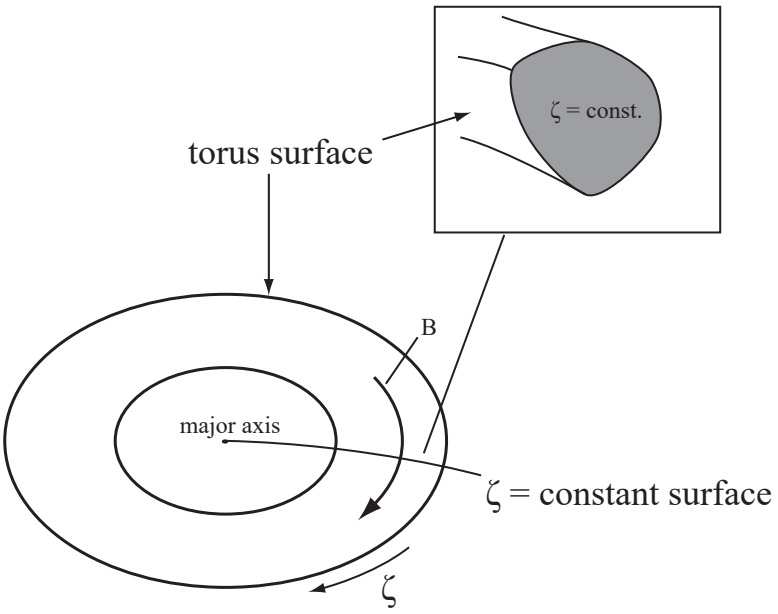

Figure 8: Top view of the toroid like flux surface together with the $\zeta = 0$ and the $\zeta = 2\pi$ plane. The grey area indicates a constant ζ-surface limited by the torus surface S_{torus}

Since the magnetic field $\mathbf{B}$ is always perpendicular to the the surface vector of the torus surface it is possible to drop the first term. For the two other terms one has to set ζ to either zero or 2π which just leaves

$$\iiint_V d^3R\ \mathbf{B}\cdot d\mathbf{S} = 2\pi \iint_{S_{\zeta=2\pi}} \mathbf{B}\cdot d\mathbf{S}. \tag{2.2.29}$$

Identifying the surface $S_{\zeta=2\pi}$ as the surface area which previously was referred to as S_{tor} it is possible to arrive at the desired form of the toroidal flux:

$$\Phi = \frac{1}{2\pi} \iiint_V \mathbf{B} \cdot \nabla\zeta d^3R. \tag{2.2.30}$$

With analogous considerations the poloidal flux may be written as

$$\chi = \frac{1}{2\pi} \iiint_V \mathbf{B} \cdot \nabla\theta d^3R. \tag{2.2.31}$$

Considering the derivative of the toroidal flux with respect to the flux label,

$$\Phi' = \frac{d\Phi}{d\mathfrak{r}} = \frac{d}{d\mathfrak{r}} \frac{1}{2\pi} \iiint_V \mathbf{B} \cdot \nabla\zeta \sqrt{g}\, d\mathfrak{r}d\theta d\zeta = \frac{1}{2\pi} \iint_S \mathbf{B} \cdot \nabla\zeta \sqrt{g}\, d\theta d\zeta. \tag{2.2.32}$$

Here, the infinitesimal volume element d^3R was replaced by the corresponding expression within the new coordinate system $\sqrt{g}\, d\mathfrak{r}d\theta d\zeta$. Since $\nabla\zeta$ is nothing more than a contra-variant basis vector it is possible to substitute $\mathbf{B}\nabla\zeta$ with the contra-variant component for the magnetic field as given by (2.2.23). Additionally, the derivative of ν can be calculated with the general form of ν (2.2.25):

$$\begin{aligned} \Phi' &= \frac{1}{2\pi} \int_0^{2\pi} \int_0^{2\pi} d\theta d\zeta \sqrt{g} \underbrace{\frac{1}{\sqrt{g}} \frac{\partial\nu}{\partial\theta}}_{(2.2.23)} \\ &= \frac{1}{2\pi} \int_0^{2\pi} \int_0^{2\pi} d\theta d\zeta \left(C_1(\mathfrak{r}) + \frac{\partial\tilde{\nu}}{\partial\theta} \right) = 2\pi C_1(\mathfrak{r}). \end{aligned} \tag{2.2.33}$$

The integration of $\frac{\partial\tilde{\nu}}{\partial\theta}$ vanishes since it is periodic in θ. The equivalent procedure can be performed for the poloidal flux yielding

$$\chi' = -2\pi C_2(\mathfrak{r}). \tag{2.2.34}$$

Combining everything calculated so far, the following expression for the function ν is obtained:

$$\nu = \frac{1}{2\pi} \left(\Phi'\theta - \chi'\zeta \right) + \tilde{\nu}(\mathfrak{r}, \theta, \zeta). \tag{2.2.35}$$

The final question that has to be answered is how the periodic function $\tilde{\nu}$ is handled. One legitimate choice is to absorb it into one of the angular coordinates since they can be shifted by any 2π-*periodic* function. For instance, including it within θ yields

$$\begin{aligned} \theta^* &= \theta + 2\pi \frac{\tilde{\nu}}{\Phi'} \\ \zeta^* &= \zeta \\ \nu(\mathfrak{r}, \theta^*, \zeta^*) &= \frac{1}{2\pi} \Phi'\theta^* - \frac{1}{2\pi} \chi'\zeta^*. \end{aligned} \tag{2.2.36}$$

Therefore, an equation for a straight line in (θ, ζ) coordinates is obtained by setting $\nu = constant$:

$$\Phi'\theta^* - \chi'\zeta = constant. \tag{2.2.37}$$

Consequently a suitable set of straight field line/ flux coordinates is obtained. Variations may occur due to the choice of the flux label and/or the treatment of the potential like ν-function. [30]

[30] see D'haeseleer et al. 1991, 116-122 [4]

3. The Galerkin Variational Equilibrium Code (GVEC)

All of the previously discussed derivations, concepts and explanations were presented to provide the theoretical foundation for the central focus of this thesis which evolves around the equilibrium code GVEC.

GVEC allows the calculation of equilibrium configurations of the magnetic field within the framework of ideal MHD. This is achieved by applying a minimization algorithm onto the total energy functional W_{MHD}. To allow for a proper understanding of the work done within this thesis and the alterations and expansions that were performed within the code, a brief overview of the code documentation done by F.Hindenlang and O.Maj [6] is given in this chapter. Additionally, the theoretical descriptions of the alternative mappings for the magnetic field topology are introduced.

3.1. Coordinates and Magnetic Field Definition

Due to the convenient straight field line properties, calculations in GVEC are performed in a special flux coordinate system of Clebsch-form which are referred to as PEST-coordinates[31]. The flux label s is chosen such that

$$s \equiv \mathfrak{r} \sim \sqrt{\Phi}(s). \tag{3.1.1}$$

As a consequence, it is possible to write the toroidal flux $\Phi(s)$ as a function depending on the toroidal flux on the last flux surface via

$$\Phi(s) = \Phi^{edge} s^2 \Rightarrow \hat{\Phi} = \frac{\Phi(s)}{\Phi^{edge}}. \tag{3.1.2}$$

This choice sets $s = 0$ at the magnetic axis and $s = 1$ on the outer most closed flux surface. For the expression of the polodial flux, the definition of the so called *rotational transform* ι is used:

$$\iota\left(\hat{\Phi}(s)\right) = \frac{d\chi}{d\Phi} = \frac{\chi'}{\Phi'} \Rightarrow \chi(s) = \int_{\tilde{s}}^{s} \iota\left(\hat{\Phi}(\tilde{s})\right) \Phi'(\tilde{s}) d\tilde{s}. \tag{3.1.3}$$

The poloidal straight field line angle coordinate θ^* is maintained in the form with a potential term λ and a counter-clockwise poloidal angle $\theta \in [0, 2\pi]$ so that

$$\theta^* = \theta + \lambda. \tag{3.1.4}$$

The third coordinate is given by a toroidal angle ζ:

$$\zeta^* = \zeta \in [0, 2\pi]. \tag{3.1.5}$$

Hence, a defining vector potential may be written by recalling (2.2.26) via

$$\mathbf{A} = \Phi(s)\nabla\theta^* - \chi(s)\nabla\zeta = \Phi(s)\nabla\left(\theta + \lambda\right) - \chi(s)\nabla\zeta. \tag{3.1.6}$$

[31] In this system $\zeta = -\phi$, given a cylindrical coordinate system (R, ϕ, Z), see Kruger and Greene Phys.Plasmas 26, 082506-8 [9]

From this vector potential, a magnetic field can be calculated:

$$\begin{aligned}\mathbf{B} = \nabla \times \mathbf{A} &= \Phi' \nabla s \times \nabla (\theta + \lambda) - \chi' \nabla s \times \nabla \zeta \\ &= \Phi' \nabla s \times \left(\nabla \theta + \lambda_{\dot{\theta}} \nabla \theta + \lambda_{\dot{\zeta}} \nabla \zeta\right) - \chi' \nabla s \times \nabla \zeta \\ &= \Phi' \left(1 + \lambda_{\dot{\theta}}\right) \nabla s \times \nabla \theta + \left(\Phi' \lambda_{\dot{\zeta}} - \chi'\right) \nabla s \times \nabla \zeta \\ &= \Phi' \left(1 + \lambda_{\dot{\theta}}\right) \nabla s \times \nabla \theta + \left(\chi' - \Phi' \lambda_{\dot{\zeta}}\right) \nabla \zeta \times \nabla s.\end{aligned}$$

Hereby, the chain rule $\nabla C(s) = C'(s) \nabla s$ was used. The lower indices with $\dot{\theta}$ and $\dot{\zeta}$ symbolize derivatives with respect to these coordinates. Recasting the cross-products with the help of (2.2.6) and (2.2.10) in the form of co-variant basis vectors allows for the identification of the contra-variant components. Again the flux label component B^s vanishes as described in (2.2.19):

$$\mathbf{B} = B^{\zeta} \mathbf{e}_{\zeta} + B^{\theta} \mathbf{e}_{\theta} = \Phi' \left(1 + \lambda_{\dot{\theta}}\right) \frac{\mathbf{e}_{\zeta}}{\mathcal{J}} + \left(\chi' - \Phi' \lambda_{\dot{\zeta}}\right) \frac{\mathbf{e}_{\theta}}{\mathcal{J}} \tag{3.1.7}$$

$$\begin{aligned} B^{\theta} &= \frac{1}{\mathcal{J}} \underbrace{\left(\chi' - \Phi' \lambda_{\dot{\zeta}}\right)}_{\equiv b^{\theta}} \\ B^{\zeta} &= \frac{1}{\mathcal{J}} \underbrace{\Phi' \left(1 + \lambda_{\dot{\theta}}\right)}_{\equiv b^{\zeta}}. \end{aligned} \tag{3.1.8}$$

With the help of the metric coefficients the co-variant components are easily calculated (compare (2.2.13)):

$$\begin{aligned} B_s &= g_{s\theta} B^{\theta} + g_{s\zeta} B^{\zeta} \\ B_{\theta} &= g_{\theta\theta} B^{\theta} + g_{\theta\zeta} B^{\zeta} \\ B_{\zeta} &= g_{\zeta\theta} B^{\theta} + g_{\zeta\zeta} B^{\zeta}. \end{aligned} \tag{3.1.9}$$

3.2. The Energy Functional

As mentioned before, GVEC calculates equilibrium configurations within the framework of ideal MHD by minimizing the corresponding energy functional. Recall the form of the total energy as given by (2.1.57). Assuming velocity $v = 0$, multiplying by μ_0 and expressing the $\mathbf{B}^2$ term via the dot product of $\mathbf{B} \cdot \mathbf{B}$ using (2.2.14) gives the energy-functional the form of

$$W = \mu_0 \mathcal{W}(v = 0) = \int_V \left(\mu_0 \frac{P(s)}{\gamma - 1} + \frac{1}{2} \sum_{\xi\omega} B^{\xi} g_{\xi\omega} B^{\omega} \right) d\mathbf{r}. \tag{3.2.1}$$

Hereby, the indices $\xi, \omega \in (\theta, \zeta)$ represent the summation over the two angular coordinates. The pressure profile $P(s)$ is defined via the mass profile over the normalized toroidal flux so that the adiabatic conservation of mass between neighboring flux surfaces is fulfilled (compare (2.1.52)) [32]:

$$P(s) \equiv P(\hat{\Phi}(s)) = \frac{m(\hat{\Phi}(s))}{[V'(s)]^{\gamma}}. \tag{3.2.2}$$

[32] see Hirshman and Whitson Phys.Fluids 1983, 3555 [10]

In this context $V'(s)$ represents the radial derivative of the volume between two flux surfaces obtained by integrating the Jacobian with respect to the angular coordinates:

$$V'(s) = \int_0^{2\pi}\int_0^{2\pi} \mathcal{J}\, d\theta d\zeta. \tag{3.2.3}$$

This form implies that during the variation of the pressure $P(s)$ only the $V'(s)$ term, which is, in contrast to $m(\hat{\Phi}(s))$, dependent on the geometry of the flux surface, varies. Using these definitions, the expression for the infinitesimal volume element in the flux-coordinate system $d\mathbf{r} = \mathcal{J} ds d\theta d\zeta$ and the previously derived form of the contra-variant components of the **B**-field (3.1.8), a more explicit expansion of the energy functional is possible:

$$W = \int_0^1 \left(\mu_0 \frac{1}{\gamma - 1} \frac{m(\hat{\Phi}(s))}{[V'(s)]^\gamma} V'(s) + \int_0^{2\pi}\int_0^{2\pi} \frac{1}{2\mathcal{J}} \sum_{\xi\omega} b^\xi g_{\xi\omega} b^\omega d\theta d\zeta \right) ds. \tag{3.2.4}$$

3.3. Coordinate Mapping and Variation of the Energy Functional

Given now a prescribed pressure profile as well as the toroidal flux and the form of the rotational transform, an equilibrium configuration for the system contained in W can be obtained. This is achieved by minimizing the energy functional with respect to the geometry of the problem. In GVEC, only a ‚fixed-boundary' approach is available, meaning that the geometry of the outermost flux surface ($s = 1$) is given and remains fixed. In the free-boundary approach, not considered here, the outermost flux surface would be allowed to move while being coupled to an external coil field. The independent variables influencing the variation of the energy are naturally chosen to be the flux coordinates (s, θ, ζ). As a consequence, the inverse transformation from the flux coordinates to a real space system would introduce the real space coordinates as dependent variables. A standard choice of these real space coordinates would be for example cylindrical/torus coordinates $(R(s,\theta,\zeta), Z(s,\theta,\zeta), \phi)$ which are again easily used to calculate Cartesian coordinates. GVEC, however, provides a variety of different choices for this kind of mapping onto the real space. Therefore, these dependent real space coordinates will be referred to as (X^1, X^2, ζ). Still, in all applications shown in this work, only the cylindrical coordinate system with $(X^1, X^2, \zeta) \to (R, Z, \phi)$ will be used.

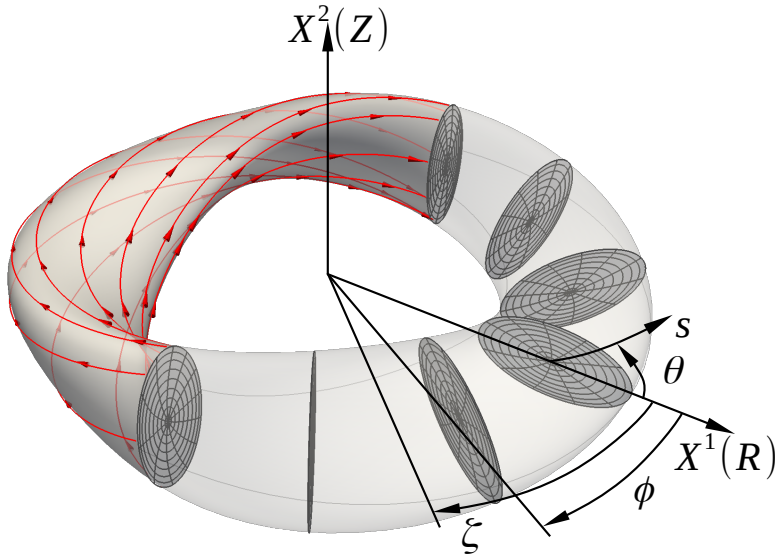

Figure 9: Cylindrical real space coordinates $(R, \phi, Z) \equiv \left(X^1, \zeta, X^2\right)$ and flux coordinates $(\mathrm{s}, \theta, \zeta)$.[33]

In that sense, one works with coordinates so that a representation of Cartesian coordinates (x, y, z) is given by a dependence onto the real space coordinates (X^1, X^2, ζ) which again are dependent on the flux coordinates $(\mathrm{s}, \theta, \zeta)$. Therefore, it is possible to write the Jacobian of the whole transformation $\mathcal{J}$ as a product of the Jacobian from the transformation to real space coordinates

$$\mathcal{J}_p : (s, \theta, \zeta) \to (X^1, X^2, \zeta) \tag{3.3.1}$$

and the Jacobian from the transformation of the real space coordinates to the Cartesian system

$$\mathcal{J}_h : (X^1, X^2, \zeta) \to (x, y, z). \tag{3.3.2}$$

This might be easily proven by applying the chain and product rule while calculating the derivatives of the Cartesian coordinates with respect to the flux coordinates and henceforth the corresponding Jacobian. Note that in the case of the cylindrical coordinate system $J_h = R$.

$$\mathcal{J} = \mathcal{J}_h \mathcal{J}_p. \tag{3.3.3}$$

The index p symbolizes *poloidal* since the Jacobian $\mathcal{J}_p$, for which $\partial_s \zeta = 0$ and $\partial_\theta \zeta = 0$, takes the following form:

$$\mathcal{J}_p = \partial_s X^1 \partial_\theta X^2 \partial_\zeta \zeta - \partial_\theta X^1 \partial_s X^2 \partial_\zeta \zeta = X^1_{\dot{s}} X^2_{\dot{\theta}} - X^1_{\dot{\theta}} X^2_{\dot{s}}. \tag{3.3.4}$$

So far no explicit dependence of the real space coordinates X^1 and X^2 was given. In general, they will depend on some parameters coupling (s, θ, ζ). These parameters are degrees of freedom (DOFs) which can be tuned and twisted to prescribe a different configuration onto the system. It can be shown, as discussed and applied by Hirshman and Whitson [10], that vanishing forces onto these coefficients

[33] This figure was kindly provided by F. Hindenlang

provide a minimum in the energy functional and therefore an equilibrium configuration. Hence, the evaluation of the variation of the energy functional with respect to an (arbitrary) combined Fourier-spline coefficient η is at hand. Applying such a variation onto the functional (3.2.4) yields

$$\begin{aligned} -\frac{dW}{d\eta} &= \frac{d}{d\eta}\int_0^1 \left(\mu_0 \frac{m\left(\hat{\Phi}(s)\right)}{1-\gamma}\left(V'(s)\right)^{(1-\gamma)}\right) - \frac{1}{2}\int_0^{2\pi}\int_0^{2\pi}\frac{1}{2\mathcal{J}}\sum_{\xi\omega} b^{\xi} g_{\xi\omega} b^{\omega} d\theta d\zeta\Bigg) ds \\ &= \int_0^1 \left(\mu_0 \frac{m\left(\hat{\Phi}(s)\right)}{\left(V'(s)\right)^{\gamma}}\frac{dV'(s)}{d\eta} - \frac{1}{2}\sum_{ij}\left\langle\!\!\left\langle \frac{dL_B(s)}{d\eta}\right\rangle\!\!\right\rangle\right) ds. \end{aligned} \tag{3.3.5}$$

Since the mass profile $m\left(\hat{\Phi}(s)\right)$ is prescribed, it is not affected by the variation. The $\langle\!\langle\rangle\!\rangle$-brackets denote the integration over the two angle coordinates and are introduced for the sake of readability. For the angular surface term $V'(s)$ only the Jacobian is affected by the variation so that

$$\frac{dV'(s)}{d\eta} = \left\langle\!\!\left\langle \frac{d\mathcal{J}}{d\eta}\right\rangle\!\!\right\rangle. \tag{3.3.6}$$

The quantity $L_B(s)$ contains the variation of the magnetic field:

$$\frac{dL_B(s)}{d\eta} = \frac{1}{\mathcal{J}}\left[b^{\xi} b^{\omega}\frac{dg_{\xi\omega}}{d\eta} + 2g_{\xi\omega}b^{\xi}\frac{db^{\omega}}{d\eta} - \frac{b^{\xi}g_{\xi\omega}b^{\omega}}{\mathcal{J}}\frac{d\mathcal{J}}{d\eta}\right]. \tag{3.3.7}$$

Since one is free to choose the indices over the summation, it is possible to gather the two variations of the b^i and b^j in the second term of the bracket. The variation of the poloidal Jacobian $\mathcal{J}_p$ can be easily calculated by recalling (3.3.4). The Jacobian $\mathcal{J}_h$, however, depends on the mapping choice which connects the real space coordinates to the Cartesian coordinates and thus, has to be left in the more general form:

$$\frac{d\mathcal{J}}{d\eta} = \mathcal{J}_h\left(X^1_{\dot{s}}\frac{dX^2_{\dot{\theta}}}{d\eta} - X^2_{\dot{s}}\frac{dX^1_{\dot{\theta}}}{d\eta} + X^2_{\dot{\theta}}\frac{dX^1_{\dot{s}}}{d\eta} - X^1_{\dot{\theta}}\frac{dX^2_{\dot{s}}}{d\eta}\right) + \mathcal{J}_p\sum_k\left(\frac{\partial\mathcal{J}_h}{\partial X^k}\frac{dX^k}{d\eta}\right). \tag{3.3.8}$$

Where $k \in (1,2)$ since the derivative of the third real space coordinate ζ is zero, i.e. $\frac{d\zeta}{d\eta} = 0$. For the components of the magnetic field, the variation too is straight forward, since the only affected parameter is λ. With the definitions from (3.1.8) it follows, assuming again the prescribed $\Phi(s)$ and $\iota(\hat{\Phi}(s))$ profiles, that

$$\frac{db^{\theta}}{d\eta} = -\Phi'(s)\frac{d\lambda_{\dot{\zeta}}}{d\eta}, \quad \frac{db^{\zeta}}{d\eta} = \Phi'(s)\frac{d\lambda_{\dot{\theta}}}{d\eta}. \tag{3.3.9}$$

The variation of the metric coefficients has to be treated with more care. Since the mapping between the flux coordinates and the Cartesian system is done with the help of the coordinates (X^1, X^2, ζ) one can write the overall metric coefficients g_{ij} with the help of the metric tensor $\mathcal{G}$ for the transformation from $\mathbf{q} = (X^1, X^2, \zeta)$ to (x, y, z). For example, in the cylindrical coordinates

$$\mathcal{G} = \begin{bmatrix} 1 & 0 & 0 \\ 0 & 1 & 0 \\ 0 & 0 & R^2 \end{bmatrix}. \tag{3.3.10}$$

In that sense, the metric coefficient g_{ij} can be expressed by use of the definition (2.2.11) and the dot product relation (2.2.14):

$$g_{\xi\omega} = \sum_{k,l=1}^{3} \frac{\partial q^k}{\partial \xi} \mathcal{G}_{kl} \frac{\partial q^l}{\partial \omega}. \tag{3.3.11}$$

Now again applying the chain rule, the variation can be evaluated via

$$\frac{dg_{\xi\omega}}{d\eta} = \sum_{k,l=1}^{3} \left[q^k_{\dot{\xi}} \mathcal{G}_{kl} \frac{dq^l_{\dot{\omega}}}{d\eta} + q^l_{\dot{\omega}} \mathcal{G}_{lk} \frac{dq^k_{\dot{\xi}}}{d\eta} + \sum_{a=1}^{3} \left(q^k_{\dot{\xi}} \frac{\partial \mathcal{G}_{kl}}{\partial q^a} q^l_{\dot{\omega}} \right) \frac{dq^a}{d\eta} \right]. \tag{3.3.12}$$

The only unknown quantities left in these equations are the variations of X^1, X^2, λ and the Jacobian $\mathcal{J}_h$. However, $\mathcal{J}_h = \sqrt{G}$ is analytically known by the choice of the mapping to physical space, for the cylindrical coordinates it is simply $\mathcal{J}_h = R$. Henceforth, one is left with the solution variables (X^1, X^2, λ) which will be calculated via a descretization, explicitly introducing the DOFs and allowing the minimisation of W. The minimisation procedure itself will be done via *gradient descent*.

3.4. Discretization of the Solution Variables

The question what form X^1, X^2 and λ take and how they depend on the DOFs remains. In GVEC all the solution variables are described using a tensor-product ansatz where the *radial* and the *angular* dependencies are separated. Mind, *radial* and *angular* refer in this case to the generalized concepts. In that sense, the ansatz can be expressed as

$$\begin{aligned} X^k &= X^{k,[rad.]}(s) X^{k,[ang.]}(\theta, \zeta) \\ \lambda &= \lambda^{[rad.]}(s) \lambda^{[ang.]}(\theta, \zeta). \end{aligned} \tag{3.4.1}$$

Since the angular coordinates are periodic, a description via a Fourier-Ansatz is suitable. Hence, the angular contributions are expressed in a Fourier-series with the basis functions

$$\begin{aligned} X^{k,[ang.]}_{base}(\theta, \zeta) &= \lambda^{[ang.]}_{base}(\theta, \zeta) \\ &= \mathcal{F}_{mn}(\theta, \zeta) = \cos(m\theta - N_{FP} n\zeta) \text{ and/or } \sin(m\theta - N_{FP} n\zeta). \end{aligned} \tag{3.4.2}$$

The quantity N_{FP} indicates the number of toroidal field periods. The labels m and n describe the mode numbers and thus will indicate the contributing modes. These modes are chosen such that

$$m \in [0, m_{max}] \quad n \in \begin{cases} [0, n_{max}], & m = 0 \\ [-n_{max}, n_{max}] & m \neq 0 \end{cases}. \tag{3.4.3}$$

The radial contribution is expressed via splines of a chosen degree p_x with maximum continuity $C^{(p_x-1)}$.

3.4.1. B-Splines

Given a set of control points $\mathbf{D}_0, \dots \mathbf{D}_n$ and a vector containing knots $\mathbf{T} = \{t_0, t_1, \dots, t_m\}$ with $t_i \in [0,1]$ it is possible to define a function $\mathbf{C}(t)$ via

$$\mathbf{C}(t) = \sum_{i=0}^{n} \mathbf{D}_i N_{i,p}(t), \tag{3.4.4}$$

where $p = m - n - 1$ is the definition of the degree and $N_{i,j}$ are the basis functions defined as [34]

$$\begin{aligned} N_{i,0} &= \begin{cases} 1 & \text{if } t_i \leq \ t < t_{i+1} \text{ and } t - i < t_{i+1} \\ 0 & \text{otherwise} \end{cases} \\ N_{i,j}(t) &= \frac{t - t_i}{t_{i+j} - t_i} N_{i,j-1}(t) + \frac{t_{i+j+1} - t}{t_{i+j+1} - t_{i+1}} N_{i+1,j-1}(t). \end{aligned} \tag{3.4.5}$$

Hence, $\mathbf{C}(t)$ is referred to as a B(asis)-spline function. These B-splines are used for the discretization of the *radial* direction in the tensor-product ansatz.

3.5. Alternative Descriptions of the Magnetic Field Topology

Motivated by promising results with regards to the calculation of resonant perturbations as shown in the the work by M.Taylor [2], alternative descriptions of the magnetic field topology shall be introduced in this section.

3.5.1. NSTAB-Mapping

The basic idea behind this mapping, which is equivalent to the one used in the NSTAB code by M.Taylor [2], is to express the, as of now, decoupled variables X^1 and X^2 via a linear coupling of the coordinate values at the *magnetic axis* (X_a^i) and the *fixed boundary* (X_b^i). This coupling is done via the introduction of a generalized radius α. However, α couples not only the central and outer most flux surface but also the two coordinates X^1 and X^2, for it is used for both representations. In that sense one obtains the mapping via[35]

$$\begin{aligned} X^1 &= X_a^1(\zeta) + \alpha(s,\theta,\zeta)\left[X_b^1(\theta,\zeta) - X_a^1(\zeta)\right] \\ X^2 &= X_a^2(\zeta) + \alpha(s,\theta,\zeta)\left[X_b^2(\theta,\zeta) - X_a^2(\zeta)\right], \end{aligned} \tag{3.5.1}$$

where $\alpha(0,\theta,\zeta) = 0$ and $\alpha(1,\theta,\zeta) = 1$ provide the necessary limits. It is worth noting, that the magnetic axis is independent of s and θ since it is a degenerate flux surface of volume zero.

In the original GVEC the variables X^1 and X^2 are expressed via a tensor product ansatz using Fourier- and spline basis functions. Therefore, the DOFs are defined by the corresponding coefficients to these basis functions. With the new mapping, the same basis functions are used to discretize the new solution variables X_a^1, X_a^2

[34] see E. Weisstein, B-Spline [3]

[35] In NSTAB [2] $X_a^1 \equiv r_0$, $X_a^2 \equiv z_0$, $X_b^1 \equiv r_1$, $X_b^2 \equiv z_1$ and $\alpha \equiv R$

and α. The treatment of the potential λ is left unchanged. Since GVEC works with a *fixed boundary*, X_b^1 and X_b^2 are just prescribed, although they too are expressed via a Fourier-basis. Consequently, one can write X_a^1, X_a^2 and α via

$$X_a^i(\zeta) = \sum_n \left\{X_a^i\right\}_n \mathcal{F}_n(\zeta) \tag{3.5.2}$$

$$X_b^i(\theta,\zeta) = X_b^{k,[ang.]}(\theta,\zeta) = \sum_{m,n} \left\{X_b^i\right\}_{mn} \mathcal{F}_{mn}(\theta,\zeta) \tag{3.5.3}$$

$$\alpha(s,\theta,\zeta) = \sum_{l,m,n} \{\alpha\}_{lmn} \mathcal{F}_{mn}(\theta,\zeta)\mathcal{B}_l(s). \tag{3.5.4}$$

Here, i denotes the coordinate, i.e. $i \in [1,2]$. $\mathcal{B}_l(s)$ symbolizes the l-th spline basis function and $\mathcal{F}_n(\zeta) \equiv \mathcal{F}_{m=0,n}(\zeta)$. The quantities in the curly brackets $\left(\{X_a^i\}_n, \{X_b^i\}_{mn}, \{\alpha\}_{lmn}\right)$ are the combined coefficients from the Fourier- and spline expansion, i.e. the DOFs.

As a result, important changes in the variation of the energy functional, i.e. the forces onto the DOFs, have to be made. In the original mapping the derivatives of X^1 and X^2 with respect to a DOF $(d/d\eta)$ are given by just one (combined) basis function. This is because, X^1 and X^2 are directly calculated via the tensor-product ansatz. The basis function obtained via this derivative would then be considered within the force calculation. With the new mapping, however, changes for the derivatives with respect to the flux coordinates (s,θ,ζ) and the basis coefficients have to be made. Especially important is the fact that now both X^1 and X^2 are affected by the variation in the α-coefficients.
Henceforth, calculating the derivatives with respect to the flux coordinates yields

$$X_{\dot{s}}^i = \alpha_{\dot{s}}(X_b^i - X_a^i) \tag{3.5.5}$$

$$X_{\dot{\zeta}}^i = X_{a,\dot{\zeta}}^i + \alpha_{\dot{\zeta}}(X_b^i - X_a^i) + \alpha(X_{b,\dot{\zeta}}^i - X_{a,\dot{\zeta}}^i) \tag{3.5.6}$$

$$X_{\dot{\theta}}^i = \alpha_{\dot{\theta}}(X_b^i - X_a^i) + \alpha X_{b,\dot{\theta}}^i. \tag{3.5.7}$$

Using these results, the necessary contributions to the force terms are obtained by varying with respect to the combined Fourier-spline coefficients:

For X_a^i

$$\frac{\partial X^i}{\partial \{X_a^i\}_n} = [1-\alpha]\,\mathcal{F}_n(\zeta) \tag{3.5.8}$$

$$\frac{\partial X_{\dot{s}}^i}{\partial \left\{X_a^i\right\}_n} = -\alpha_{\dot{s}}\mathcal{F}_n(\zeta) \tag{3.5.9}$$

$$\frac{\partial X_{\dot{\zeta}}^i}{\partial \left\{X_a^i\right\}_n} = [1-\alpha]\,\mathcal{F}_{n,\dot{\zeta}}(\zeta) - \alpha_{\dot{\zeta}}\mathcal{F}_n(\zeta) \tag{3.5.10}$$

$$\frac{\partial X^i_{\dot\theta}}{\partial \{X^i_a\}_n} = -\alpha_{\dot\theta}\mathcal{F}_n(\zeta) \tag{3.5.11}$$

and for α

$$\frac{\partial X^i}{\partial \{\alpha\}_{lmn}} = \left[X^i_b - X^i_a\right]\mathcal{F}_{mn}(\theta,\zeta)\mathcal{B}_l(s) \tag{3.5.12}$$

$$\frac{\partial X^i_{\dot s}}{\partial \{\alpha\}_{lmn}} = \left[X^i_b - X^i_a\right]\mathcal{F}_{mn}(\theta,\zeta)\mathcal{B}_{l,\dot s}(s) \tag{3.5.13}$$

$$\frac{\partial X^i_{\dot\zeta}}{\partial \{\alpha\}_{lmn}} = \left[X^i_{b,\dot\zeta} - X^i_{a,\dot\zeta}\right]\mathcal{F}_{mn}(\theta,\zeta)\mathcal{B}_l(s) + \left[X^i_b - X^i_a\right]\mathcal{F}_{mn,\dot\zeta}(\theta,\zeta)\mathcal{B}_l(s) \tag{3.5.14}$$

$$\frac{\partial X^i_{\dot\theta}}{\partial \{\alpha\}_{lmn}} = X^i_{b,\dot\theta}\mathcal{F}_{mn}(\theta,\zeta)\mathcal{B}_l(s) - \left[X^i_b - X^i_a\right]\mathcal{F}_{mn,\dot\theta}(\theta,\zeta)\mathcal{B}_l(s). \tag{3.5.15}$$

3.5.2. The Hybrid Mapping

Due to several problematic attributes of the NSTAB-mapping within the theoretical set-up of GVEC, which will be discussed in detail in chapter 4, an additional slightly altered version of the NSTAB-mapping was used:

$$\begin{aligned} X^1 &= \hat{X}^1_a(s,\theta,\zeta) + \alpha(s,\theta,\zeta)\left[X^1_b(\theta,\zeta) - \hat{X}^1_a(s,\theta,\zeta)\right] \\ X^2 &= \hat{X}^2_a(s,\theta,\zeta) + \alpha(s,\theta,\zeta)\left[X^2_b(\theta,\zeta) - \hat{X}^2_a(s,\theta,\zeta)\right]. \end{aligned} \tag{3.5.16}$$

The difference to (3.5.1) is given by the extended dependencies of X^i_a on (s,θ) denoted via the quantity $\hat{X}^i_a$:

$$\hat{X}^i_a(s,\theta,\zeta) = \sum_{l,m,n}\left\{\hat{X}^i_a\right\}_{lmn}\mathcal{F}_{mn}(\theta,\zeta)\mathcal{B}_l(s). \tag{3.5.17}$$

Again, $\mathcal{F}_{mn}$ and $\mathcal{B}_l$ are the corresponding basis functions and $\{\hat{X}^i_a\}_{lmn}$ is the combined coefficient.

This mapping effectively represents a hybridisation between the original GVEC- and the NSTAB-mapping. The dependency of $\hat{X}^i_a$ on θ, which is completely optional, is implemented in the code and could eventually allow for a stronger shift in the hybridisation towards the original GVEC mapping. However, for the analysis performed in this thesis, no use of this dependency was necessary. Furthermore, the test cases discussed in Sec.4 are all axisymmetric and thus, a ζ-dependency is not included. Therefore, only the $m = n = 0$ mode is used for $\hat{X}^i_a$, yielding $\hat{X}^i_a = \hat{X}^i_a(s)$. Thus, the difference between the NSTAB mapping and (3.5.16) is given by the additional s-dependency in $\hat{X}^i_a$. Whereas the NSTAB mapping blends the outer boundary to the magnetic axis, we have now a blending from the outer boundary to the centres of the individual flux surfaces. In that sense $\hat{X}^i_a(s)$ represents the positions of these centres and $\hat{X}^i_a(s=0)$ represents the actual magnetic axis.

Even though the basic representation is hardly changed, the introduction of the new dependencies heavily affects the derivatives of the mapping. The derivatives with respect to the new mapping variables are given by

$$X^i_{\dot{s}} = (1-\alpha)\,\hat{X}^i_{a,\dot{s}} + \alpha_{\dot{s}}(X^i_b - \hat{X}^i_a) \tag{3.5.18}$$

$$X^i_{\dot{\zeta}} = \hat{X}^i_{a,\dot{\zeta}} + \alpha_{\dot{\zeta}}(X^i_b - \hat{X}^i_a) + \alpha(X^i_{b,\dot{\zeta}} - \hat{X}^i_{a,\dot{\zeta}}) \tag{3.5.19}$$

$$X^i_{\dot{\theta}} = \hat{X}^i_{a,\dot{\theta}} + \alpha_{\dot{\theta}}(X^i_b - \hat{X}^i_a) + \alpha\left(X^i_{b,\dot{\theta}} - \hat{X}^i_{a,\dot{\theta}}\right). \tag{3.5.20}$$

In a similar fashion there are additional dependencies arising in the force terms:

For X^i_a

$$\frac{\partial X^i}{\partial\left\{\hat{X}^i_a\right\}_{lmn}} = [1-\alpha]\,\mathcal{F}_{mn}(\theta,\zeta)\mathcal{B}_l(s) \tag{3.5.21}$$

$$\frac{\partial X^i_{\dot{s}}}{\partial\left\{\hat{X}^i_a\right\}_{lmn}} = [1-\alpha]\,\mathcal{F}_{mn}(\theta,\zeta)\mathcal{B}'_l(s) - \alpha_{\dot{s}}\mathcal{F}_{mn}(\theta,\zeta)\mathcal{B}_l(s) \tag{3.5.22}$$

$$\frac{\partial X^i_{\dot{\zeta}}}{\partial\left\{\hat{X}^i_a\right\}_{lmn}} = [1-\alpha]\,\mathcal{F}_{mn,\dot{\zeta}}(\zeta)\mathcal{B}_l(s) - \alpha_{\dot{\zeta}}\mathcal{F}_{mn}(\zeta)\mathcal{B}_l(s) \tag{3.5.23}$$

$$\frac{\partial X^i_{\dot{\theta}}}{\partial\left\{\hat{X}^i_a\right\}_{lmn}} = [1-\alpha]\,\mathcal{F}_{mn,\dot{\theta}}(\theta,\zeta)\mathcal{B}_l(s) - \alpha_{\dot{\theta}}\mathcal{F}_{mn}(\theta,\zeta)\mathcal{B}_l(s) \tag{3.5.24}$$

and for α

$$\frac{\partial X^i}{\partial\{\alpha\}_{lmn}} = \left[X^i_b - \hat{X}^i_a\right]\mathcal{F}_{mn}(\theta,\zeta)\mathcal{B}_l(s) \tag{3.5.25}$$

$$\frac{\partial X^i_{\dot{s}}}{\partial\{\alpha\}_{lmn}} = \left[X^i_b - \hat{X}^i_a\right]\mathcal{F}_{mn}(\theta,\zeta)\mathcal{B}_{l,\dot{s}}(s) - X^i_{a,\dot{s}}\mathcal{F}_{mn}(\theta,\zeta)\mathcal{B}_l(s) \tag{3.5.26}$$

$$\frac{\partial X^i_{\dot{\zeta}}}{\partial\{\alpha\}_{lmn}} = \left[X^i_{b,\dot{\zeta}} - \hat{X}^i_{a,\dot{\zeta}}\right]\mathcal{F}_{mn}(\theta,\zeta)\mathcal{B}_l(s) + \left[X^i_b - \hat{X}^i_a\right]\mathcal{F}_{mn,\dot{\zeta}}(\theta,\zeta)\mathcal{B}_l(s) \tag{3.5.27}$$

$$\frac{\partial X^i_{\dot{\theta}}}{\partial\{\alpha\}_{lmn}} = \left[X^i_{b,\dot{\theta}} - \hat{X}^i_{a,\dot{\theta}}\right]\mathcal{F}_{mn}(\theta,\zeta)\mathcal{B}_l(s) - \left[X^i_b - \hat{X}^i_a\right]\mathcal{F}_{mn,\dot{\theta}}(\theta,\zeta)\mathcal{B}_l(s). \tag{3.5.28}$$

3.6. Code Structure

In Fig.10 a rough schematic of the basic code structure for GVEC is shown. For a calculation the physical-, minimization- and visualization-parameters have to be specified at the start via a parameter file that will be read into the code. Afterwards, the initial configuration of the system is calculated from these parameters. As described before, splines and Fourier-basis functions are used for the discretization.

Three main choices for the initialization can be made. Either the boundary configuration and the magnetic axis position, given in the parameter file, are used to calculate a starting configuration or a configuration from a previous calculation is read into the code (restart). Additionally, GVEC can use VMEC data files as an input. For the original mapping this allows a restart from a VMEC calculation. Due to the different representations in the NSTAB- and hybrid mapping, only the boundary and axis parameters from VMEC can be used there. In general, it is worth noting that the initial configurations for the NSTAB and hybrid mapping are obtained via a similar blending as in their underlying representation. As a result all initial flux surfaces are scaled versions of the boundary flux surface, thus having the same shape. In the original GVEC-mapping, however, an elliptical form of the inner flux surfaces can be easily initialised.

The minimizing process itself relies on three main routines, the energy- and force-variation/evaluation and the preconditioning scheme. Preconditioning is a useful procedure to speed up convergence. For GVEC a preconditioning scheme similar to the one presented by S.P.Hirshman and O.Bentancourt in [8] is used.

Finally, GVEC produces output files that can be used to visualize physical and numerical quantities of interest. Furthermore, data files containing the information for a restart are produced.

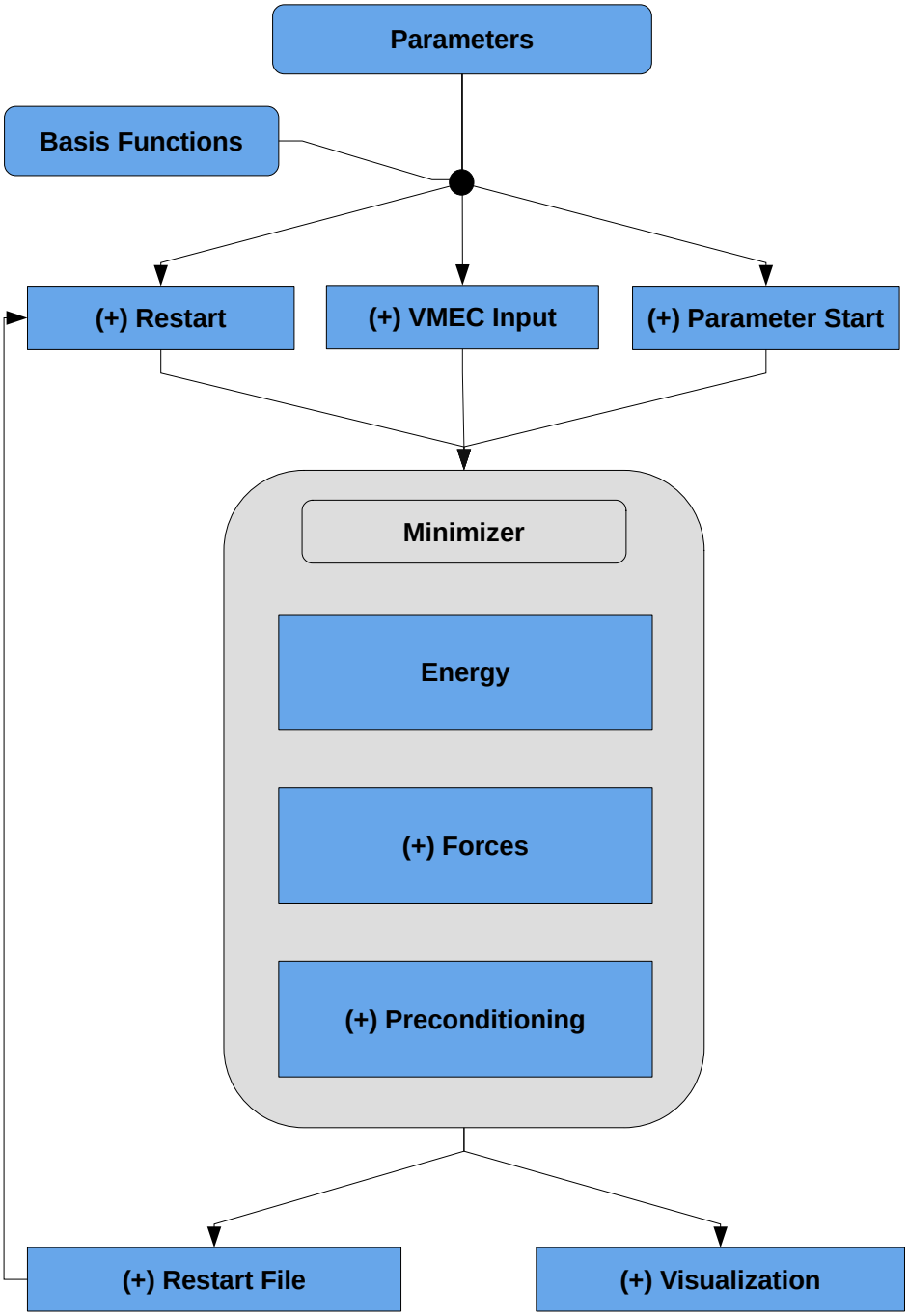

Figure 10: Schematic code structure of GVEC. The blocks marked by (+) had to be adapted for the alternative mappings.

3.6.1. Adaptations in the Preconditioner

For the hybrid mapping, which includes the s-dependent quantity $\hat{X}_a^i(s,\zeta)$, an adaptation of the preconditioning scheme as used in the original GVEC mapping is possible. The basic idea is to calculate the highest derivatives of the Hessian-matrix, which are the derivatives of the force terms, collect them and average over the two

angles (θ, ζ). This results in a 1D radial preconditioner for each Fourier-mode. A detailed derivation of this preconditioner may be found in [6] and [8].

For the hybrid mapping, alterations in the preconditioning matrix for the forces on X^1 and X^2 had to be made, so that the new preconditioner deals with the forces on $\hat{X}_a^1, \hat{X}_a^2$ and α.

The radial preconditioner matrix for the force onto X^i is given by

$$K_{kl}^{X^i} = |\sigma^{mn}| \int_0^1 \left\{ \frac{\partial X_{\dot{s}}^{i,[rad.]}(s)}{\partial \eta_k} D_{ss}^{X^i}(s) \frac{\partial X_{\dot{s}}^{i,[rad.]}(s)}{\partial \eta_l} + \frac{\partial X^{i,[rad.]}(s)}{\partial \eta_k} \left(\mathcal{S}^{X^i}(s) + \left[m^2 D_{\theta\theta}^{X^i}(s) + mn D_{\theta\zeta}^{X^i}(s) + n^2 D_{\zeta\zeta}^{X^i} \right] \right) \frac{\partial X^{i,[rad.]}(s)}{\partial \eta_l} \right\} ds. \tag{3.6.1}$$

Where the index $i \in [1,2]$ denotes the coordinate and the indices k, l indicate the matrix element. The quantity $|\sigma^{mn}|$ acts as the norm for the Fourier-mode-(mn). The quantities denoted by $D_{ab}^{X^i}$, with $a, b \in [s, \theta, \zeta]$, are diffusion coefficients:

$$D_{ss}^{X^1}(s) = \left\langle \mathfrak{D}_{ss}^{X^1} \right\rangle_{(\theta,\zeta)} = \left\langle \frac{b^\xi g_{\xi\omega} b^\omega}{\mathcal{J}^2} \frac{1}{\mathcal{J}} \left(\mathcal{J}_h X_{\dot{\theta}}^2 \right)^2 \right\rangle_{(\theta,\zeta)} \tag{3.6.2}$$

$$\mathcal{S}^{X^1}(s) = \left\langle \mathfrak{S}^{X^1} \right\rangle_{(\theta,\zeta)} = \left\langle \frac{b^\xi g_{\xi\omega} b^\omega}{\mathcal{J}^2} \frac{1}{\mathcal{J}} \left(\mathcal{J}_p \frac{\partial \mathcal{J}}{\partial q^1} \right)^2 \right\rangle_{(\theta,\zeta)} \tag{3.6.3}$$

$$D_{\theta\theta}^{X^1}(s) = \left\langle \mathfrak{D}_{\theta\theta}^{X^1} \right\rangle_{(\theta,\zeta)} = \left\langle \frac{b^\xi g_{\xi\omega} b^\omega}{\mathcal{J}^2} \frac{1}{\mathcal{J}} \left(\mathcal{J}_h X_{\dot{s}}^2 \right)^2 + \frac{\mathcal{J}_h b^\theta}{\mathcal{J}^2} \left(2 X_{\dot{s}}^2 \left(b^\theta q_{\dot{\theta}}^i + b^\zeta q_{\dot{\zeta}}^i \right) \mathcal{G}_{i1} + \mathcal{J}_p b^\theta \mathcal{G}_{11} \right) \right\rangle_{(\theta,\zeta)} \tag{3.6.4}$$

$$D_{\theta\zeta}^{X^1}(s) = \left\langle \mathfrak{D}_{\theta\zeta}^{X^1} \right\rangle_{(\theta,\zeta)} = \left\langle \frac{\mathcal{J}_h b^\theta}{\mathcal{J}^2} \left(2 X_{\dot{s}}^2 \left(b^\theta q_{\dot{s}}^i + b^\zeta q_{\dot{\zeta}}^i \right) \mathcal{G}_{i1} + \mathcal{J}_p b^\theta \mathcal{G}_{11} \right) \right\rangle_{(\theta,\zeta)} \tag{3.6.5}$$

$$D_{\zeta\zeta}^{X^1} = \left\langle \mathfrak{D}_{\zeta\zeta}^{X^1} \right\rangle_{(\theta,\zeta)} = \left\langle \frac{1}{\mathcal{J}} b^\zeta b^\zeta \mathcal{G}_{11} \right\rangle_{(\theta,\zeta)} \tag{3.6.6}$$

$$D_{ss}^{X^2}(s) = \left\langle \mathfrak{D}_{ss}^{X^2} \right\rangle_{(\theta,\zeta)} = \left\langle \frac{b^\xi g_{\xi\omega} b^\omega}{\mathcal{J}^2} \frac{1}{\mathcal{J}} \left(\mathcal{J}_h X_{\dot{\theta}}^1 \right)^2 \right\rangle_{(\theta,\zeta)} \tag{3.6.7}$$

$$\mathcal{S}^{X^2}(s) = \left\langle \mathfrak{S}^{X^2} \right\rangle_{(\theta,\zeta)} = \left\langle \frac{b^\xi g_{\xi\omega} b^\omega}{\mathcal{J}^2} \frac{1}{\mathcal{J}} \left(\mathcal{J}_p \frac{\partial \mathcal{J}}{\partial q^2} \right)^2 \right\rangle_{(\theta,\zeta)} \tag{3.6.8}$$

$$D_{\theta\theta}^{X^2}(s) = \left\langle \mathfrak{D}_{\theta\theta}^{X^2} \right\rangle_{(\theta,\zeta)} = \left\langle \frac{b^\xi g_{\xi\omega} b^\omega}{\mathcal{J}^2} \frac{1}{\mathcal{J}} \left(\mathcal{J}_h X_{\dot{s}}^1 \right)^2 + \frac{\mathcal{J}_h b^\theta}{\mathcal{J}^2} \left(2 X_{\dot{s}}^1 \left(b^\theta q_{\dot{\theta}}^i + b^\zeta q_{\dot{\zeta}}^i \right) \mathcal{G}_{i2} + \mathcal{J}_p b^\theta \mathcal{G}_{22} \right) \right\rangle_{(\theta,\zeta)} \tag{3.6.9}$$

$$D_{\theta\zeta}^{X^2}(s) = \left\langle \mathfrak{D}_{\theta\zeta}^{X^2} \right\rangle_{(\theta,\zeta)} = \left\langle \frac{\mathcal{J}_h b^\theta}{\mathcal{J}^2} \left(2X_{\dot{s}}^1 \left(b^\theta q_\theta^i + b^\zeta q_\zeta^i \right) \mathcal{G}_{i2} + \mathcal{J}_p b^\theta \mathcal{G}_{22} \right) \right\rangle_{(\theta,\zeta)} \tag{3.6.10}$$

$$D_{\zeta\zeta}^{X^2} = \left\langle \mathfrak{D}_{\zeta\zeta}^{X^2} \right\rangle_{(\theta,\zeta)} = \left\langle \frac{1}{\mathcal{J}} b^\zeta b^\zeta \mathcal{G}_{22} \right\rangle_{(\theta,\zeta)}. \tag{3.6.11}$$

The brackets $\langle \cdots \rangle_{(\theta,\zeta)}$ symbolise the average over the angles (θ, ζ). The quantities in fraktur-font (e.g., $\mathfrak{D}$) denote the coefficients before the averaging is performed.

Similar to the adaptations necessary for the forces, the evaluation of the derivatives of X^i with respect to the basis coefficients η are the ones that have to be treated differently for the hybrid mapping. The changes in the $\mathfrak{D}$-coefficients and $\mathfrak{S}$ are already handled by the force evaluation routine. However, the quantities $\frac{\partial}{\partial \eta_k} X^{i,[rad.]}$ and $\frac{\partial}{\partial \eta_k} X_{\dot{s}}^{i,[rad.]}$ introduce new dependencies that have to be multiplied onto the other coefficients. Where in the original mapping these quantities provide a selected radial basis functions, the hybrid mapping introduces additional factors due to the blending function. With that in mind, one can write the preconditioner matrices for the forces onto the hybrid solution variables $\hat{X}_a^i(s,\zeta)$ as

$$\begin{aligned} K_{kl}^{\hat{X}_a^i} = |\sigma^{mn}| \int_0^1 \Bigg\langle & \left([1-\alpha]\, \mathcal{B}_k'(s) - \alpha_{\dot{s}} \mathcal{B}_k(s) \right) \mathfrak{D}_{ss}^{X^i} \left([1-\alpha]\, \mathcal{B}_l'(s) - \alpha_{\dot{s}} \mathcal{B}_l(s) \right) \\ & + [1-\alpha]^2\, \mathcal{B}_k(s) \left(\mathfrak{S}^{X^i} + \left[m^2 \mathfrak{D}_{\theta\theta}^{X^i} + mn \mathfrak{D}_{\theta\zeta}^{X^i} + n^2 \mathfrak{D}_{\zeta\zeta}^{X^i} \right] \right) \mathcal{B}_l(s) \Bigg\rangle_{(\theta,\zeta)} ds. \end{aligned} \tag{3.6.12}$$

Where the index $i \in [1,2]$ denotes the coordinate and the indices k, l indicate the matrix element. $\mathcal{B}$ is again the corresponding selected B-spline function. In contrast to the original mapping, the preconditioner matrix includes mixed products of the basis function $\mathcal{B}$ and its derivative $\mathcal{B}'$.

For the preconditioning of the forces onto α, the coupling between X^1 and X^2 has to be considered again, resulting in the combined preconditioner matrix

$$\begin{aligned} K_{kl}^{\alpha} = |\sigma^{mn}| \int_0^1 \Bigg\langle & \left(\left[X_b^1 - \hat{X}_a^1 \right] \mathcal{B}_k'(s) - \hat{X}_{a,\dot{s}}^1 \mathcal{B}_k \right) \mathfrak{D}_{ss}^{X^1} \left(\left[X_b^1 - \hat{X}_a^1 \right] \mathcal{B}_l'(s) - \hat{X}_{a,\dot{s}}^1 \mathcal{B}_l \right) \\ & + \left(\left[X_b^2 - \hat{X}_a^2 \right] \mathcal{B}_k'(s) - \hat{X}_{a,\dot{s}}^2 \mathcal{B}_k \right) \mathfrak{D}_{ss}^{X^2} \left(\left[X_b^2 - \hat{X}_a^2 \right] \mathcal{B}_l'(s) - \hat{X}_{a,\dot{s}}^2 \mathcal{B}_l \right) \\ & + \left[X_b^1 - \hat{X}_a^1 \right]^2 \mathcal{B}_k(s) \left(\mathfrak{S}^{X^1} + \left[m^2 \mathfrak{D}_{\theta\theta}^{X^1} + mn \mathfrak{D}_{\theta\zeta}^{X^1} + n^2 \mathfrak{D}_{\zeta\zeta}^{X^1} \right] \right) \mathcal{B}_l(s) \\ & + \left[X_b^2 - \hat{X}_a^2 \right]^2 \mathcal{B}_k(s) \left(\mathfrak{S}^{X^2} + \left[m^2 \mathfrak{D}_{\theta\theta}^{X^2} + mn \mathfrak{D}_{\theta\zeta}^{X^2} + n^2 \mathfrak{D}_{\zeta\zeta}^{X^2} \right] \right) \mathcal{B}_l(s) \Bigg\rangle_{(\theta,\zeta)} ds. \end{aligned} \tag{3.6.13}$$

4. Numerical Results

In this chapter numerical results for different test cases and minimization parameters are presented and discussed. Thereby, the focus lies on the differences between the three mappings of the magnetic field topology.

4.1. Test Cases

This section presents a compact overview of the three test cases considered for the analysis of the different mappings for the magnetic field topology. An overview of the application of the individual cases can be found in tab.1. All the ζ = *const.* surfaces shown in this section represent results obtained using the hybrid mapping with the optimized minimisation configuration discussed later on in this chapter. Since all cases are axisymmetric, only the n=0 component is simulated and no discussion of the ζ dependency nor the use of additional Fourier modes in toroidal direction will be given.

Tab. 1: Overview Test Cases

Name	Initialisation	Investigated Issues	Section	Mappings
elliptic tokamak	equilibrium axis arbitrary axis	magnetic axis radial resolution	4.2 4.4	original, NSTAB, hybrid
TOKSY	VMEC-input	X_a^i boundary condition near axis asymptotic	4.3.2 4.3.1	original, hybrid
TOKX	arbitrary axis	X_a^i boundary condition	4.3.2	original, hybrid

4.1.1. Elliptic Tokamak

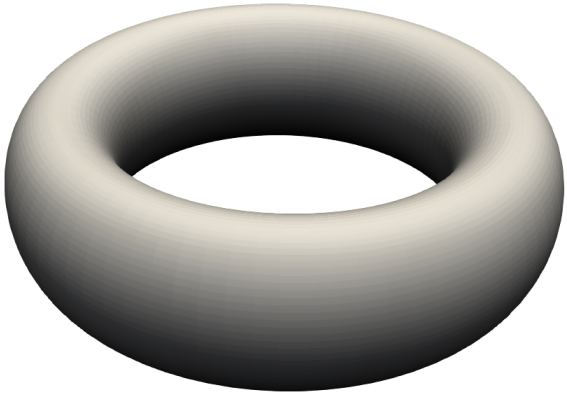

Figure 11: elliptic tokamak 3D outer boundary

The elliptic tokamak is the simplest test case used in this thesis. As the name suggests the outer boundary is given by an elliptic doughnut form (comp.Fig.11). Due to its highly symmetric form, the innermost up to the outermost flux surfaces are all described by an elliptical form. Although this test case is rather far from realistic geometries, it still provides insight into parameter-influences onto the minimization

process. Due to its simplicity, accurate results for the equilibrium configuration are expected. In Fig.12 the necessary physical quantities describing the test case are plotted. Note, that quantities linear in the normalized toroidal flux will show a quadratic dependency in s ($\Phi \sim s^2$).

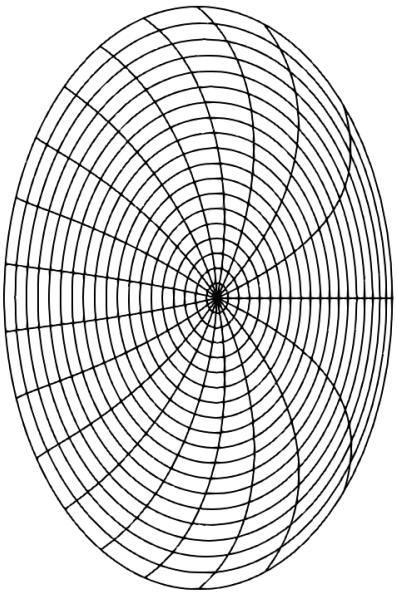

(a) ζ = *const.* plane

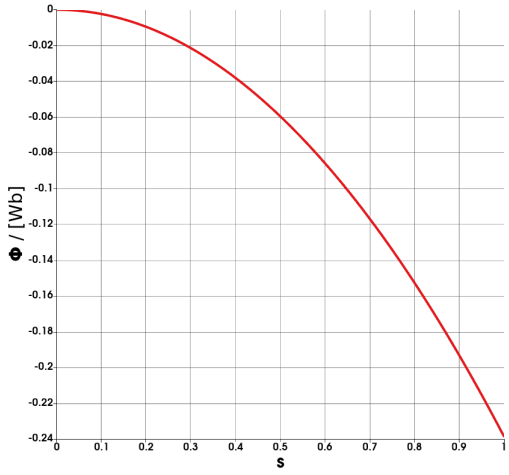

(b) toroidal flux

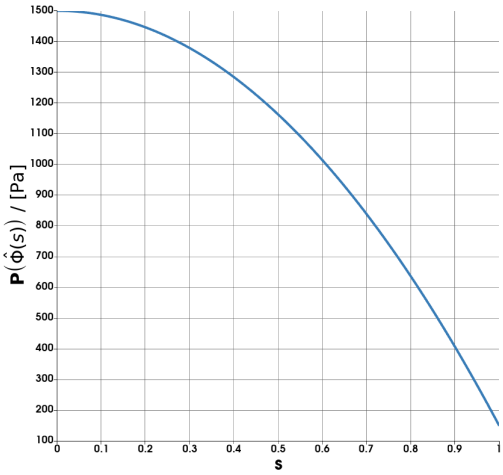

(c) pressure-profile

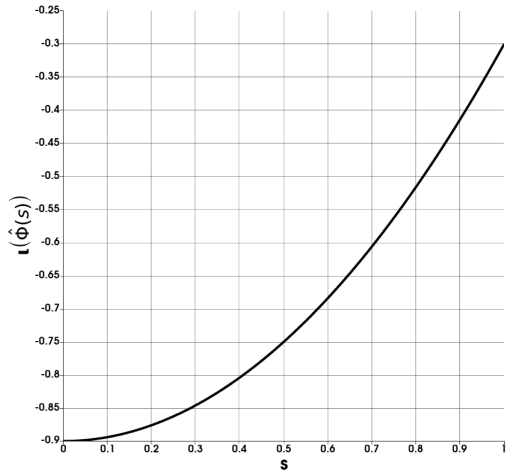

(d) iota-profile

Figure 12: Physical quantities prescribed for the elliptic tokamak test-case. In (a) one can see the circular s = *const.* flux surface contours and the θ^* = *const.* straight field line angle contours for a ζ = *const.* surface. In (b) the profile of the toroidal flux Φ is plotted. In (c) and (d) the corresponding pressure $\mathbf{P}$ and iota ι profiles in dependence of the flux surface label s are shown.

4.1.2. D-Shaped Tokamak: TOKSY

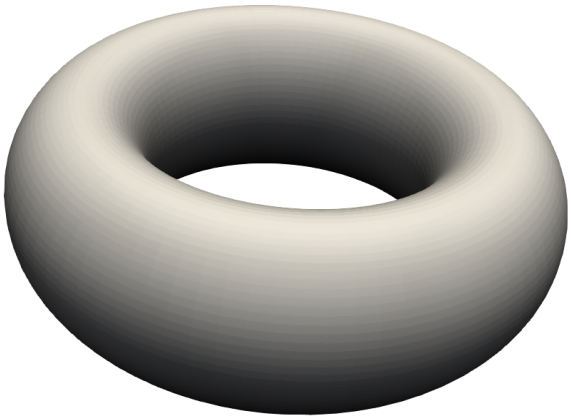

Figure 13: TOKSY 3D outer boundary

The D-shaped tokamak case provides an intermediate complexity for testing the influence of different minimization parameters. The outermost boundary already differs from the innermost flux surfaces which again takes the form of a simple ellipse. For mappings of the magnetic field topology that rely on the blending between the outer and inner flux surfaces, like the NSTAB- and hybrid mapping, such behaviour is of particular interest.

Furthermore, the input for this test case is provided by VMEC-data. The rotational transform ι- and pressure-profiles are rather complex and described by high-order polynomials. A visualization of this setup is give in Fig.14.

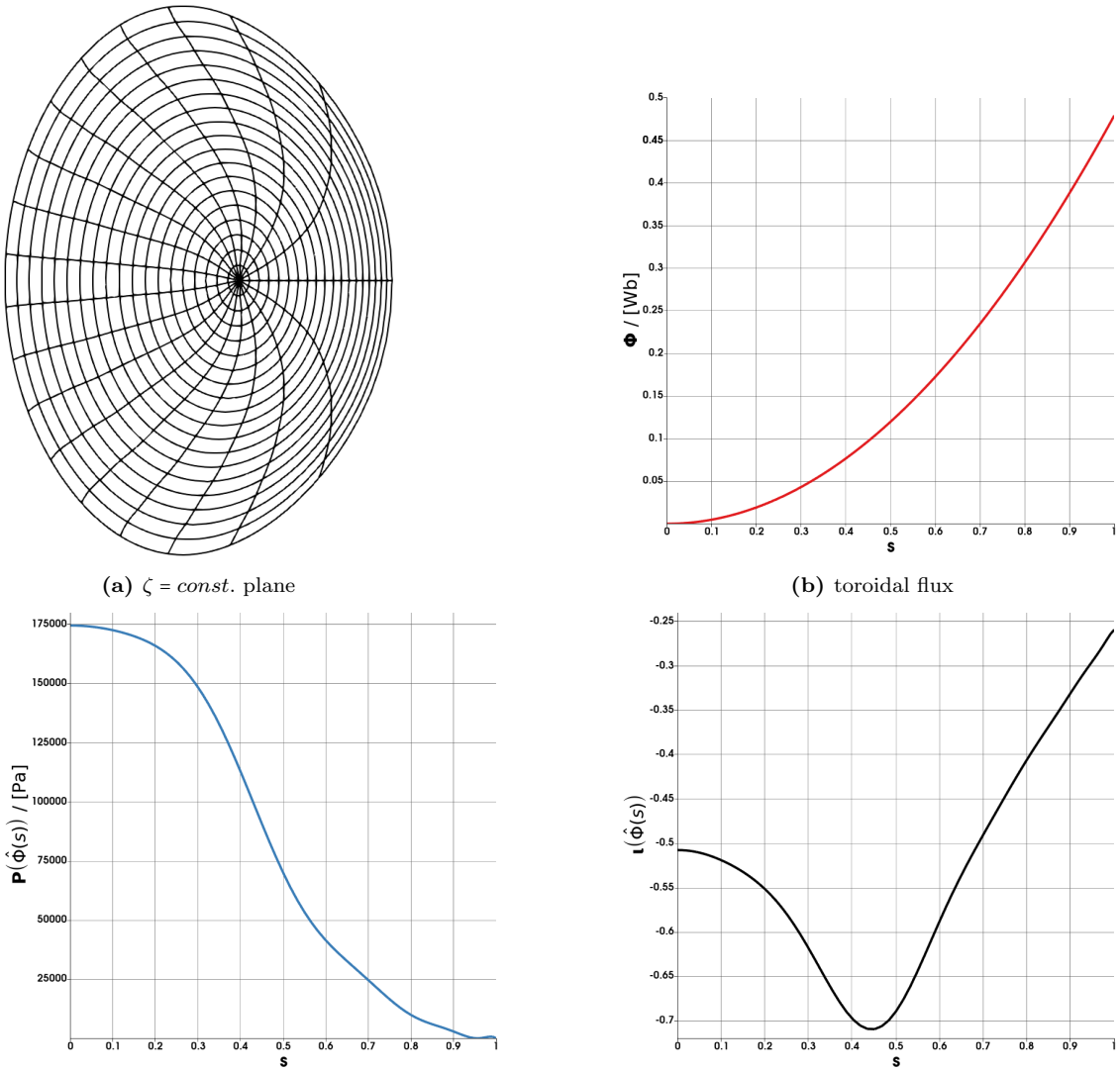

(a) $\zeta = const.$ plane

(b) toroidal flux

(c) pressure-profile

(d) iota-profile

Figure 14: Physical quantities prescribed for the TOKSY test-case. In (a) one can see the circular $s = const.$ flux surface contours and the $\theta^* = const.$ straight field line angle contours for a $\zeta = const.$ surface. In (b) the profile of the toroidal flux Φ is plotted. In (c) and (d) the corresponding pressure $\mathbf{P}$ and iota ι profiles in dependence of the flux surface label s are shown.

4.1.3. Tokamak with a Complex Boundary: TOKX

Figure 15: TOKX 3D outer boundary

The TOKX-tokamak provides a rather complex test case, for its outer boundary has to be parametrized by a high number of poloidal modes which are necessary to describe a flux surface that is close to an X-point. This causes a significant change of the form of the flux surfaces from the outer boundary towards the magnetic axis. Again, for mappings like the NSTAB and hybrid one, which include the blending function, this is of particular interest.

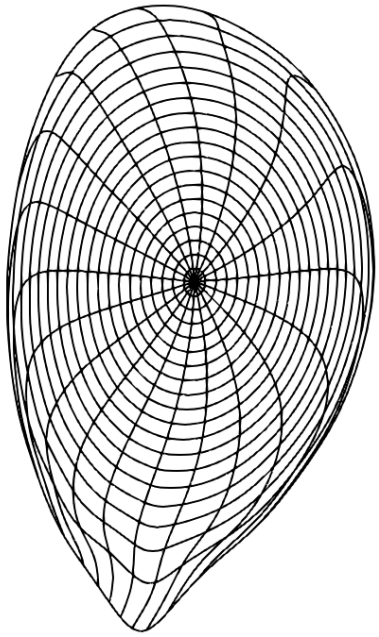

(a) $\zeta = const.$ plane

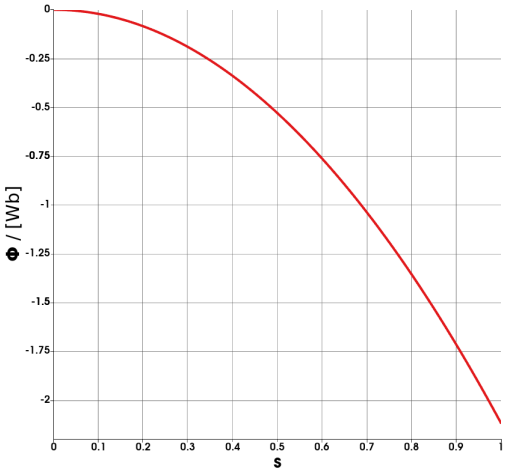

(b) toroidal flux

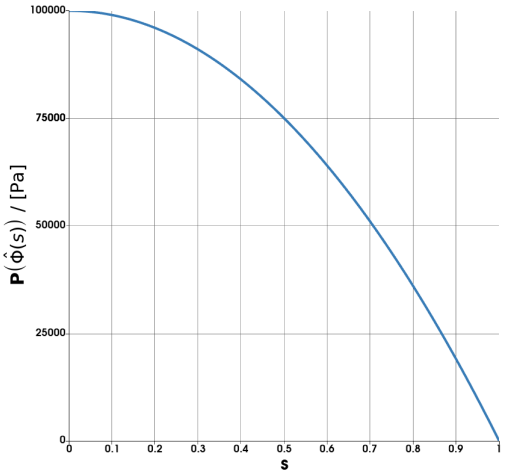

(c) pressure-profile

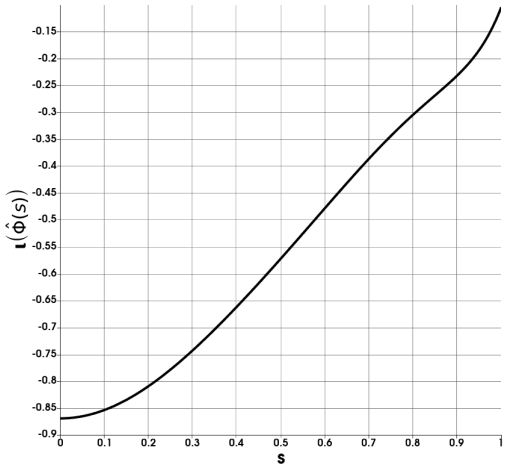

(d) iota-profile

Figure 16: Physical quantities prescribed for the TOKX test-case. In (a) one can see the circular $s = const.$ flux surface contours and the $\theta^* = const.$ straight field line angle contours for a $\zeta = const.$ surface. In (b) the profile of the toroidal flux Φ is plotted. In (c) and (d) the corresponding pressure $\mathbf{P}$ and iota ι profiles in dependence of the flux surface label s are shown.

4.2. Treatment of the Magnetic Axis

As mentioned before, the magnetic axis is the centre of the nested flux surfaces. It is a surface of degenerate volume zero and thus one has to deal with the arising singularity at $s = 0$ when using a polar coordinate system. [36]

Implementation of the mapping as used in the NTSAB code [37] into GVEC proved rather problematic with respect to the representation and positioning of the magnetic axis. This was already observed for the simple test case of the elliptic tokamak. A comparison between the original GVEC mapping (OM) and the alternative mapping as used within the NSTAB code [38] (NM) showed that the position of the magnetic axis was always delayed for the NM with respect to the OM for toroidal configurations. It appears that the forces onto the axis are dominated by non-local contributions from outer flux surfaces which prevents proper convergence (see Fig.18 and Fig.17). This non-local influences are especially evident, when the magnetic axis is initialised at the converged position, obtained from previous calculations. For the OM this initialisation results in a rapid convergence of the total energy and thus an equilibrium configuration. In the NM, however, the non-local force contributions onto X_a^i result in an initial shift of the axis which then is reversed during further iterations. This shift prevents a convergence of the NM within reasonable calculation times (see Fig.20). The reason for this behaviour might be found in the boundary condition for the magnetic axis. As discussed by Hirshman and Whitson [10], it is required that the radial variation of the (m=0,n)-mode of the X^i-coordinate must vanish at the axis when the flux label is proportional to the volume of the flux surface [39]:

$$\lim_{s\to 0}\left(\frac{\partial X^{i,0n}}{\partial s}(s,\theta,\zeta)\right) = 0. \tag{4.2.1}$$

This requirement is problematic since in the NM the radial derivative of X^i is dominated by the variation of the parameter α. The weight of $(X_b^i - X_a^i)$ in general is non-zero and the slope of α in the radial direction has to be non-zero as well for it linearly increases from 0 to 1 in the radial direction. In the NSTAB code this problem is circumvented by introducing an axis residue condition.[40] This condition treats the variation of the energy with respect to the DOFs of the axis by partial integration in s and θ. Extracting the singularity contribution in a residual term, which treats the volume $s = 0$ up to a close flux surface at $s_0 > s = 0$, allows for proper treatment of the outer regions and the calculation of the near axis region by imposing several simplifications onto the residual contribution. For the implementation into GVEC, this approach is unfit. Therefore, a slightly altered version of the NM is introduced, the previously discussed hybrid mapping (HM). To recapitulate, the basic idea is to introduce a radial dependency in the X_a^i parameter. As a result, the actual magnetic axis is given by the $\hat{X}_a^i(s = 0)$ contribution and the radial blending between edge and axis is now a blending between the edge and fictitious centres of the individual

[36] see Hirshman and Whitson Phys.Fluids 1983, 3557f [10] and Taylor Comp.Phys. 1994, 410 [2]
[37] see Taylor Comp.Phys. 1994 [2]
[38] see Taylor Comp.Phys. 1994, 409 [2]
[39] see Hirshman and Whitson Phys.Fluids 1983, 3558 [10]
[40] see Taylor Comp.Phys. 1994, 410f [2]

flux surfaces. This maintains the coupling of the X^1 and X^2 coordinates as well as the coupling of the edge to the central region, but also allows the fulfilment of the asymptotic behaviour (4.2.1).

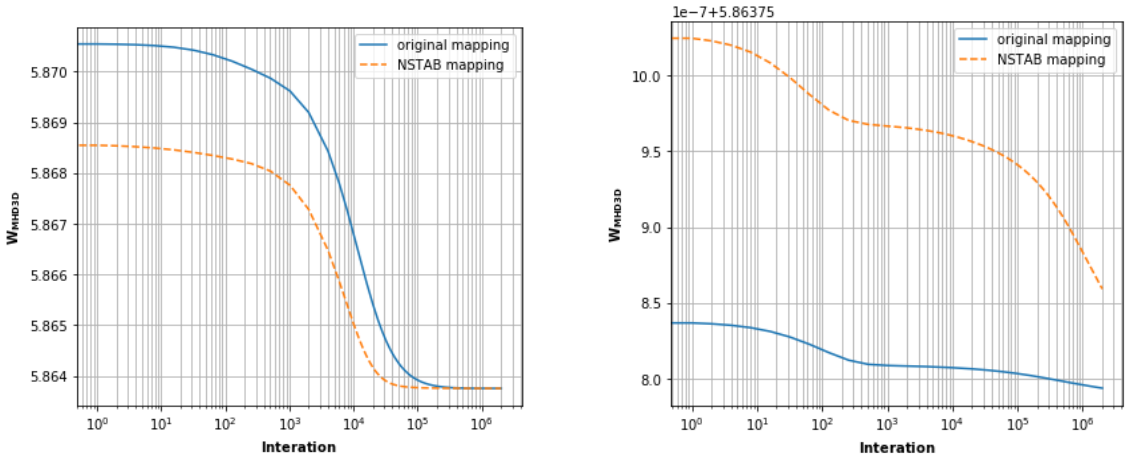

(a) initial $2 \cdot 10^6$ iterations

(b) restart with refined grid

Figure 17: Total energy W_{MHD3D} for the configuration of the elliptic tokamak. The initial position for the magnetic axis was displaced in X^1 and X^2. The continuous blue lines show the energy for the OM, the dashed orange lines the energy for the NM. In (**a**) the energy evolution is shown for the initial 2 million iterations. In (**b**) the energy evolution is shown after the calculation was restarted with a refined radial grid from a previous calculation were 4 million iterations were performed.

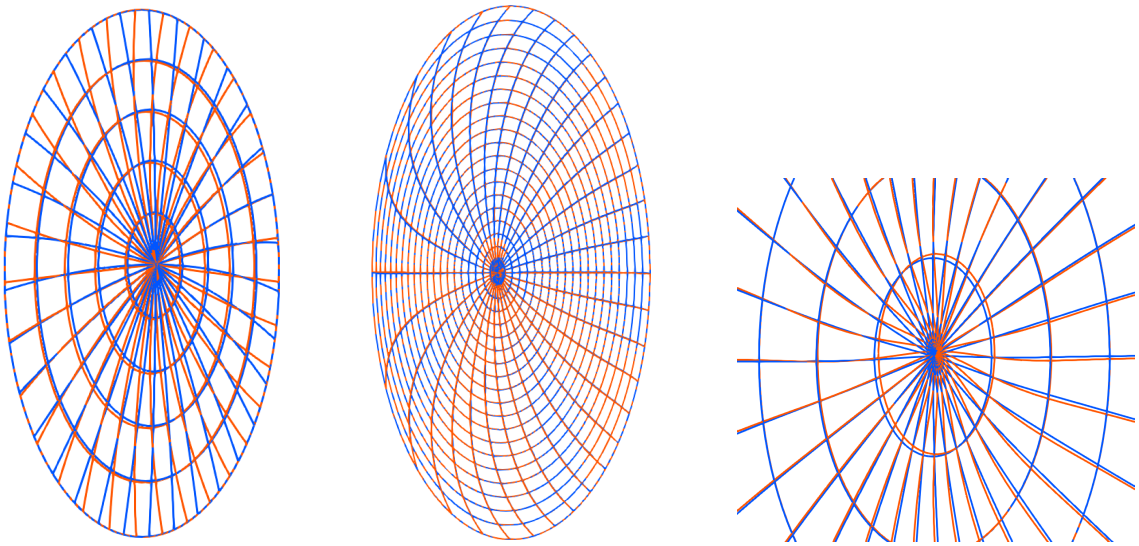

(a) initial configuration

(b) configuration after $6 \cdot 10^6$ iterations

(c) near-axis configuration after $6 \cdot 10^6$ iterations

Figure 18: A $\zeta = const.$ plane for the elliptic tokamak. The circular lines represent $s = const.$ surfaces the others represent $\theta = const.$ surfaces. The orange grid shows the configuration as calculated with the NM. The blue grid shows the OM solution. A total of 6 million iterations were performed for both variants of the mapping. The initial position of the magnetic axis was displaced in both relevant coordinates (X^1, X^2). Although, the overall configuration as shown in (**b**) is almost identical for both calculations, the near-axis region in (**c**) exhibits discrepancies between the two solutions.

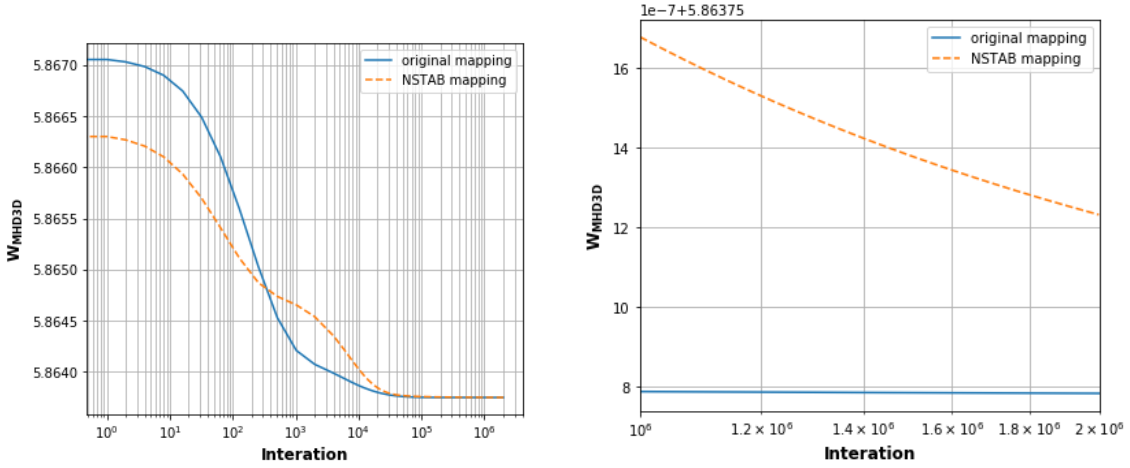

(a) initial $2 \cdot 10^6$ iterations

(b) grid refined $2 \cdot 10^6$ iterations

Figure 19: Total energy W_{MHD3D} for the configuration of the elliptic tokamak. The initial position for the magnetic axis is set to a previously calculated converged position. The continuous blue line shows the energy for the OM. The dashed orange line the energy for the NM. In (**a**) the energy evolution is shown for the total 2 million iterations. In (**b**) the final iteration steps are shown to demonstrate the difference in energy due to the different axis positions. Again, the energy of the NM is higher.

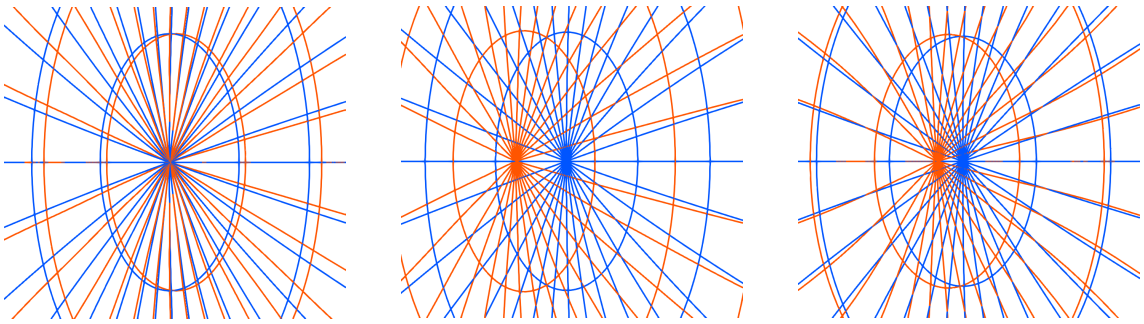

(a) initial configuration

(b) $5 \cdot 10^4$ iterations

(c) $2 \cdot 10^6$ iterations

Figure 20: A $\zeta = const.$ plane for the elliptic tokamak. The circular lines represent $s = const.$ surfaces the others represent $\theta = const.$ surfaces. The orange grid shows the configuration as calculated with the NM. The blue grid shows the OM solution. A total of 2 million iterations were performed for both variants of the mapping. The magnetic axis was initialised at a previously calculated converged position. It can be seen, that for the NM the axis is initially pulled away from the equilibrium position and then approaches it again with further iterations.

4.2.1. Improvements with the Hybrid Mapping

To validate the additionally introduced dependencies in the hybrid representation, the elliptic tokamak configuration as in Sec.4.2 was used for testing the minimisation process. Especially the initialisation at the equilibrated position of the magnetic axis is of interest. Again, a high number of iterations was performed to see whether or not the axis and total energy converges onto the same position/value as in the OM. Although, preconditioning with the previously described approach is possible for the HM it was not used in these calculations for the sake of comparability to the NM. Furthermore, for all calculations with the HM, $\hat{X}_a^i$ just includes the $m = n = 0$

mode. The energy evolution with respect to the number of iterations can be found in Fig.21. There, a comparison between the three different version for the mapping of the magnetic field topology can be seen. The quite different energy evolutions can be explained with the different initial configurations. Although, every calculation run was initialised with the same axis position and outer boundary, the overall initialisation had to be different due to the different approaches for the mapping. However, as can be observed, the final total energy of the hybrid mapping and the the *OM* are in good agreement.

Similarly, it is observable that the magnetic axis now stays at the initialised equilibrium position. In Fig.22 the corresponding visualisation results for the near-axis region are shown for different iteration steps. Again, a good agreement between the *OM* and the *HM* is present.

Due to this improvements and the complication to achieve satisfying equilibrium configurations with the *NM* within GVEC, all further calculations and analysis are performed with the *HM*.

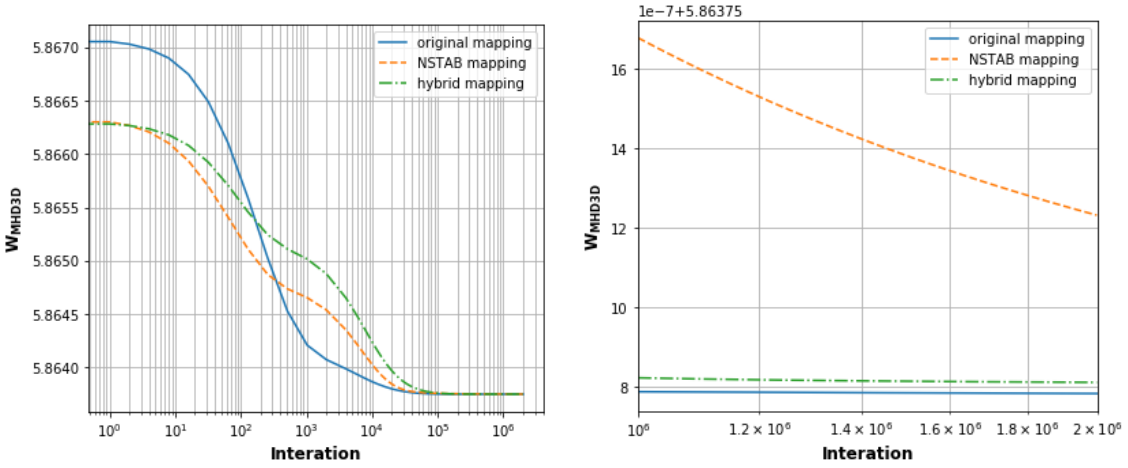

(a) total $2 \cdot 10^6$ iterations **(b)** final iterations

Figure 21: Total energy W_{MHD3D} for the configuration of an elliptic tokamak. The initial position for the magnetic axis is set to a previously calculated converged position. The continuous blue line shows the energy for the OM. The dashed orange line the energy for the NM and the dashed-dotted green line the energy obtained via the hybrid mapping. In (**a**) the energy evolution is shown for all 2 million iterations. In (**b**) the final iteration steps are shown to demonstrate the good agreement between the hybrid mapping and the OM in comparison to the NM.

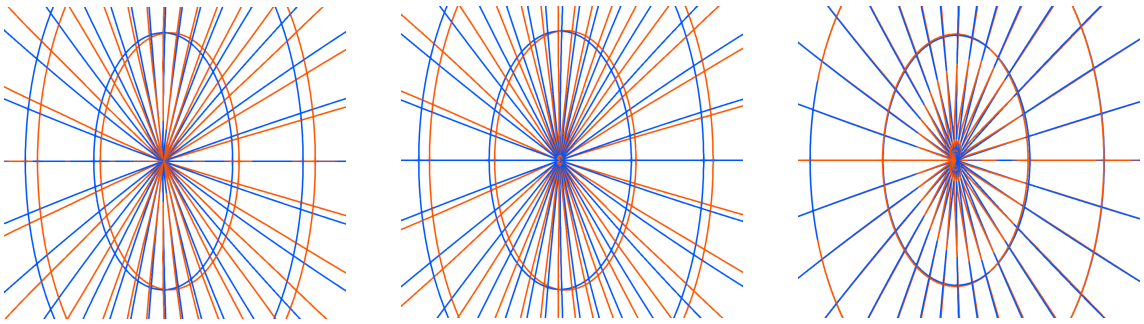

(a) initial configuration **(b)** $5 \cdot 10^4$ iterations **(c)** $2 \cdot 10^6$ iterations

Figure 22: A $\zeta = const.$ plane for the elliptic tokamak. The circular lines represent $s = const.$ contours the others represent $\theta = const.$ contours. The orange grid shows the configuration as calculated with the *HM*. The blue grid shows the *OM* solution. A total of 2 million iterations were performed for both variants of the mapping. The magnetic axis was initialised at a previously calculated converged position. The dependence of $\hat{X}_a^i$ on s resolves the previous problems with the non-local force contributions. After a suitable number of iterations, the results for the *HM* and the *OM* are in good agreement.

An additional advantage of the *HM* is, as previously discussed, the straight forward adaptation of the preconditioning scheme already used in the *OM*. To demonstrate the acceleration of the convergence towards the equilibrium configuration due to preconditioning, a comparison between a calculation with and without the preconditioner was performed for the elliptic tokamak. The results are shown in Fig.23. Clearly a drastic improvement of the energy convergence can be observed. Note, that the iteration-axis in Fig.23 uses a logarithmic scale.

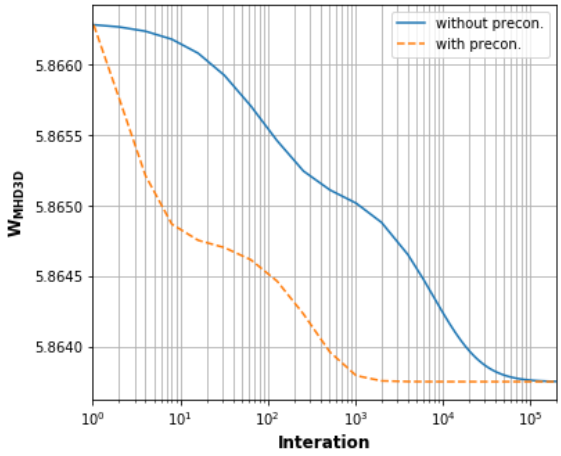

Figure 23: Comparison of the energy evolution for the elliptic tokamak test case between the minimisation using the *HM* with and without the preconditioner. Drastic improvement in terms of energy-convergence can be observed.

4.3. Influence of Boundary Conditions

An essential aspect of the hybrid mapping is, that boundary conditions (BC) with respect to the outermost (prescribed) flux surface and the magnetic axis need to be specified. This section focuses on the analysis of the influence of these BC onto the minimisation process for the *HM* and the corresponding results.

4.3.1. Improving Near Axis Asymptotic Behaviour

One important aspect is the asymptotic behaviour of the potential λ in the near axis region. The requirement that has to be fulfilled for λ at all times is the per definition arising periodicity. However, as discussed by Hirshman and Whitson [10], the near axis asymptotic of λ can be approximated for the *OM* in such a way that the derivatives of its Fourier amplitudes with respect to the angle θ vanish at the magnetic axis.[41]

Calculations with the *HM* quickly showed, that this zero derivative of λ in θ did not allow for the proper representation of the flux surfaces near the magnetic axis for the TOKSY and TOKX case. The initialisation with the *HM* carries the form of the outermost flux surface all the way towards the axis due to the blending. When the same BC as in the *OM* for λ are used, this means that the parameter α has to perform a decoupling between the modes from the boundary and the modes in the near axis region. However, α itself vanishes at the axis, thus, no decoupling occurs within reasonable iteration numbers.

In the book by F. Bauer et al. [1] where a version of the *NM* is used, no further restriction of the potential term is given apart from the periodicity[42] which is simply realized by excluding the $m = 0$ mode of the Fourier expansion.

Therefore, several approaches for the BC on λ were tested in the TOKSY case to explore their influence onto the near axis asymptotic. The first choice was naturally the BC used within the *OM*, which are Dirichlet-BC. These set λ to zero at the magnetic axis. Additionally, Neumann-BC, which require the derivative of λ with respect to s to vanish near the axis, were applied. Finally, the choice of open BC, following F. Bauer et al. [1], was used. To visualize the behaviour of λ towards the axis, the 2D-flux coordinate space (s,θ) was used. The corresponding plots can be seen in Fig.24.

It becomes quite obvious, that the original Dirichlet BC influence just a small area close to the axis forcing λ to vanish. Since the asymptotic behaviour enforced through this is a direct result of the mapping choice, it can clearly be said that this approach is wrong. Especially because the flux surface shape close to the axis in this case is stuck in the initialised state (see Fig.24b).

For the Neumann BC, non-zero values at the axis arise for λ, this already results in the desired decoupling of modes such that the flux surfaces become ellipse-shaped (see Fig.24d). Still, the requirement for a zero derivative in s of λ can not be mathematically supported.

Applying open BC seems to be the best choice in the case of the *HM*. The desired decoupling and correct representation of the flux surfaces near the axis can

[41] see Hirshman and Whitson Phys.Fluids 1983, 3558 [10]
[42] see Bauer et al. A Computational Method in Plasma Physics 1978, 9 [1]

be achieved (see Fig.24f), and no significant numerical errors due to the restriction-less minimisation seem to occur. A comparison of the innermost flux surfaces for the more complex TOKX case shows, that the same problematic occurs as in the TOKSY case, but also, that the unrestricted evolution of λ improves the near axis representation (see Fig.25). Nevertheless, achieving the decoupling from the complex boundary shape seems to be more difficult in this case.

An explanation for the difference between the behaviour of λ in the *OM* and the *HM* can be also given when considering the straight field line angle θ^*. Since this quantity is composed of the angle θ plus the potential λ, the same equilibrium solution can be obtained for a given geometry even if θ and λ are not the same for, e.g., two different mappings. Only the sum of those two variables is of importance and should yield the same result in the final equilibrium solution. Exactly this is the case for the *OM* and the *HM* as can be seen in Fig.26. The θ contours are quite different but the θ^* contours are the same.

As a conclusion, one can see that the contribution of the potential term λ near the axis is essential for the *HM* to achieve the correct ellipse-like shape expected for the innermost flux surfaces. The decoupling from modes of the edge can not be achieved by α alone.

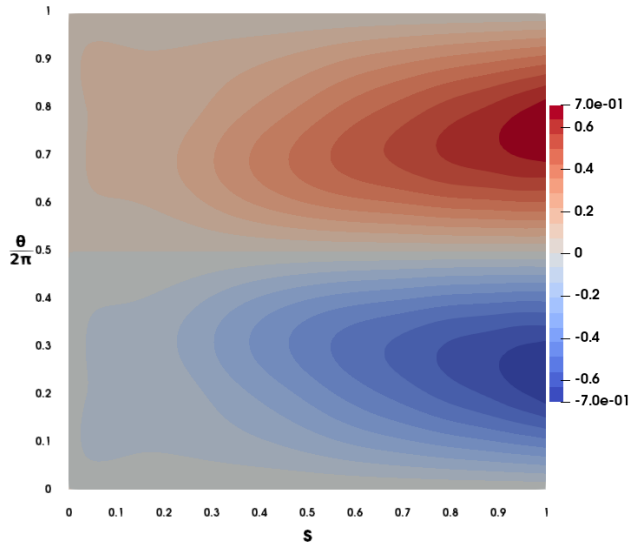

(a) Dirichlet BC: λ

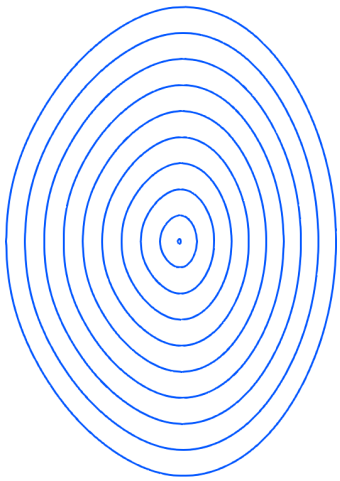

(b) Dirichlet BC: flux surfaces

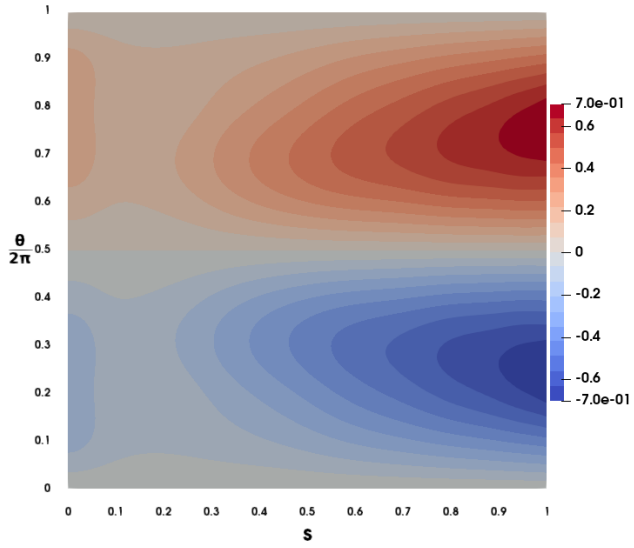

(c) Neumann BC: λ

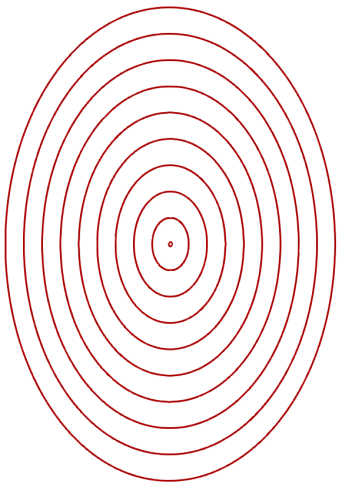

(d) Neumann BC: flux surfaces

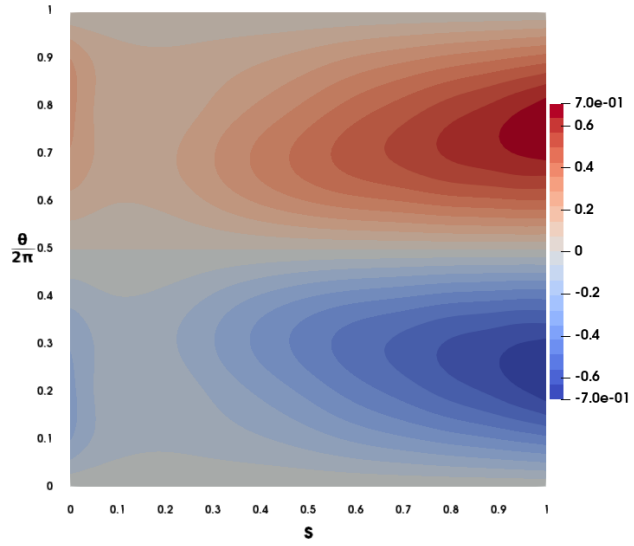

(e) open BC: λ

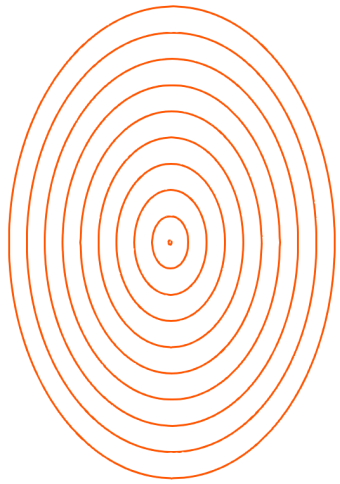

(f) open BC: flux surfaces

Figure 24: Value of the potential λ on a $\zeta = const.$ surface and flux surfaces for $s \in [0, 10^{-2}]$ for the TOKSY test case using different BC for λ at the magnetic axis (s=0).

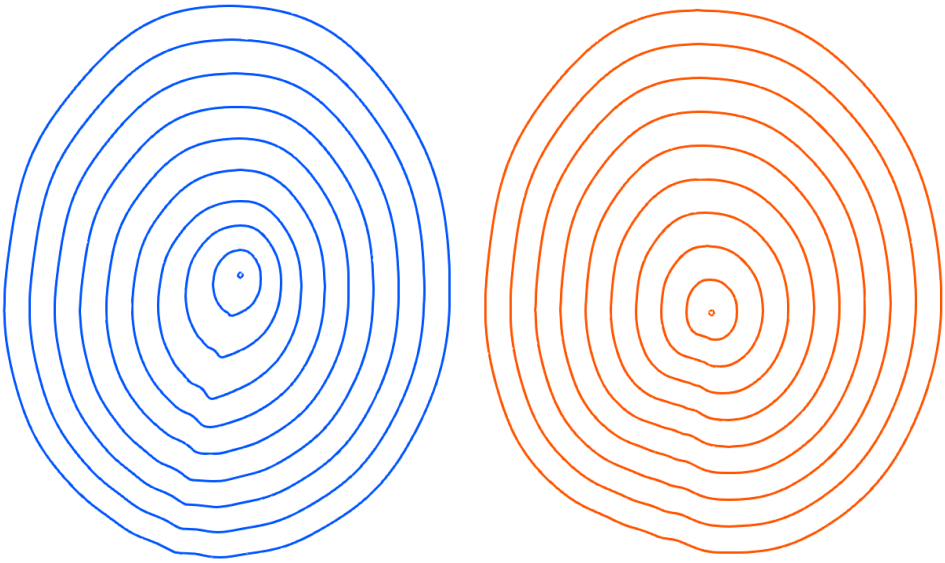

(a) Dirichlet BC **(b)** open BC

Figure 25: Flux surfaces for the TOKX test case for $s \in [0, 10^{-2}]$ using different BC for λ. The decoupling from the edge can be improved but not fully achieved by the open BC in (b).

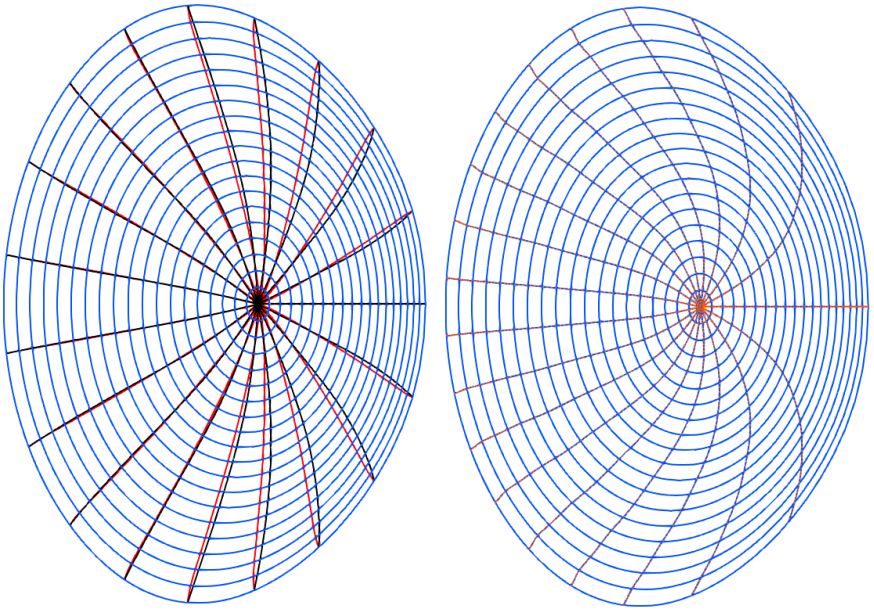

(a) θ – *contours* **(b)** θ^* – *contours*

Figure 26: Comparison between the $\theta = const.$ (black and red) and $\theta^* = \theta + \lambda = const.$ (blue and orange) contours for the TOKSY test case. The black and blue lines belong the the solution of the *OM* and the red and orange ones to the solution of the *HM*.

4.3.2. $\hat{X}_a^i$ at the outermost flux surface

As discussed in Sec.4.2, the introduction of the hybrid mapping with variable $\hat{X}_a^i(s)$ was done to allow for the correct asymptotic behaviour (4.2.1). Although the near axis asymptotic is, thus, achievable, the question how $\hat{X}_a^i(s)$ has to behave at the

outer most flux surface remains. While for the NSTAB mapping X_a^i is just a constant value for a $\zeta = const.$ surface and thus defined over the whole regime, $\hat{X}_a^i$ shows some degree of contingency at the outermost flux surface. This is due to the blending function (3.5.16) which cancels the contribution of $\hat{X}_a^i$ at $s = 1$. $\hat{X}_a^i$ can take any value and will not influence the coordinate value $X^i(s = 1, \theta, \zeta)$. Hence, the question whether some restrictions onto this variable are necessary at the outermost flux surface, since arbitrariness can prove rather problematic for minimisation algorithms.

One approach is to force the $\hat{X}_a^i$ variable to take the value of the $m = 0$ mode in θ of the boundary X_b^i, i.e. prescribe Dirichlet BC. Since $\hat{X}_a^i$ was used without the dependence on θ, such BC could enforce some consistency. The $m = 0$ mode in θ of X_b^i is the only contribution on a $\zeta = const.$-surface that would survive an integration over one period in θ. Under this consideration it could be a suitable restriction for $\hat{X}_a^i$.

For the elliptic tokamak and the TOKSY case, the Dirichlet BC resulted in a proper representation of the equilibrium configuration. A comparison of the equilibrium results with the *OM* and the *HM* for the TOKSY case can be seen in Fig.27. Calculations performed for the TOKX case, however, showed that Dirichlet-type BC for $\hat{X}_a^i(s = 1)$ are problematic for such an asymmetric geometry. In Fig.30 one can observe that this results in oscillations for the θ^* lines at the edge. This again causes a breakdown of the mapping near the edge. Visualizing $\hat{X}_a^i(s)$ (see Fig.28) for both the TOKSY and TOKX case confirms the result, that Dirichlet BC cause drastic behaviour near the edge and thus, are unfit.

A Neumann BC would be less restrictive. Whilst this might enforce some degree of smoothness towards the edge, no solid argumentation for such a restriction is at hand. Comparing results between a Neumann BC and open BC at the $s = 1$ for $\hat{X}_a^i$ shows, that the enforced zero-derivative in s only creates smoothness in a negligible area but drastically affects the near edge dependence (see Fig.29). In the TOKSY case no influence of the $\hat{X}_a^i(s = 1)$ BC onto the equilibrium configuration can be observed. In the complex TOKX case, however, the open BC results in different flux surface shapes and $\theta^* = const.$-contours near the edge when comparing the *OM* solution to the *HM* solution (see Fig.31). Especially the region near the X-point is affected by this discrepancy. The central region shows good agreement between the two mappings. It is evident, that with the *HM* the influence of the outer boundary is carried further inwards. However, due to its high complexity, the TOKX case may need a significant increase in radial and/or angular resolution to achieve a robust equilibrium for both the *OM* and the *HM*. Especially due to the rapid change of the flux surface shape towards the X-point. Additionally, this increase in resolution would result in much higher computation times.

In conclusion, an open BC for $\hat{X}_a^i$ at $s = 1$ seems to provide the best choice.

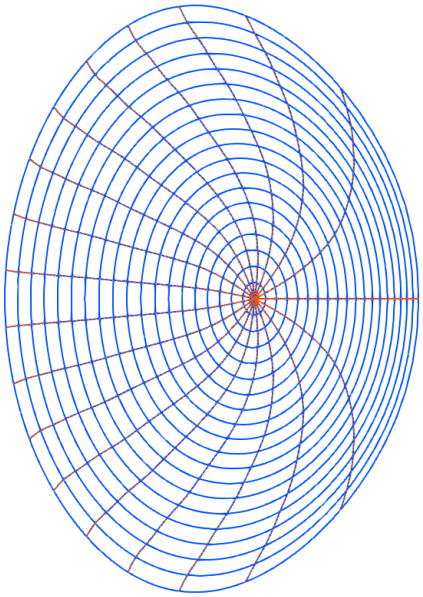

Figure 27: Comparison between the equilibrium configuration obtained with the *HM* (orange) and the *OM* (blue) for the TOKSY test case. A total of 10^6 iterations were performed. Both mappings present the same equilibrium configuration. The only discrepancy is close to the magnetic axis, but within the fluctuation range of its position. No influence of the Dirichlet BC for $\hat{X}_a^i$ is observable for the $\theta^* = const.$-lines

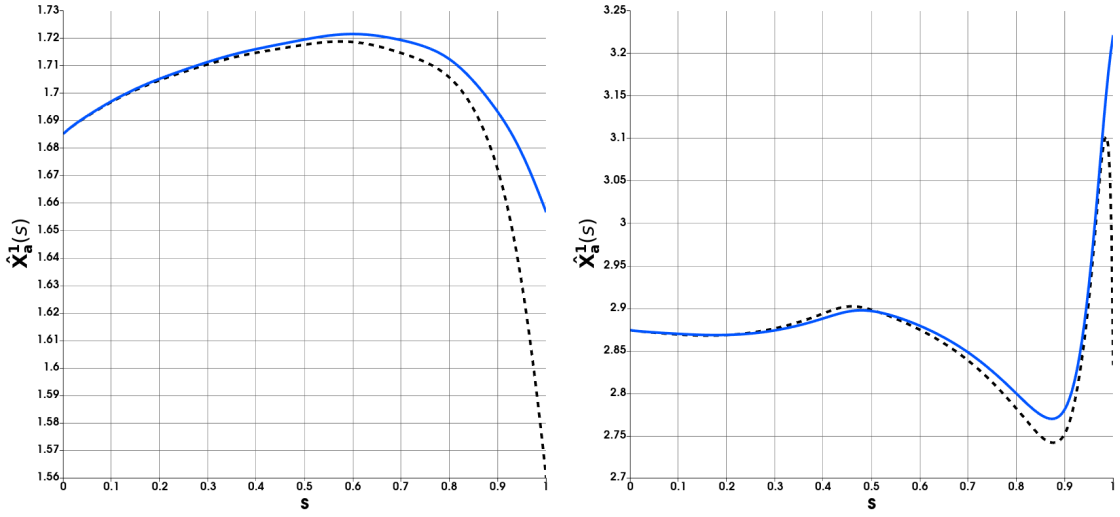

(a) TOKSY **(b)** TOKX

Figure 28: Influence of the BC at $s = 1$ on the radial dependency of $\hat{X}_a^1(s)$, open BC (solid blue line) and Dirichlet BC (dashed black line).

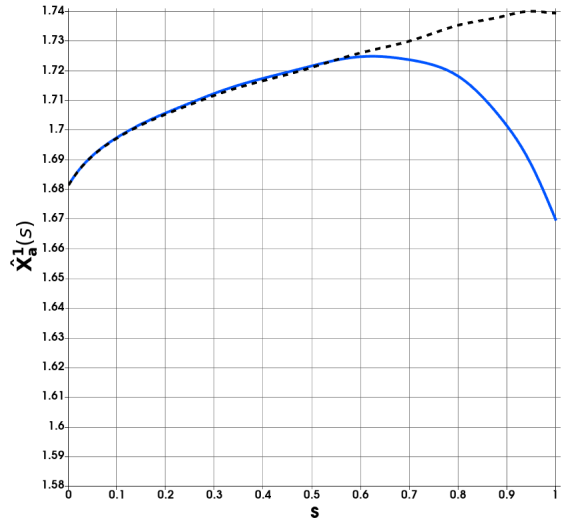

Figure 29: Influence of the BC at $s = 1$ on the radial dependency of $\hat{X}_a^1(s)$ for the TOKSY test case, open BC (solid blue line) and Neumann BC (dashed black line).

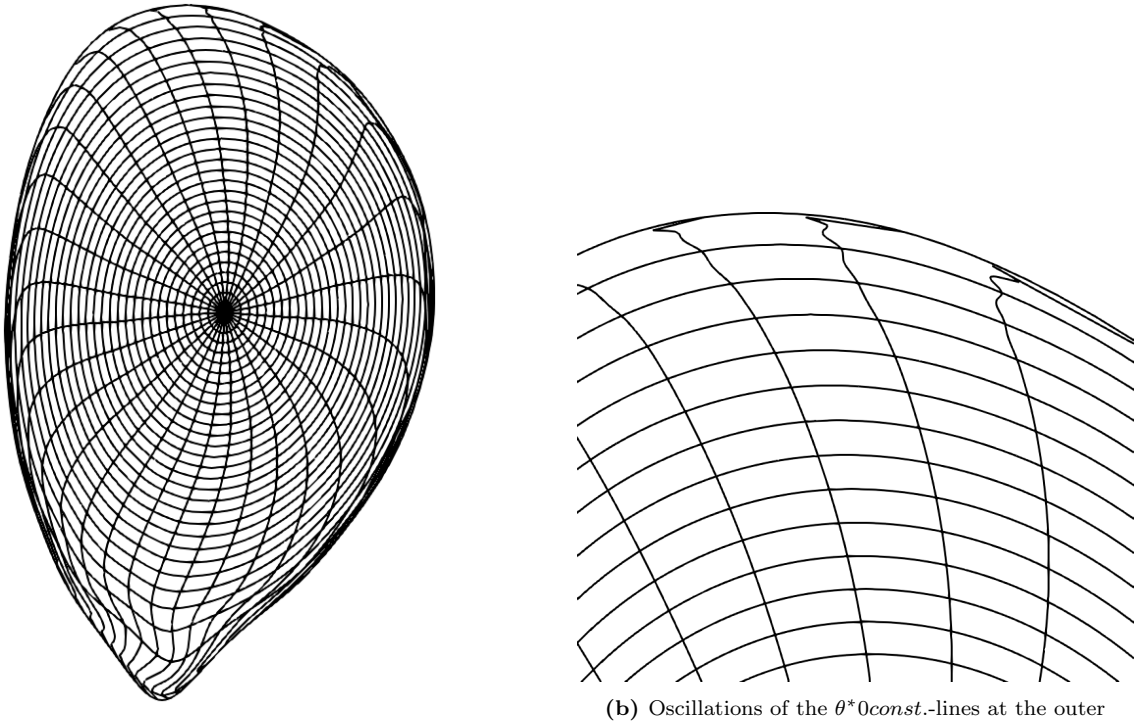

(a) $\zeta = cons.$-plane for the TOKX test

(b) Oscillations of the $\theta^* 0 const.$-lines at the outer boundary.

Figure 30: Configuration of the TOKX case using a Dirichlet BC for $\hat{X}_a^i$. The influence of the BC is visible at the edge, where the $\theta^* = const.$-lines start to oscillate.

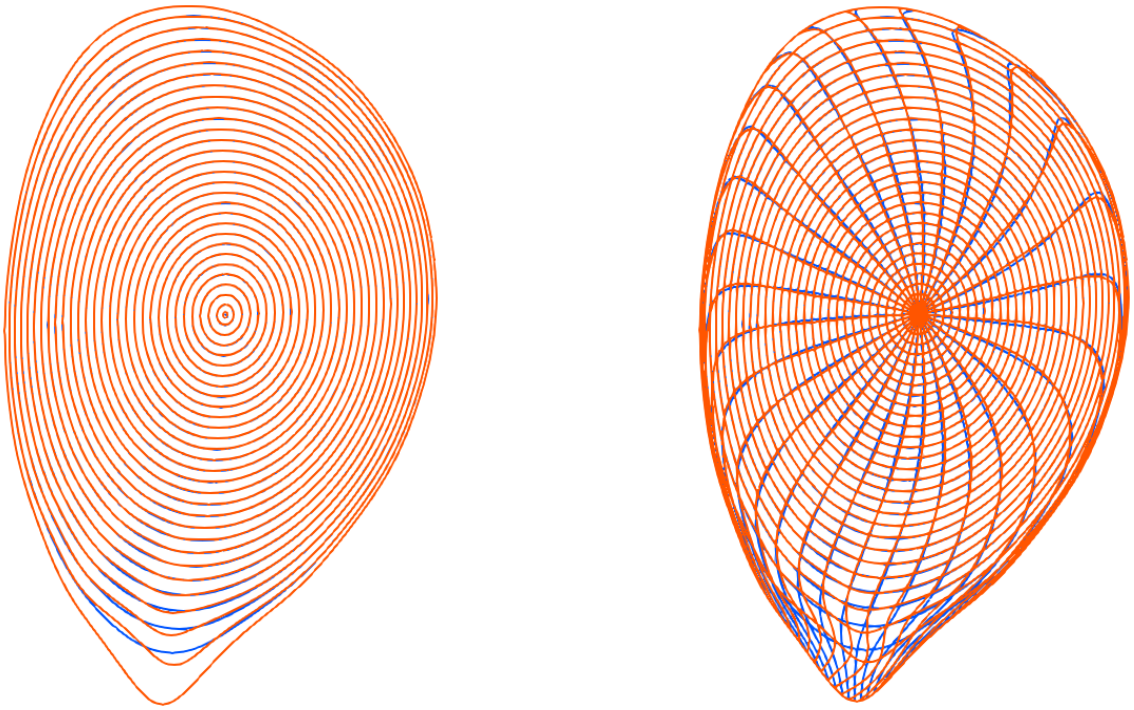

(a) constant flux contours for a $\zeta = cons.$-plane

(b) constant flux- and θ^*-contours for a $\zeta = cons.$-plane

Figure 31: Comparison between the equilibrium configuration obtained with the *OM* (blue) and the *HM* (orange) with open BC for $\hat{X}_a^i$. Differences are mainly present in the region near the X-point and in the $\theta^* = const.$ contours.

4.4. Radial and Spectral Resolution

A crucial aspect when using GVEC for equilibrium calculations is the appropriate choice of radial and spectral resolution. The first is chosen via the radial grid-size whereas the latter can be improved by using more modes in the angular directions. Therefore, the equilibrium energy and the equilibrium axis position of the *OM* and the *HM* were calculated for different radial grid-sizes and numbers of poloidal modes. The test case used is the elliptic tokamak. The minimisation parameters were the same for the two mappings to achieve a good comparability. For the solution variables this means that, e.g., the same number of modes was chosen. As an example, if eight poloidal modes are used this means that for the *OM* X^1, X^2 and λ are constructed with these. For the hybrid mapping, however, α and λ would be described via eight modes, not necessarily X^1 and X^2.

In Fig.32 the energies obtained with different resolutions are plotted. Each point represents the energy value after $2 \cdot 10^5$ iterations. These iterations were performed after restarting from the solution using a coarse equidistant radial grid of five elements. This initial calculation itself was performed for $4 \cdot 10^5$ iterations to ensure a suitable equilibrium with the chosen parameters.

One of the obvious results is that the number of necessary poloidal modes is quite high given the simplicity of the test case, since the outermost flux surface is de-

scribed by only the $m = 0$ and $m = 1$ poloidal mode. However, no essential gain in accuracy is given after a certain threshold, which can be seen when comparing the calculations using eight and twelve poloidal modes. The *HM* appears to be more sensitive to the mode number beneath $m = 8$.

For increasing radial grid size it can be observed, that the calculated energies converge onto a common value. The number of radial grid-elements used here were 5, 12, 21, 42 and 60 with an equidistant grid in s.

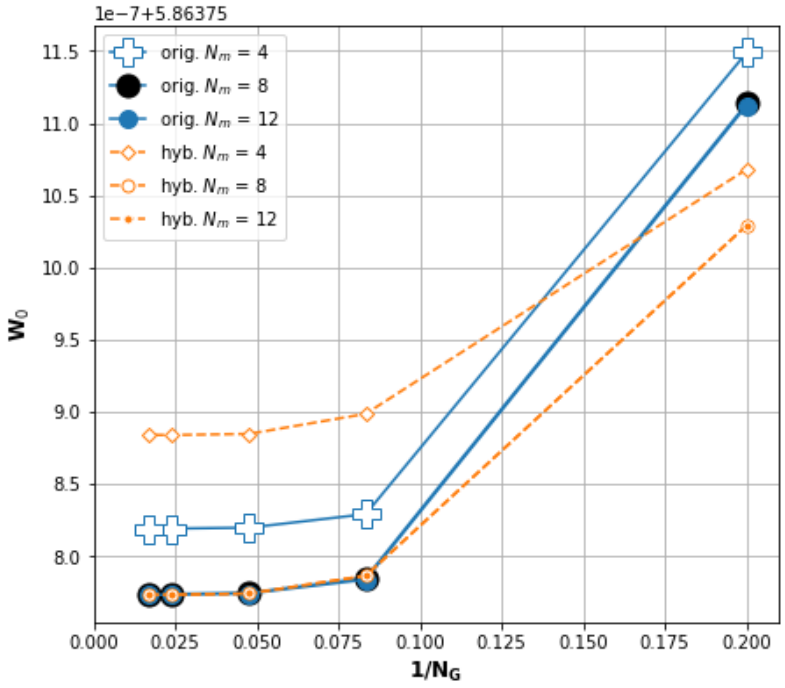

Figure 32: Minimum total energy of the elliptic tokamak test case for the *OM* and the *HM* using different radial grid-sizes N_G and a different number of poloidal modes N_m.

Fig.33 shows the influence of the resolution onto the position of the magnetic axis. Due to the symmetry of the test case, only $X_a^1(s = 0)$ is plotted, $X_a^2(s = 0)$ is always zero.

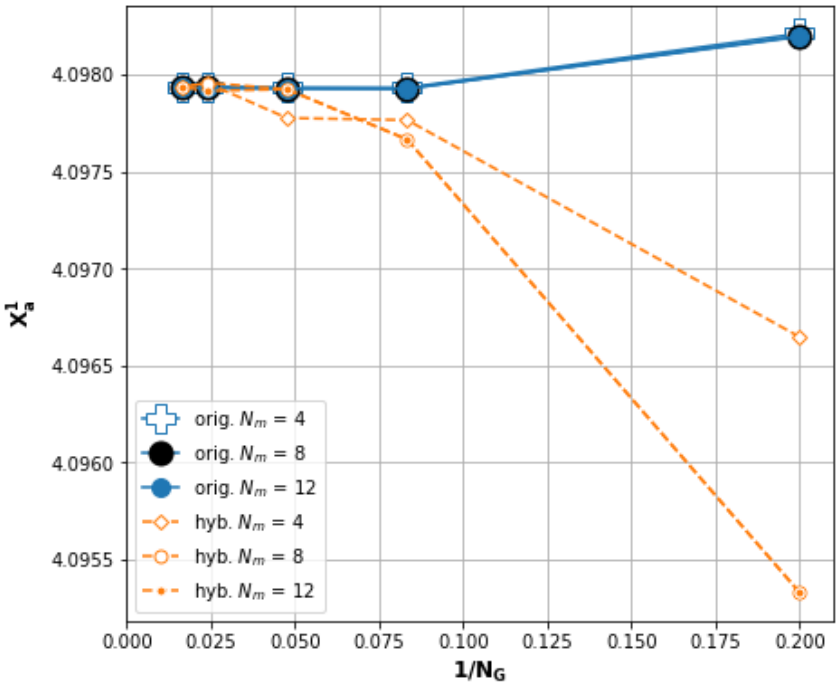

Figure 33: Position of the magnetic axis $X_a^1(s = 0)$ of the elliptic tokamak test case for the *OM* and the *HM* using different radial grid-sizes N_G and a different number of poloidal modes N_m. The coordinate X_a^2 is always numerical zero in this case.

For the *OM* one can observe that the position of the magnetic axis converges quickly onto the same position with increasing radial grid size and is almost independent of the number of poloidal modes. For the *HM* the mode number again exposes a more drastic influence beneath $m = 8$. Furthermore, it can be seen, that the position of the magnetic axis converges at a larger number of radial grid elements for the *HM*. Only above 21 grid elements the change in the axis position becomes comparatively small. Whereas, for the *OM* this can already be said for about 12 radial grid elements. Nevertheless, this test case suggests, that for an adequate representation of the magnetic axis a surprisingly high spectral and radial resolution is required for the *HM*. In the appendix A. one can find a visualization of the evolution of the axis position with increasing iteration number for the different resolutions used in Fig.33.

5. Summary and Conclusion

Starting from the fundamental derivations for the framework of ideal MHD, the theoretical setup for the 3D-MHD equilibrium code GVEC was introduced and explained. In Sec.2.1 a detailed derivation of the ideal MHD equations is given and their validity regime is discussed. The necessary assumptions for ideal MHD can be summarized with the constraints of *high collisionality*, *small ion gyro-radius* and *small resistivity* for the described plasmas. Together with the low frequency Maxwell equations, the ideal MHD equations form a closed system. MHD equilibria are calculated by solving the force-balance equation $\nabla P = \mathbf{J} \times \mathbf{B}$, where P is the pressure, $\mathbf{J}$ the current density and $\mathbf{B}$ the magnetic field.

In Sec.2.2 the important concept of flux coordinates was discussed. In the core of a magnetically confined plasma, assuming nested closed flux surfaces, they drastically simplify the treatment of the corresponding equations by depicting the magnetic field $\mathbf{B}$ and/or the current density $\mathbf{J}$ as straight lines. Flux coordinates usually consist of a radial like flux label and two angular coordinates. For GVEC these are (s, θ^*, ζ), where s is a flux label proportional to the square root of the toroidal flux, θ^* is the straight field line angle and ζ the toroidal angle. GVEC itself calculates equilibrium configurations by minimizing the total ideal MHD-energy using a gradient descent method. An additional important assumption implied in the code is the existence of nested flux surfaces.

In this work, an alternative mapping of the magnetic field topology, based on the NSTAB computer code [2], was implemented and tested for GVEC. This was done in close cooperation with the Max-Planck Institute for Plasma Physics through Dr. Ing. Florian Hindenlang. The geometry of the magnetic flux surfaces is expressed by a mapping of the flux coordinates onto real space coordinates (X^1, X^2, ζ). The idea behind the NSTAB mapping is to express X^i via a blending function of the outermost flux surface X^i_b and the magnetic axis X^i_a using a generalized radius α, which couples the X^1 and X^2 coordinates. For the new variables the discretization features of GVEC are kept, which use B-Splines in radial direction and Fourier-modes in the periodic angular directions.

As demonstrated in the numerical results, this NSTAB mapping fails to solve a simple elliptic tokamak case in the region of the magnetic axis. Therefore, an additional mapping, hybridising the original and the NSTAB mapping, was introduced, by adding a radial dependency to X^i_a (denoted by the variable $\hat{X}^i_a(s)$), which solved the problem of the axis region. The Hybrid mapping allowed to adapt the existing preconditioning scheme leading to faster convergence.

The influence of different boundary conditions onto the final equilibrium solution was analysed for the hybrid mapping using several test cases of increasing complexity. Open boundary conditions for λ and the new variable $\hat{X}^i_a$ proved best, especially for complex boundary shapes, where other choices may lead to a breakdown of the mapping. In the original mapping of GVEC, the variable λ vanishes at the mag-

netic axis, whereas for the hybrid mapping, the open BC was found to be important. Since λ plays the role of a reparametrization of the angle θ, a non-vanishing BC allowed to decouple the shape of the inner flux surfaces from the boundary shape, and therefore allowing the expected elliptic shape in the near axis region. Nevertheless, in the case of the complex boundary shape, a high number of iterations was still required.

Finally, the influence of the radial and spectral resolution using the original and the hybrid mapping were investigated. For both, the total energy converges onto a very similar value with increasing spectral mode number and radial grid size. The hybrid mapping is more sensible regarding the spectral resolution. The magnetic axis too is placed similarly, although, the original mapping shows less sensitivity with regards to the tested parameters.

No immediate improvement through the alternative mappings with regards to the original one can be observed for the three tested cases. The NSTAB version heavily relies on the special treatment of the near axis region and therefore is unfit for GVEC. The hybrid mapping performs well for the simple and intermediate boundary test cases and is comparable to the original mapping. For the test case with a complex boundary shape, however, discrepancies between the original and the hybrid mapping occur. The underlying edge-centre blending of the hybrid mapping becomes quite evident in this case and requires a careful choice of the boundary conditions. A distinguishing feature allowing to classify the quality of the equilibrium solution would be the local force balance, which is left for future work.

The question whether perturbations could be calculated more easily with the alternative description, which motivated this thesis, remains. However, it is questionable if calculations with perturbed systems are even meaningful, unless a clear statement for the higher or equivalent quality of the unperturbed equilibrium solution of the hybrid mapping in comparison to the original one can be made.

6. References

[1] F.Bauer, O.Betancourt, P.Garabedian,
A Computational Method in Plasma Physics,
Springer-Verlag (1978)

[2] M.Taylor,
A High Performance Spectral Code for Nonlinear MHD Stability,
Journal of Computational Physics 110 (1994)

[3] E.Weisstein
"B-Spline." MathWorld–A Wolfram Web Resource. `https://mathworld.wolfram.com/B-Spline.html` Last access: 12.10.2020

[4] W.D.D'haeseleer, W.N.G.Hitchon, J.D.Callen, J.L.Shohet,
Flux Coordinates and Magnetic Field Structure,
Springer-Verlag (1991)

[5] P.M.Bellan,
Fundamentals of Plasma Physics,
Cambridge University Press (2008)

[6] F.Hindenlang, O.Maj,
GVEC prototype, (internal code documentation)
Max-Planck-Institute for Plasma Physics (2020)

[7] J.P.Freidberg,
Ideal MHD,
Cambridge University Press (2014)

[8] S.P.Hirshman, O.Betancourt,
Preconditioned Descent Algorithm for Rapid Calculations of Magnetohydrodynamic Equilibria
Journal of Computational Physics 96 (1991)

[9] S.E.Kruger, J.M.Greene,
The relationship between flux coordinates and equilibrium-based frames of reference in fusion theory
Phys. Plasmas 26, 082506 (2019)

[10] S.P.Hirshman, J.C.Whitson,
Steepest-descent moment method for three-dimensional magnetohydrodynamic equilibria,
The Physics of Fluids 26, 3553 (1983)

A. Convergence of the Magnetic Axis Position

In this appendix one can find a visualization of the position of the magnetic axis over the iteration number for the three different test cases introduced in Sec.4. For the hybrid mapping the suited boundary conditions discussed in Sec.4.3 were used. The results presented in Fig.36 - 41 correspond to the individual points shown in Fig.33.

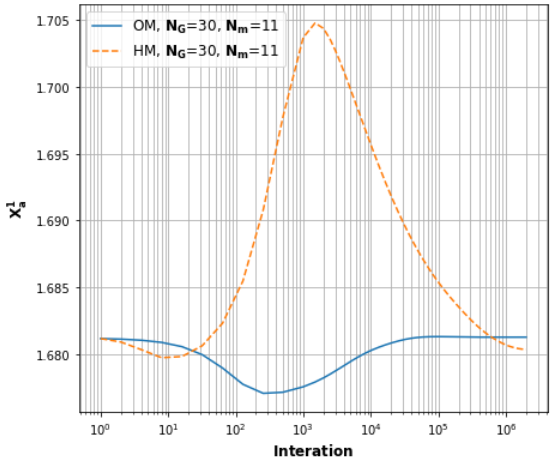

Figure 34: Position of the magnetic axis X_a^1 over the iteration number for the TOKSY tokamak test case using the original mapping (blue-solid) and the hybrid mapping (orange-dashed) for $N_G = 30$ radial grid elements and $N_m = 11$ poloidal Fourier modes.

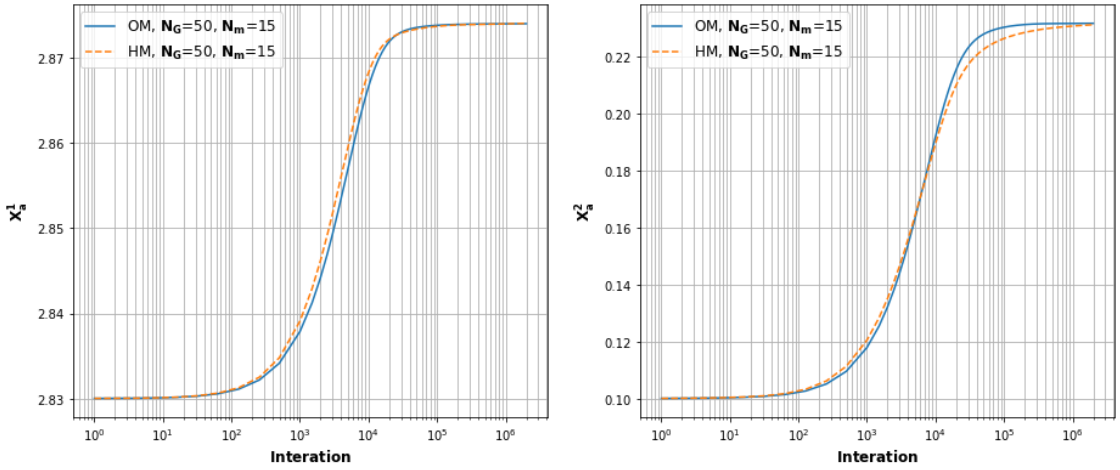

(a) **(b)**

Figure 35: Position of the magnetic axis X_a^1 and X_a^2 over the iteration number for the TOKX tokamak test case using the original mapping (blue-solid) and the hybrid mapping (orange-dashed) for $N_G = 50$ radial grid elements and $N_m = 15$ poloidal Fourier modes.

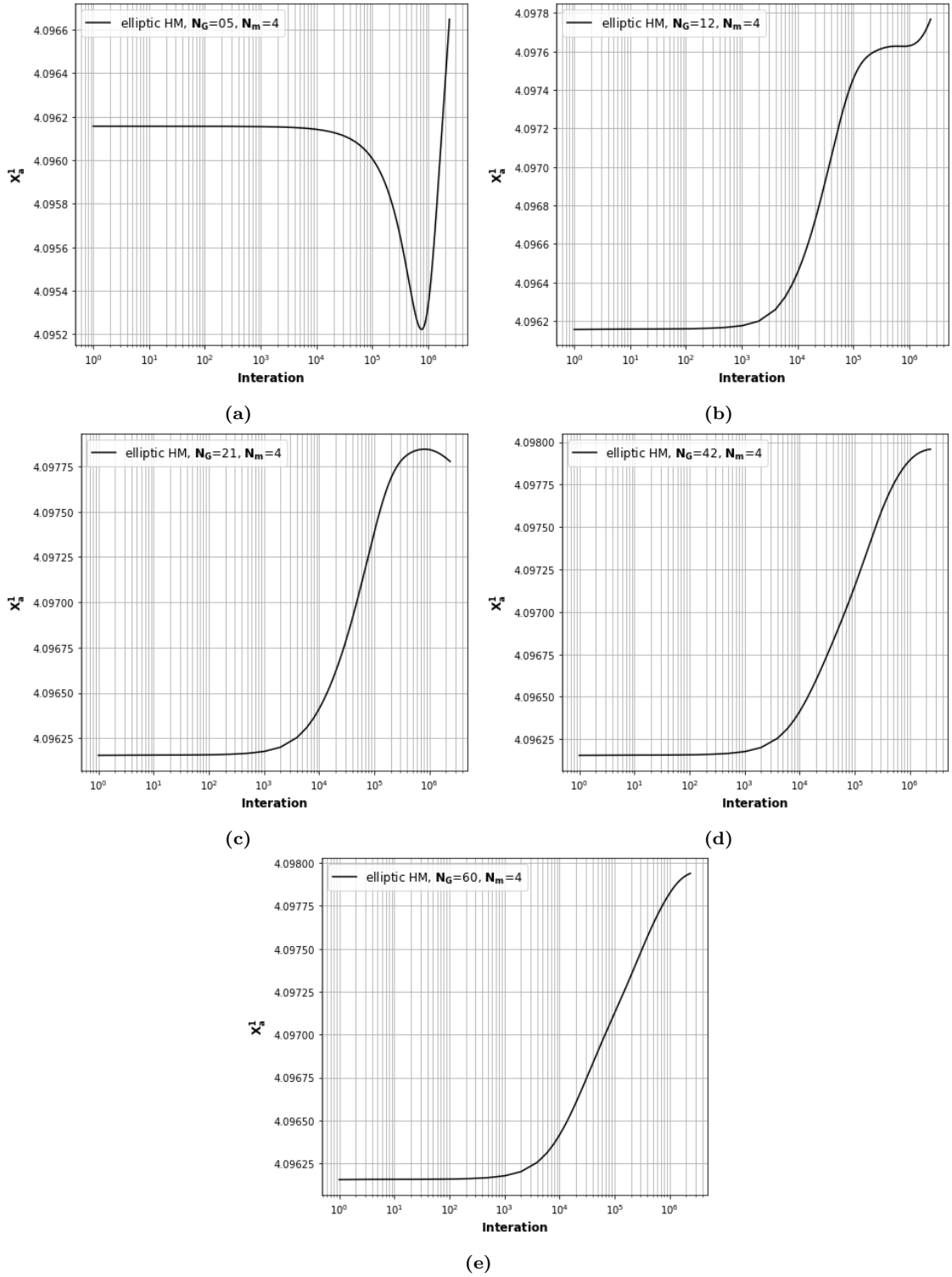

Figure 36: Position of the magnetic axis X_a^1 over the iteration number for the elliptic tokamak test case using the hybrid mapping with different radial resolutions and $N_m = 4$ poloidal Fourier modes. N_G is the number of radial grid elements.

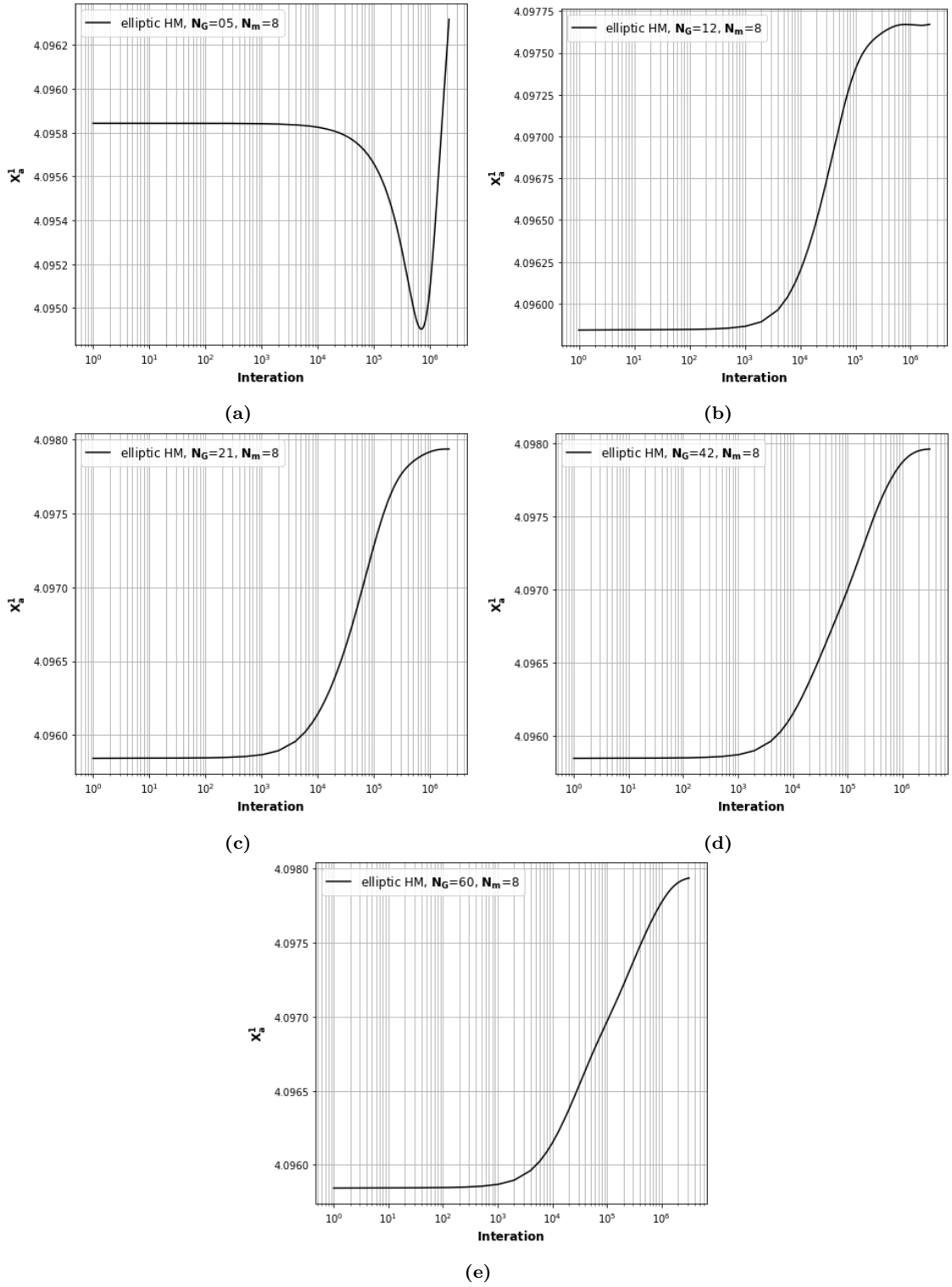

Figure 37: Position of the magnetic axis X_a^1 over the iteration number for the elliptic tokamak test case using the hybrid mapping with different radial resolutions and $N_m = 8$ poloidal Fourier modes. N_G is the number of radial grid elements.

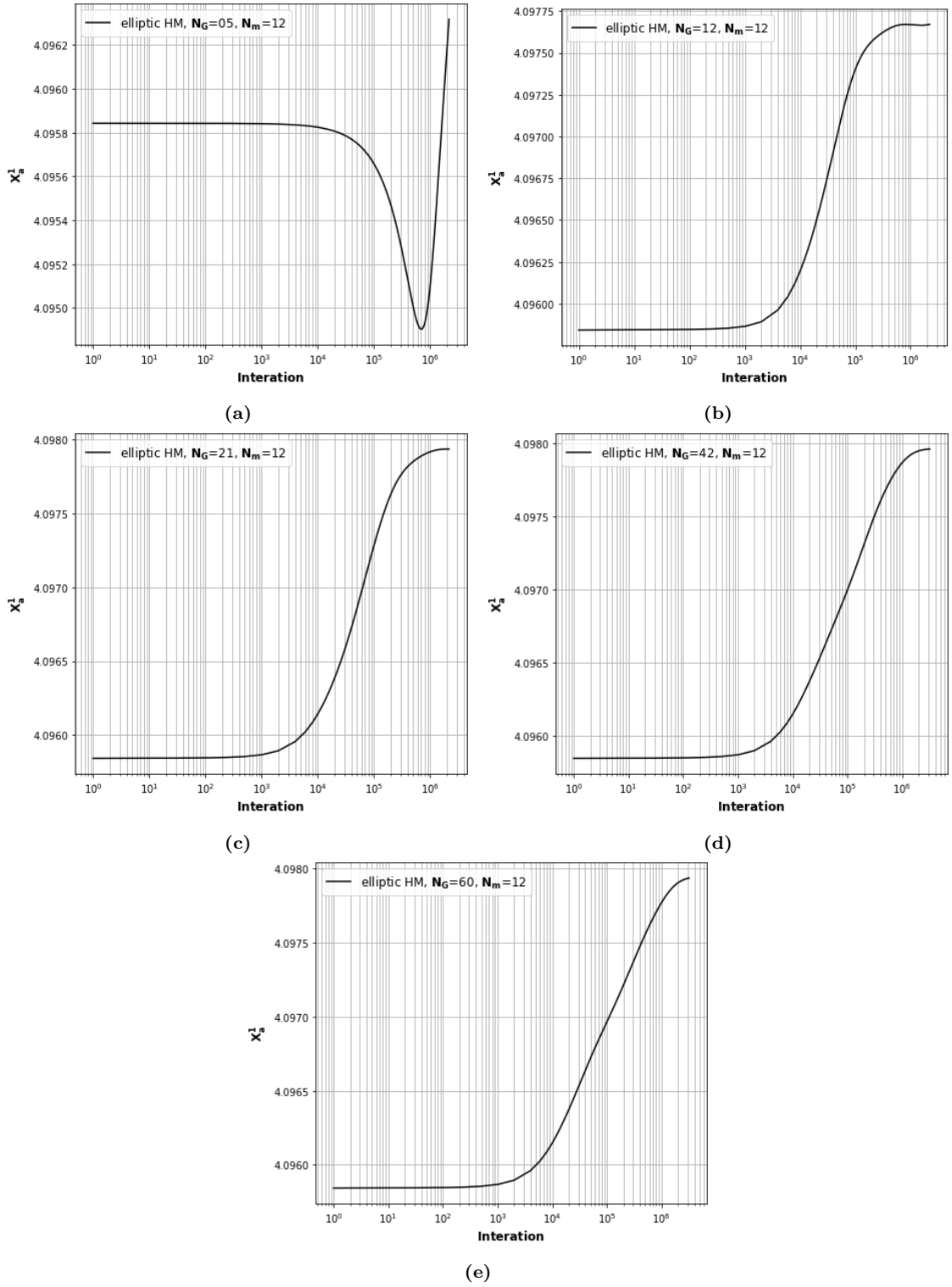

Figure 38: Position of the magnetic axis X_a^1 over the iteration number for the elliptic tokamak test case using the hybrid mapping with different radial resolutions and $N_m = 12$ poloidal Fourier modes. N_G is the number of radial grid elements.

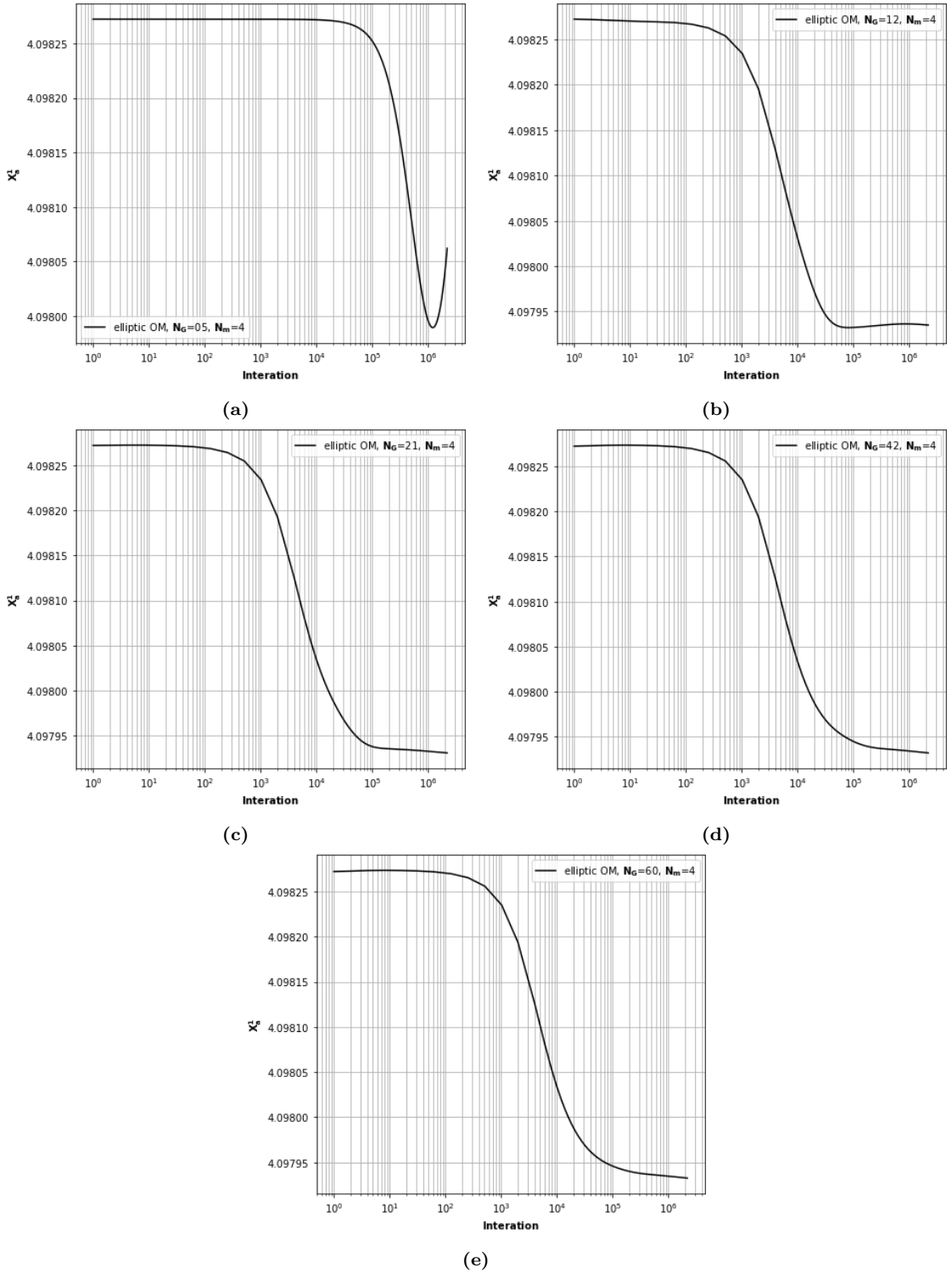

Figure 39: Position of the magnetic axis X_a^1 over the iteration number for the elliptic tokamak test case using the original mapping with different radial resolutions and $N_m = 4$ poloidal Fourier modes. N_G is the number of radial grid elements.

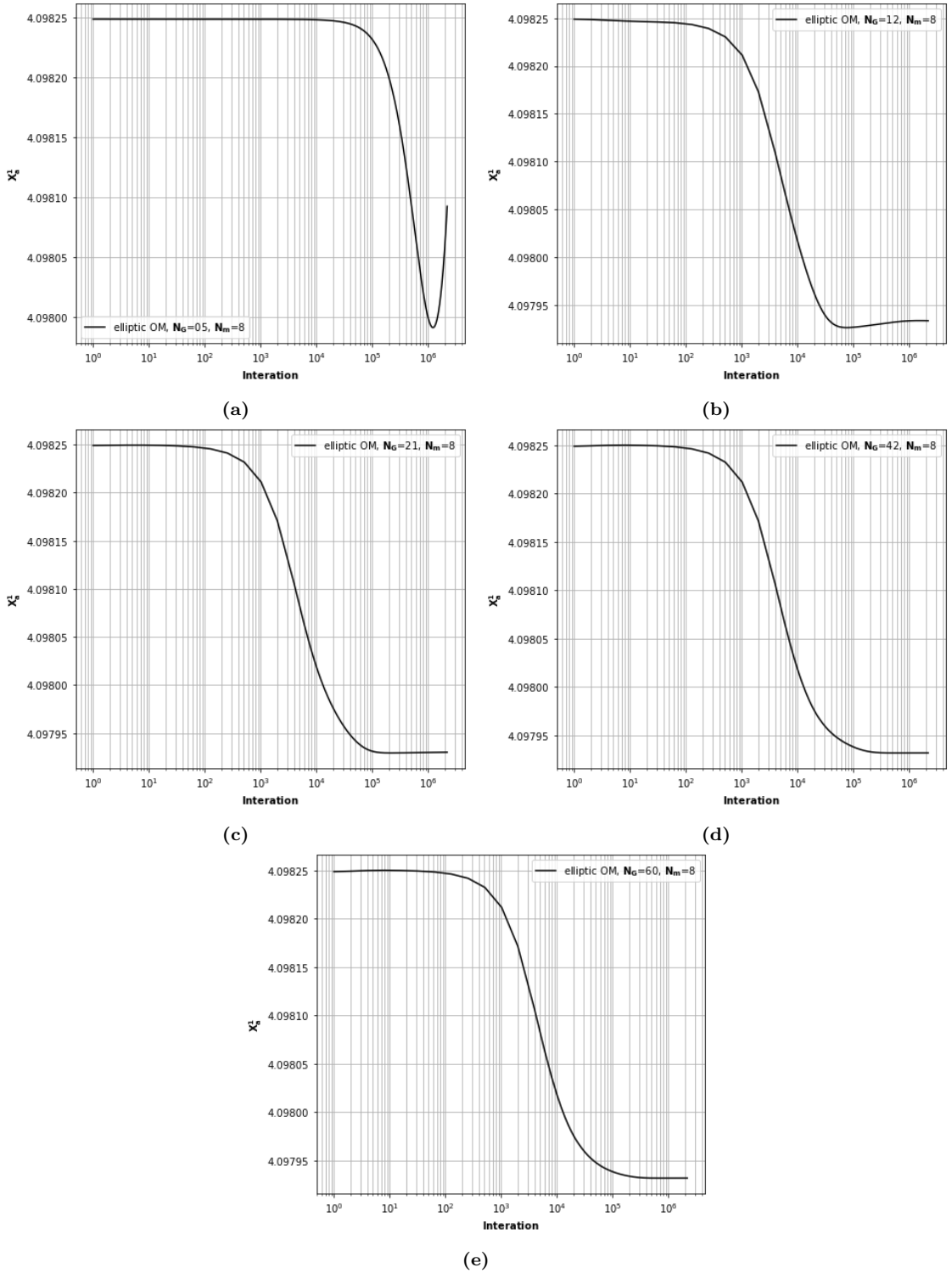

Figure 40: Position of the magnetic axis X_a^1 over the iteration number for the elliptic tokamak test case using the original mapping with different radial resolutions and $N_m = 8$ poloidal Fourier modes. N_G is the number of radial grid elements.

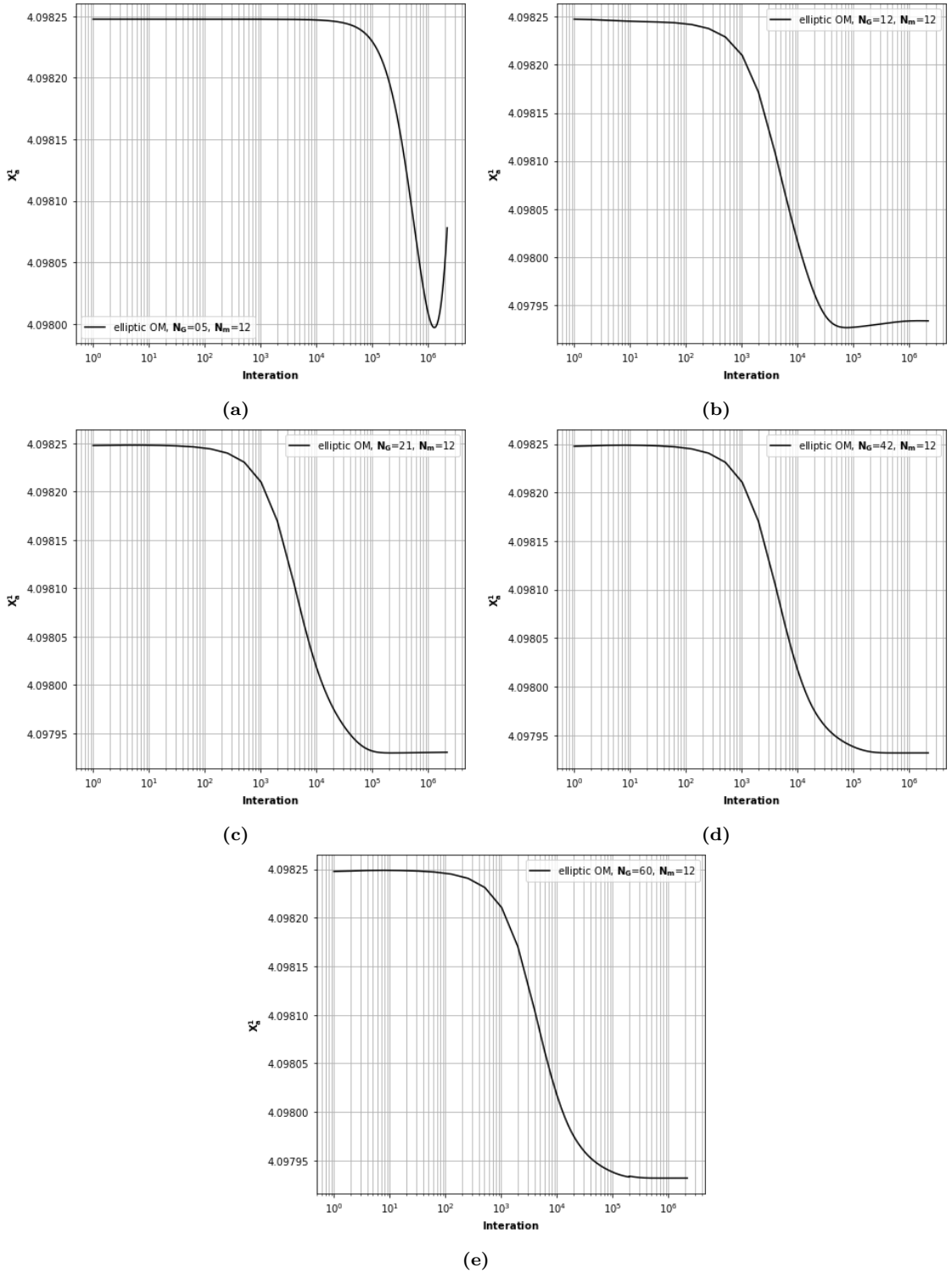

Figure 41: Position of the magnetic axis X_a^1 over the iteration number for the elliptic tokamak test case using the original mapping with different radial resolutions and $N_m = 12$ poloidal Fourier modes. N_G is the number of radial grid elements.